Using Clinopyroxene Chemistry to Constrain Magma Plumbing Systems in a 1.2 Ga Andesitic to Shoshonitic Volcanic Arc, Barby Formation, Namibia

by

LAUREN TAYLOR BURDEN

Bachelor of Science, 2020
Texas Christian University
Fort Worth, TX

Submitted to the Graduate Faculty of the
College of Science and Engineering
Texas Christian University
In partial fulfillment of the requirements
For the degree of

MASTER OF SCIENCE

MAY 2022

USING CLINOPYROXENE CHEMISTRY TO CONSTRAIN MAGMA PLUMBING SYSTEMS IN A 1.2 GA ANDESITIC TO SHOSHONITIC VOLCANIC ARC, BARBY FORMATION, NAMIBIA

By

Lauren Taylor Burden

Thesis approved:

Major Professor

For The College of Science and Engineering

ACKNOWLEDGEMENTS

I would like to thank my advisor, Dr. Richard Hanson, for all his support through my graduate and undergraduate career at TCU. Thank you for providing me a solid foundation for my education and the helping me grow into the student I am today. I want to thank my committee members, Dr. Helge Alsleben, Dr. Arthur Busbey III, Dr. Steven Singletary, for their help and advice the last two years.

My love and gratitude to my family and friends. Thank you for keeping me grounded in the stressful moments and the endless support you have given me throughout this process. A special thanks to my fellow graduate students for taking this journey with me. Without your words of encouragement, I would not have challenged myself to pursue such an amazing opportunity.

TABLE OF CONTENTS

Acknowledgements II

Table of Contents III

List of Figures V

List of Tables VII

I. Introduction 1

Statement of Problem 1

Regional Geology 2

Konkiep Terrane 5

Recent Work on the Barby Formation 10

Whole-rock Chemistry for the Barby Formation 18

II. Methodology 24

Electron Microprobe Analysis 25

Geothermobarometry 27

III. Results 29

Petrography 29

Cpx Chemistry 38

Geothermobarometry 48

IV. Discussion And Conclusions 53

Cpx Chemistry 53

Geothermobarometry 54

Appendix I: EPMA Data 56

Appendix II: Cpx Chemistry..... 68

Appendix III: Cpx Temperatures And Pressures..... 92

References..... 107

Vita

Abstract

LIST OF FIGURES

1. Major Precambrian orogenic belts and cratons in southern Africa 4
2. Close up of southern Africa showing the study area in southern Namibia..... 4
3. Geologic map of the Konkiep terrane modified from Miller (2008)..... 6
4. Map of Andrews et al. (2016) field area to the east of the Aubures half graben 11
5. Measured sections done by Andrews et al. (2016)..... 14
6. Map modified from Ohrmundt (2020) of the Barby Formation..... 15
7. Oblique view of Ohrmundt's (2020) field area..... 16
8. Locations of mapped sill packages..... 17
9. Measured sections of sill packages 1-3 in Figure 8..... 18
10. Harker variation diagram for CaO..... 19
11. Harker variation diagram for MgO..... 19
12. Harker variation diagram for FeO 20
13. Harker variation diagram for TiO_2 20
14. Harker variation diagram for Na_2O..... 21
15. Harker variation diagram for K_2O..... 21
16. Nb/Yb vs. Zr/Ti classification diagram from Pearce (1996) 22
17. La/10-Y/15-Nb/8 discrimination diagram from Cabanis and Lecolle (1989)..... 23
18. Zr-Ti/100-Y*3 discrimination diagram from Pearce and Cann (1973)..... 23
19. Ta/Yb vs. Th/Yb discrimination diagram from Pearce (1982) 24
20. Electron microprobe at Fayetteville State University..... 27
21. Pyroclastic bomb sample SO-1747A..... 30
22. Pyroclastic bomb sample SO-18176 B. 31
23. Agglutinate sample SO-1767 C..... 31
24. Hypabyssal intrusion sample SO-1894..... 32
25. All data points for cpx analyzed in this study 38
26. Cpx compositions for sills..... 38
27. Cpx compositions for spatter and agglutinate..... 39
28. Cpx compositions for other hypabyssal intrusions..... 39
29. Cpx compositions for pyroclastic bombs..... 40
30. Cpx compositions for bedded lapillistone..... 40
31. Average Mg# vs. FeO wt% for individual crystals 41
32. Average FeO vs. MgO wt% for individual crystals 42
33. Average FeO vs. MnO wt% for individual crystals 42
34. Average Mg# vs.Cr_2O_3 wt% for individual crystals..... 43
35. Diagram showing variations between CaO, TiO_2, and Al_2O_3 contents vs. Mg# for individual crystals..... 44
36. Average Al_2O_3 vs. TiO_2 wt%..... 45
37. Ca+Na vs. Ti discrimination plot from Leterrier et al. (1982)..... 47
38. Ca vs. Ti+Cr discrimination plot from Leterrier et al. (1982)..... 47
39. Temperature and pressure results for sills..... 50
40. Temperature and pressure results for spatter and agglutinate. 51

41. Temperature and pressure results for other hypabyssal intrusions 51
42. Temperature and pressure results for pyroclastic bombs 52
43. Temperature and pressure results for bedded lapillistone 52
44. Sample KB43-16 from sill package 1 (Andrews) 69
45. Sample PO7-16 from sill package 2 (Andrews). 70
46. Sample G56-16 from sill package 3 (Andrews). 71
47. Sample M6-4 from a sill (Ohrmundt) 72
48. Sample VA 1603, agglutinate (Andrews) 73
49. Sample SO-18126 A, agglutinate (Ohrmundt). 74
50. Sample SO-1767 C from agglutinate (Ohrmundt) 75
51. Sample M1-1A from agglutinate (Ohrmundt). 76
52. Sample VA 16105 from a hypabyssal intrusion (Andrews) 77
53. Sample SO-1716 D from a hypabyssal intrusion (Ohrumundt) 78
54. Sample SO-1763 G from a hypabyssal intrusion (Ohrmundt) 79
55. Sample M3-4 from a hypabyssal intrusion (Ohrmundt) 80
56. Sample SO-1888A from a hypabyssal intrusion (Ohrmundt) 81
57. Sample SO-1894 from a hypabyssal intrusion (Ohrmundt) 82
58. Sample SO-18166 from a hypabyssal intrusion (Ohrmundt) 83
59. Sample MS6-7 from a pyroclastic bomb (Andrews) 84
60. Sample M1-4B from a pyroclastic bomb (Ohrmundt) 85
61. Sample M2-1A from a pyroclastic bomb (Ohrmundt) 86
62. Sample M3-3 from a pyroclastic bomb (Ohrmundt) 87
63. Sample SO-18173 from a pyroclastic bomb (Ohrmundt) 88
64. Sample SO-18176 B from a pyroclastic bomb (Ohrmundt) 89
65. Sample SO-1747A from a pyroclastic bomb (Ohrmundt) 90
66. Sample 1601.2A from bedded lapillistone (Andrews) 91

LIST OF TABLES

1. Sample locations 25
2. Thin section description of sill samples 33
3. Thin section description of spatter and agglutinuate samples 34
4. Thin section description of other hypabyssal intrusions 35
5. Thin section description of pyroclastic bomb samples 36
6. Thin section description of bedded lapillistone sample 37
7. Average cpx wt% of major oxides in each sample 46
8. Average temperature and pressure values for each sample 49
9. Sample KB43-16 wt% of major oxides 56
10. Sample PO7-16 wt% of major oxides 56
11. Sample G56-16 wt% of major oxides 57
12. Sample M6-4 wt% of major oxides 57
13. Sample VA1603 wt% of major oxides 58
14. Sample SO-18126A wt% of major oxides 58
15. Sample SO-1767 C wt% of major oxides 59
16. Sample M1-1A wt% of major oxides 59
17. Sample VA16105 wt% of major oxides 60
18. Sample SO-1716 D wt% of major oxides 60
19. Sample SO-1763 G wt% of major oxides 61
20. Sample M3-4 wt% of major oxides 61
21. Sample SO-1888A wt% of major oxides 62
22. Sample SO-1894 wt% of major oxides 62
23. Sample SO-18166 wt% of major oxides 63
24. Sample MS6-7 wt% of major oxides 63
25. Sample M1-4B wt% of major oxides 64
26. Sample M2-1A wt% of major oxides 64
27. Sample M3-3 wt% of major oxides 65
28. Sample SO-18173 wt% of major oxides 65
29. Sample SO-18176 B wt% of major oxides 66
30. Sample SO-1747A wt% of major oxides 66
31. Sample 1601.2A wt% of major oxides 67
32. KB43-16 temperatures and pressures 92
33. PO7-16 temperatures and pressures 93
34. G56-16 temperatures and pressures 93
35. M6-4 temperatures and pressures 94
36. VA 1603 temperatures and pressures 94
37. SO-18126 A temperatures and pressures 95
38. SO-1767 C temperatures and pressures 95
39. M1-1A temperatures and pressures 96
40. VA 16105 temperatures and pressures 97
41. SO-1716 D temperatures and pressures 98

42. SO-1763 G temperatures and pressures 99
43. M3-4 temperatures and pressures 99
44. SO-1888A temperatures and pressures 100
45. SO-1894 temperatures and pressures 100
46. SO-18166 temperatures and pressures 101
47. MS6-7 temperatures and pressures 101
48. M1-4B temperatures and pressures 102
49. M2-1A temperatures and pressures 102
50. M3-3 temperatures and pressures 103
51. SO-18173 temperatures and pressures 104
52. SO-18176 B temperatures and pressures 105
53. SO-1747A temperatures and pressures 105
54. 1601.2A temperatures and pressures 106

I. INTRODUCTION

Statement of Problem

The Barby Formation is a major rock unit within the Mesoproterozoic Konkiep terrane in southwest Namibia, which makes up part of the Namaqua-Natal orogenic belt (NNOB) in southern Africa (Figures 1 and 2). The formation consists mainly of calc-alkaline to shoshonitic basaltic andesites to andesites formed in a 1.2 Ga volcanic arc (Hoal, 1990; Miller, 2008). Here I use clinopyroxene (cpx) chemistry in Barby Formation rocks in order to help constrain magma chamber evolution and characterize the complex magma plumbing system. Samples previously collected from well-exposed outcrops of volcanic and hypabyssal intrusions in representative parts of the Barby Formation form the basis for this project (Figure 3). These areas have previously been mapped by TCU workers and are separated by a half graben filled with younger sedimentary rocks. Detailed field and geochemical studies of the Barby Formation in these areas document the eruptive styles and magma compositions of volcanic and associated hypabyssal rocks (Andrews et al., 2016; 2017; Lehman, 2019; Ohrmundt, 2020). Cpx is highly resistant to secondary alteration processes and can provide important petrogenic information in altered igneous rocks (Rossel et al., 2015). Studying cpx compositional variations in the Barby Formation will give additional insights into the magmatic history of this formation. This study uses an electron microprobe to analyze cpx in seven samples collected by Andrews et al. (2016, 2017) and in sixteen samples collected by Ohrmundt (2020) to examine compositional trends and to constrain the magma source chamber characteristics through geothermobarometry.

Regional Geology

The complex geological history in southern Africa starts with rocks in the four main Archean cratons in the region, which are the Angola-Kasai, Kaapvaal, Zimbabwe, and Tanzania cratons (Figure 1) (Hanson, 2003). These cratons are ≥ 2.5 Ga in age and are separated by three younger orogenic systems active during the Paleoproterozoic, Mesoproterozoic, and Neoproterozoic-early Paleozoic. These three orogenic episodes created the Precambrian foundation for the present geologic framework of southern Africa (Hoal, 1993; Hanson, 2003; Miller, 2008). Isotopic ages in the Proterozoic belts range from 2.05-1.8 Ga for the Eburnian orogenic episode, 1.35-1.0 Ga for the Kibaran orogenic episode, and 650-450 Ma for the Pan-African orogenic episode (Hanson, 2003). Older orogenic belts in this region have controlled the placement and shape of younger Proterozoic orogenic belts.

Rocks deformed during the Eburnian orogeny may form the unexposed basement for the Konkiep terrane and may connect with basement inliers in the Pan-African Damaran belt to the north (Miller, 2008; 2012). Paleoproterozoic basement inliers found in the western portion of the Kibaran NNOB have yielded isotopic ages of 1.9-1.7 Ga (Miller, 2008) and include gneisses that have been metamorphosed to upper amphibolite facies (Miller, 2008). The Rehoboth basement inlier (RBI) is exposed Paleoproterozoic crust to the northeast of the Konkiep terrane (Miller, 2008). Much of the RBI is covered by younger sedimentary rocks and Kalahari Desert sands. However, geophysical data show that the Paleoproterozoic rocks extend to the northeast under cover (Miller, 2008; Cornell et al., 2015). Exposed parts of the RBI give U-Pb zircon ages of 1.78-1.74 Ga (Becker et al., 1996).

During the Mesoproterozoic, the Kibaran orogeny stabilized the Congo and Kalahari cratons in southern Africa (Figure 1) (Hanson, 2003). The main belt exposed along the Kalahari

craton margin is the NNOB, which wraps the whole southern margin of the Kalahari craton (Figure 1 and 2). Aeromagnetic anomalies allow exposed NNOB segments to be traced under Phanerozoic cover in South Africa (Hoal, 1993; Hanson, 2003; Miller, 2008). The NNOB records arc magmatism and amphibolite-granulite facies metamorphism along a major convergent margin during assembly of the Rodinia supercontinent (Hanson, 2003; Miller, 2012). Accretion of island arcs was followed by continent-continent collision during this time (Hanson, 2003; Miller, 2012; Cornell et al., 2015).

To the northeast, Mesoproterozoic rocks can be traced using geophysical characteristics through Botswana beneath extensive cover in the Kalahari Desert and connect with the 1.3-1.1 Ga Choma-Kalomo block exposed in Zambia (Hanson et al., 1988). The Umkondo igneous province (UIP) was emplaced at 1.1 Ga and overlaps with younger parts of the NNOB. Widespread tholeiitic gabbroic and diabasic intrusions of this province occur across large parts of the Kalahari craton (Hanson et al., 2004; 2006). Discontinuous, isolated outcrops of 1.1 Ga volcanic and sedimentary rocks are found in the Kalahari Desert in Botswana and can be traced into southwest Namibia along the southern margin of the Damaran belt (Singletary et al., 2003; Miller, 2008). The UIP developed behind the Namaqua-Natal convergent plate boundary and was superimposed on a slightly older Mesoproterozoic orogen within Botswana and eastern Namibia (Hanson et al., 2006). Due to the intraplate setting, the UIP is considered to provide evidence of a rising mantle plume interacting with stresses from the Namaqua-Natal plate boundary during Rodinia formation (Hanson et al., 2006).

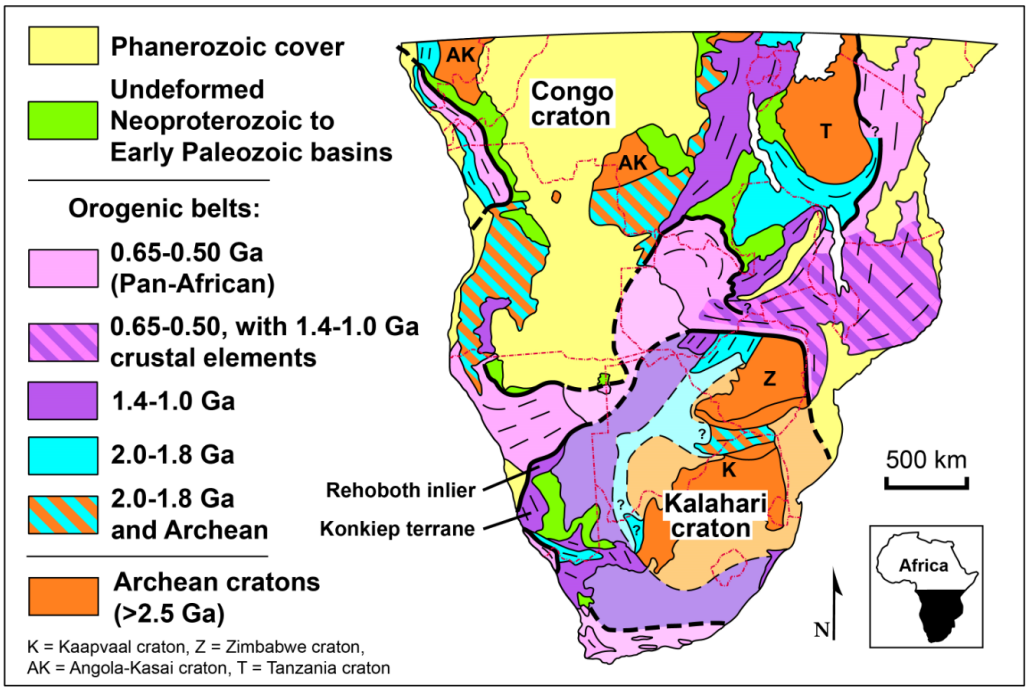

Figure 1. Major Precambrian orogenic belts and cratons in southern Africa. Modified from Hanson (2003) and Singletary et al. (2003).

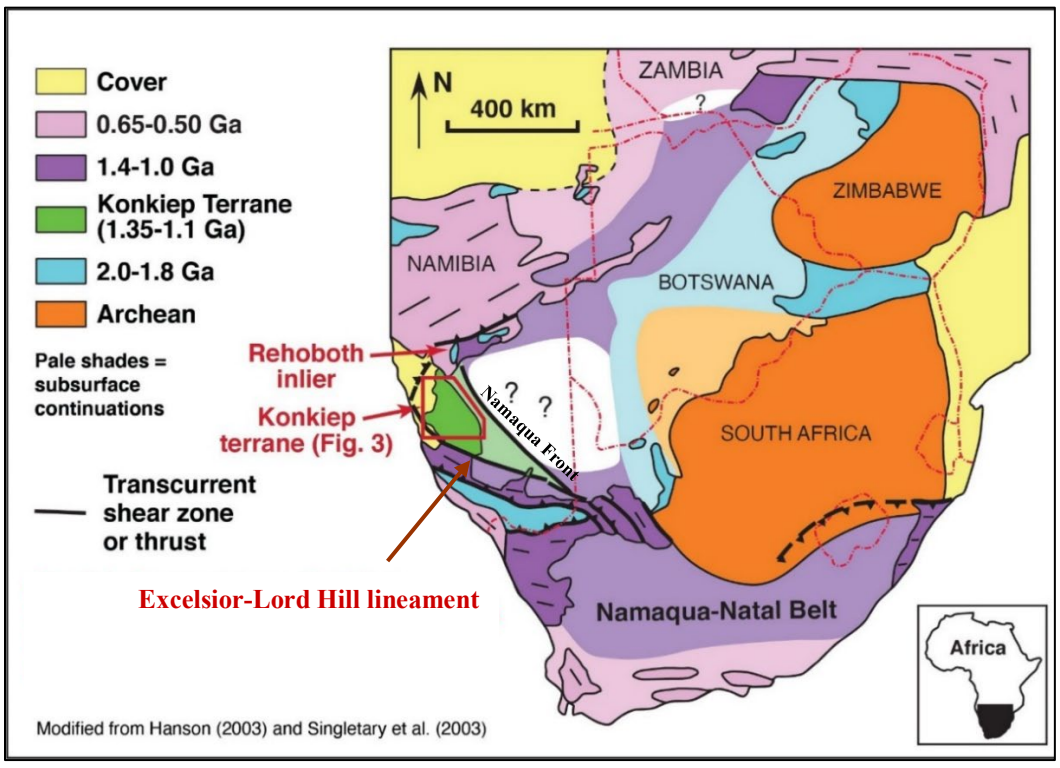

Figure 2. Close up of southern Africa showing the study area in southern Namibia. Modified from Hanson (2003) and Singletary et al. (2003).

Konkiep Terrane

The wedge-shaped Konkiep terrane represents Mesoproterozoic rocks making up a major part of the NNOB in Namibia, near the western margin of the Kalahari craton (Miller, 2008; Panzik et al., 2016). U-Pb zircon isotopic dating yields ages of 1.4-1.1 Ga for the terrane. The terrane is bounded in the south by the Excelsior-Lord Hill lineament and by the Namaqua front in the northeast (Figure 2) (Corner, 2008; Miller, 2008). The Namaqua front represents the site where accretion of the Konkiep terrane took place against the Kalahari craton (Miller, 2012). The Namaqua front is juxtaposed to the northeast against the quiet aeromagnetic signature of assumed Paleoproterozoic crust related to the RBI in the subsurface (Miller, 2012; Cornell et al., 2015). In contrast to the RBI signature, very strong and irregular magnetic anomalies can be detected throughout the Konkiep terrane (Corner, 2008; Miller, 2008).

Stratified rocks in the terrane were included within the Konkiep Group by Miller (2008), which comprised the Kairab Formation, coeval Nagatis and Welverdiend Formations, Kunjas Formation, coeval Barby and Haiber Flats Formations, Guperas Formation, and the Aubures Formation at the top of the sequence (Figure 3). More recently, the Konkiep Group has been replaced by three separate groups separated by regional unconformities (Cornell et al., 2020). Each of these groups represents changes in tectonic environment. The Betta Group includes the Nagatis and Welverdiend Formations and records rifting from 1.36-1.33 Ga, which split the RBI (Malobela et al., 2019). The Vergenoeg Group includes the 1.2 Ga Barby and coeval Haiber Flats Formations and records volcanic arc activity. The Ganaams Group includes the 1.1 Ga Guperas Formation, which is an extension of the UIP, and the overlying sedimentary Aubures Formation (Malobela et al., 2019; Cornell et al., 2020). Most of these rocks in general show unusually low-grade metamorphism (zeolite and prehnite-pumpellyite facies) compared to other

rocks within the NNOB, and they preserve a much better record of geological history in the orogen (Miller, 2008). Together with coeval units in the RBI, they make up the Sinclair Supergroup (Miller, 2008).

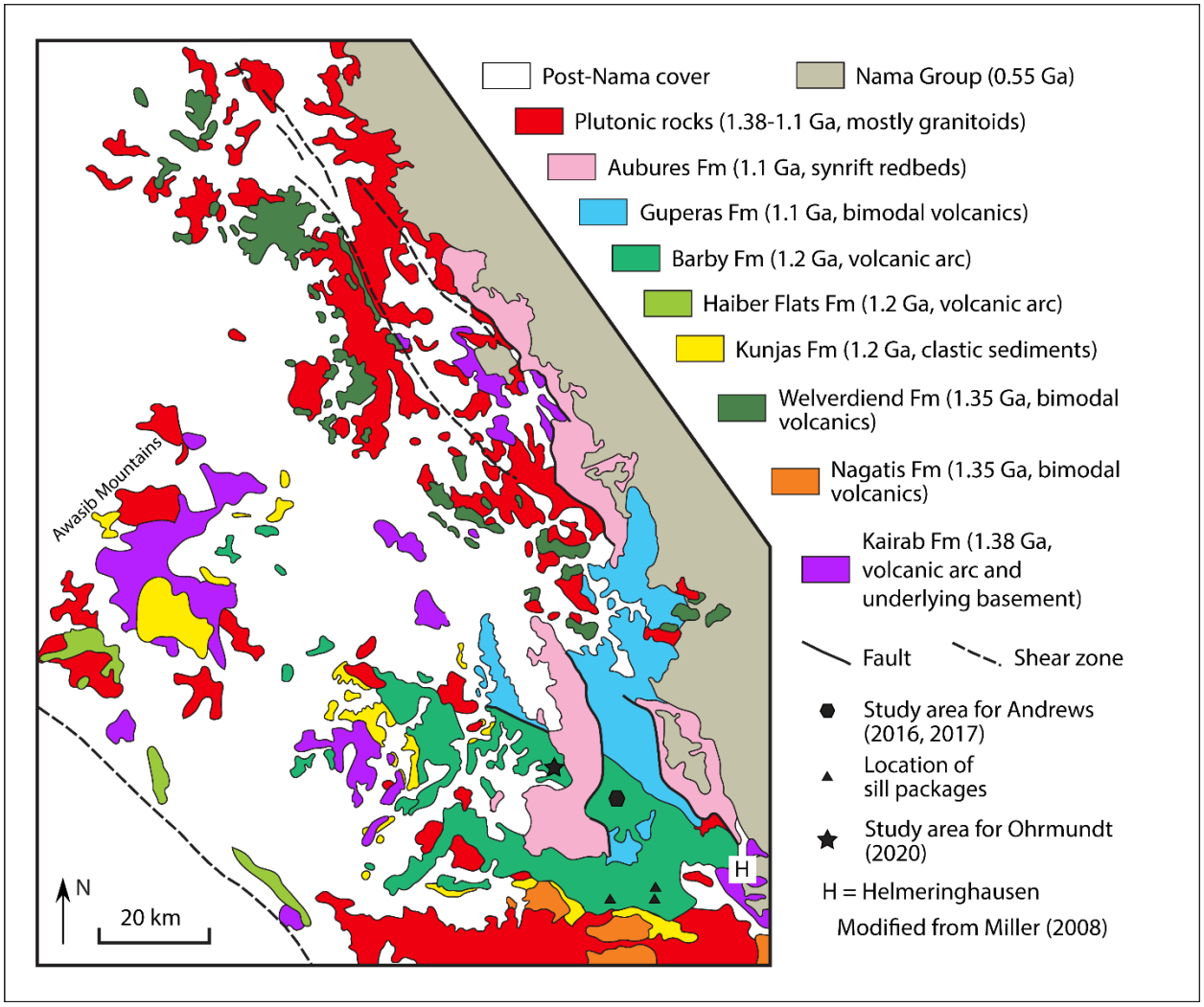

Figure 3. Geologic map of the Konkiep terrane modified from Miller (2008). Field areas from previous TCU studies are indicated within the Barby Formation. Rocks collected from these sites are the focus of this study.

In some areas of the Konkiep terrane, the basal unit is the metavolcanic Kairab Formation. Due to Phanerozoic cover, rocks within the Kairab Formation are poorly exposed. Partly bimodal metavolcanic rocks within the unit range from basaltic to rhyolitic in composition and are up to 4000 m thick in the Awasib Mountains (Figure 3) (Miller, 2008). The Kairab

Formation generally shows stronger deformation and a higher grade of metamorphism than other units in the Konkiep terrane and is considered to represent early-stage crustal development in the terrane (Hoal, 1989). Chemical analyses done by Hoal (1990) indicate compositions typical of tholeiitic island arcs, supporting a model of island-arc accretion during the Mesoproterozoic (Miller, 2008; 2012).

Located in the southeast part of the Konkiep terrane, the Nagatis Formation crops out in a belt trending northwest. Unlike the Kairab Formation, the Nagatis Formation has outcrops only in the Helmeringhausen area (Figure 3). Bounded by two unconformities, the Nagatis Formation rests on top of an older granodiorite and is overlain by the Kunjas Formation (Miller, 2008). The majority of the Nagatis Formation is dominated by A-type rhyolites, interbedded ignimbrites, and minor sedimentary rock sequences (Miller, 2008; Lehman, 2019). Some evidence of rheomorphism is shown by the rhyolites (Miller, 2008; 2012). In the southeastern corner of the Nagatis Formation, the Gamochas caldera is composed of quartz-phyric rhyolites and minor tholeiitic basalts within ring faults; basaltic dikes also occur (von Brunn, 1969; Miller, 2008; Lehman, 2019). U-Pb zircon dating by Harris et al. (2020) places this unit at 1.36 Ga, making it among the oldest undeformed units within the Sinclair Supergroup. Mafic rocks came from depleted mantle sources, whereas felsic rocks contain large amounts of crustal components with subduction signatures inherited from older crust (Lehman, 2019; Harris et al., 2020).

The Welverdiend Formation occupies a discontinuous belt trending northwest-southeast and is exposed in the northern portion of the Konkiep terrane (Miller, 2008). Roughly coeval with the Nagatis Formation, the Welverdiend Formation is ~5.1 km thick and is bimodal in composition with tholeiitic basalts and basaltic andesites intercalated with flow-banded rhyolites and pyroclastic deposits (Brown and Wilson, 1986; Miller, 2008; Cornell et al., 2015). U-Pb

zircon dating done by Cornell et al. (2015) and Harris et al. (2021) yield ages of 1.34-1.33 Ga for the unit. It is inferred that the Nagatis and Welverdiend Formations formed within a continental rift setting (Cornell et al., 2020).

The Kunjas Formation rests uncomformably on top of the Nagatis Formation, west of the Helmeringhausen area (Miller, 2008). It is composed of polymict sedimentary breccia, conglomerate, and interbedded siltstone, shale, and sandstone layers. Planar and trough cross-bedding is present throughout, as well as consistent fining-upward packages, indicating fluvial deposition (Miller, 2008; 2012). In the Awasib Mountains, conglomerate clasts are predominately granitic and quartzite in composition. Deposition of the Kunjas sediments was followed by the second main volcanic phase forming a new continental margin arc (Cornell et al., 2015; Malobela et al., 2019).

The Barby Formation, which is the subject of this study, stretches 90 km along strike northwest-southeast and is 8.5 km thick. It comprises mainly calc-alkaline to shoshonitic basaltic andesites and andesites with intercalated lacustrine sediments and minor rhyolitic lava flows (Watters, 1974; Miller, 2008; Ohrmundt, 2020), and will be discussed in more detail later. Watters (1974) describes the contact between the Kunjas and Barby Formations as disconformable in the north to conformable in the south. U-Pb zircon dating yields ages of 1.22-1.21 Ga for these volcanic rocks (Malobela et al., 2019).

Coeval with the Barby Formation, the Haiber Flats Formation is oriented northwest-southeast and located further west, closer to the Excelsior-Lord Hill lineament. The Haiber Flats Formation is composed of volcanic rocks that disconformably overlie the Kunjas strata (Miller, 2008) and range in composition from basaltic andesite to rhyolite. The volcanic rocks are strictly calc-alkaline in composition and compose up to 90% of the formation (Hoal, 1993). Some

volcaniclastic sedimentary rocks found in the Haiber Flats Formation are the erosional remnants of extrusive rocks. Trace element relationships are characteristic of hydrous melts in arc settings (Lehman, 2019). Heterogeneity of Zr concentrations between the Kairab, Barby and Haiber Flats Formations indicates that the volcanic rocks in these formations come from either two different mantle sources or from different degrees of partial melting of the mantle source rock (Hoal, 1990; Miller, 2008; Lehman, 2019). As shown by Hoal (1990), rocks within the Haiber Flats Formation are laterally discontinuous, and therefore cannot be correlated throughout the Awasib Mountains (Miller, 2008).

The Guperas Formation begins the third main magmatic cycle at ~1.1 Ga. It is the youngest volcanic formation, lies unconformably on the Barby and Welverdiend Formations, and occupies north-trending grabens. Rhyolitic lava flows, pyroclastic deposits, and minor basalt flows are interfingered with matrix-supported conglomerates and lithic sandstones (Miller, 2008). Volcanic and sedimentary rocks in the Guperas Formation are cut by a bimodal dike swarm with felsic and mafic members (Cornell et al., 2020). U-Pb zircon dating of these dikes places the intrusions at 1.1 Ga (Panzik et al., 2016; Cornell et al., 2020). The dikes also yield paleomagnetic poles that are similar to poles for the Guperas Formation and coincide with poles for the UIP, providing evidence that the Guperas Formation and the dike swarm formed from the Umkondo mantle heating event (Panzik et al., 2016; Cornell et al., 2020).

The Aubures Formation constitutes the final Mesoproterozoic unit within the Konkiep terrane. It is ~2600 m thick and was deposited in two elongate half grabens trending north-northwest located on the eastern side of the Konkiep terrane (Figure 3) (Watters, 1974; Miller, 1969; 2008). Characteristic redbeds in the formation begin with a poorly sorted basal conglomerate that fines upwards into well sorted, fine- to very fine-grained, feldspathic

sandstones, shales, and siltstones (Miller, 1969; 2008). Fluvial deposition is indicated by common tabular and trough cross beds, mud cracks, and clay pellet impressions (Miller, 2008). U-Pb dating of detrital zircons in the unit provides a maximum sedimentation age of 1108 Ma. A palaeomagnetic analysis of the Aubures Formation yielded a primary pole that places deposition of the formation between poles from the UIP and the ~1090 Ma Kalkpunt Formation in South Africa, confirming the Konkiep terrane was attached to the western margin of the Kalahari craton by at least 1.1 Ga (Kasbohm et al., 2016).

Recent Work on the Barby Formation

Previous workers concluded that the Barby Formation consists mainly of lava flows and less abundant hypabyssal intrusive rocks (Watters, 1974; Miller, 2008). More recently TCU workers have documented abundant pyroclastic rocks formed from small, monogenetic volcanoes intercalated with lacustrine sequences in representative parts of the formation (Figures 4-7) (Lehman et al., 2016; Andrews et al., 2016; 2017; Hanson et al., 2018; Ohrmundt, 2020). Andrews et al. (2016, 2017) carried out reconnaissance mapping to the east of one of the half grabens within which the Aubures Formation was deposited, along with more detailed mapping in parts of that study area. Ohrmundt (2020) documented volcanic rocks and hypabyssal magma plumbing systems in a smaller area, 2.5 by 2 km, on the other side of the Aubures half graben (Figure 3).

Field work in both TCU study areas shows abundant pyroclastic fall deposits up to 80 m thick that are interbedded with lacustrine sedimentary rocks consisting mostly of planar-laminated volcaniclastic mudstones, siltstones, and sandstones (Figures 4-7). Lava flows occur in places, but are much less common (Figure 5). Hawaiian, Strombolian, and phreatomagmatic eruptions occurred in a topographically low environment with abundant lakes (Andrews et al.,

2016; Ohrmundt, 2020*).* Varying magma ascent rates controlled the eruption style at shallow depths by dictating the magma to external water ratio, which resulted in major Hawaiian-style spatter deposits changing upward into Strombolian deposits with dispersed ribbon and fusiform bombs or into phreatomagmatic deposits with cauliflower bombs and poorly vesicular angular lapilli (Andrews et al., 2016).

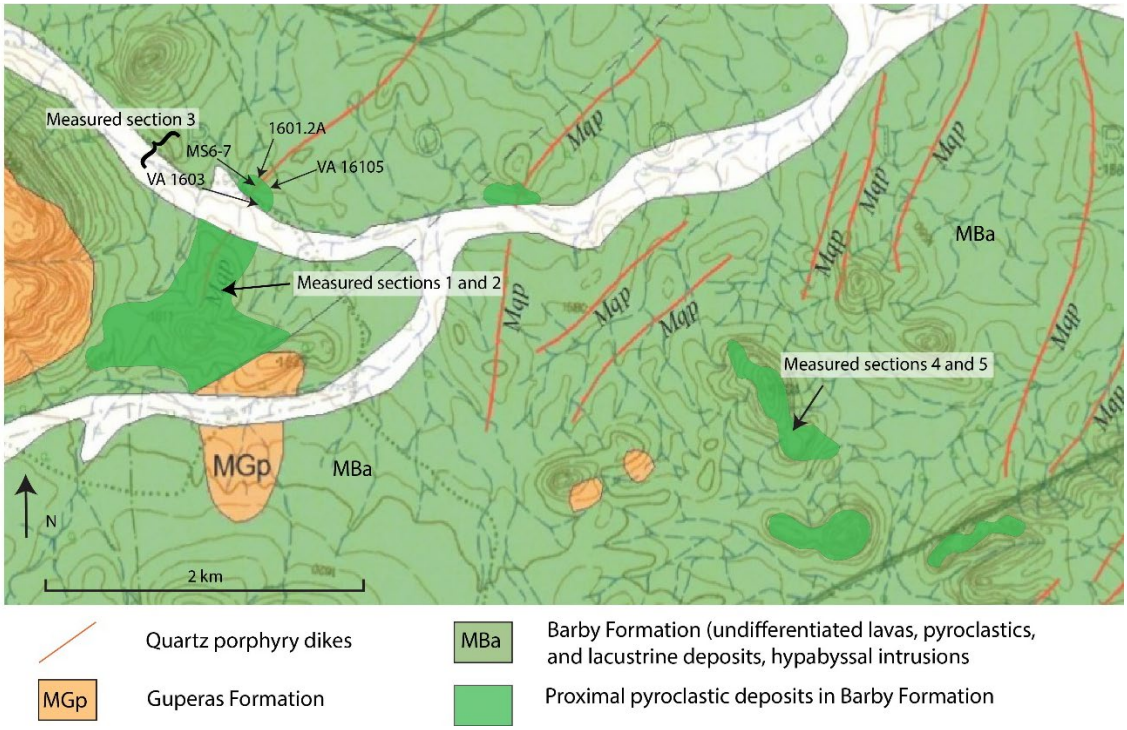

Figure 4. Map of Andrews et al. (2016) field area to the east of the Aubures half graben. Base map is from Watters (1974). Measured sections are shown in Figure 5.

Pyroclastic fall deposits in some cases form massive, bomb-rich cliffs (Figures 6 and 7) which are typically separated by lacustrine sequences 10-60 m thick with some bedded lapillistone and lapilli tuff. Bombs reach up to 1 m in diameter and are fluidal to ellipsoidal in shape, indicating Hawaiian to Strombolian eruptions. Bomb sags occur in some of the underlying units (Ohrmundt, 2020).

Hypabyssal intrusions commonly crosscut bomb-rich units, lacustrine sediments, and pyroclastic fall deposits throughout the study areas (Andrews et al., 2016; 2017; Ohrmundt, 2020). Tabular dikes and sills intrude bomb-rich units, but more irregular intrusive geometries occur in the lacustrine and pyroclastic fall deposits (Ohrmundt, 2020). An intrusion in the pyroclastic sequence shown in measured section 3 (Figure 5) is characterized by fluidal, billowy contacts against the pyroclastic deposits. These features indicate that the intrusion was emplaced shortly after the pyroclastic material was deposited. Sill packages occur in places within thick lacustrine sediments (Figures 3, 8, and 9) to the southeast of the area shown in Figure 4. These sills were inferred by Andrews et al. (2017) to have been fed from basaltic to andesitic dikes that could not penetrate the low-density sediments due to buoyancy constraints.

Sills in lacustrine deposits show undulatory, chilled margins and zones of peperite where quenched magma intermixed with the sediment. Chilled margins of the sills cracked allowing wet sediments to become fluidized and inject into the margins forming sediment tendrils. All these features indicate interaction between magma and wet, unconsolidated sediments (Andrews et al., 2016; 2017; Ohrmundt, 2020). Sill packages 1 and 2 each consist of five individual sills separated by lacustrine sediments. Sill package 3 consists of six individual sills with sill 2 intruding into sill 1. Sill 4 in this sill package also is penetrated by a small, plagioclase-rich intrusion. Zones of magma mingling are found in each sill package indicating that some sills were formed from more than one batch of magma. Locations of samples taken from these sill packages are shown in Figure 9.

Intrusive pyroclastic rocks up to 30 m thick (Figures 6 and 7) form massive, structureless units and meter-scale dikes of pyroclastic material that in some cases encase tabular lacustrine

sediment masses or show mixing with sediment along their margins. Pyroclasts in the intrusive units have similar textures to those shown by the extrusive pyroclasts (Ohrmundt, 2020).

Five phreatomagmatic diatremes that acted as feeder conduits to small maar volcanoes are described by Ohrmundt et al. (2019) and Ohrmundt (2020). The diatremes have elliptical outlines 60-120 m across (Figures 6 and 7) and are filled with a chaotic mixture of bombs, blocks, lapilli, spatter, disaggregated sand and mud, and tabular bodies of lacustrine sediment and pyroclastic deposits. This wide variety of material within the diatremes indicates explosive behavior with varying combinations of magmatic volatile release and conversion of pore water into steam within the wet sediments. It also indicates recycling of material that was erupted out, then fell back into the conduit and was erupted out again (Houghton and Smith, 1993). Recycled material erupted out of the vent would have slowly widened the diatreme by collapsing the walls and ejecta rims.

Previous TCU graduate students analyzed whole-rock geochemistry for samples from both study areas, including the sill packages. Lehman (2019) analyzed major and immobile trace elements in twenty-nine samples of the Barby Formation collected from the study area east of the Aubures half graben (Andrews' field area). Additional geochemistry performed by Ohrmundt (2020) for samples in her study area shows close similarities to the samples collected further east, indicating similar petrogenic histories for the Barby igneous rocks in both areas.

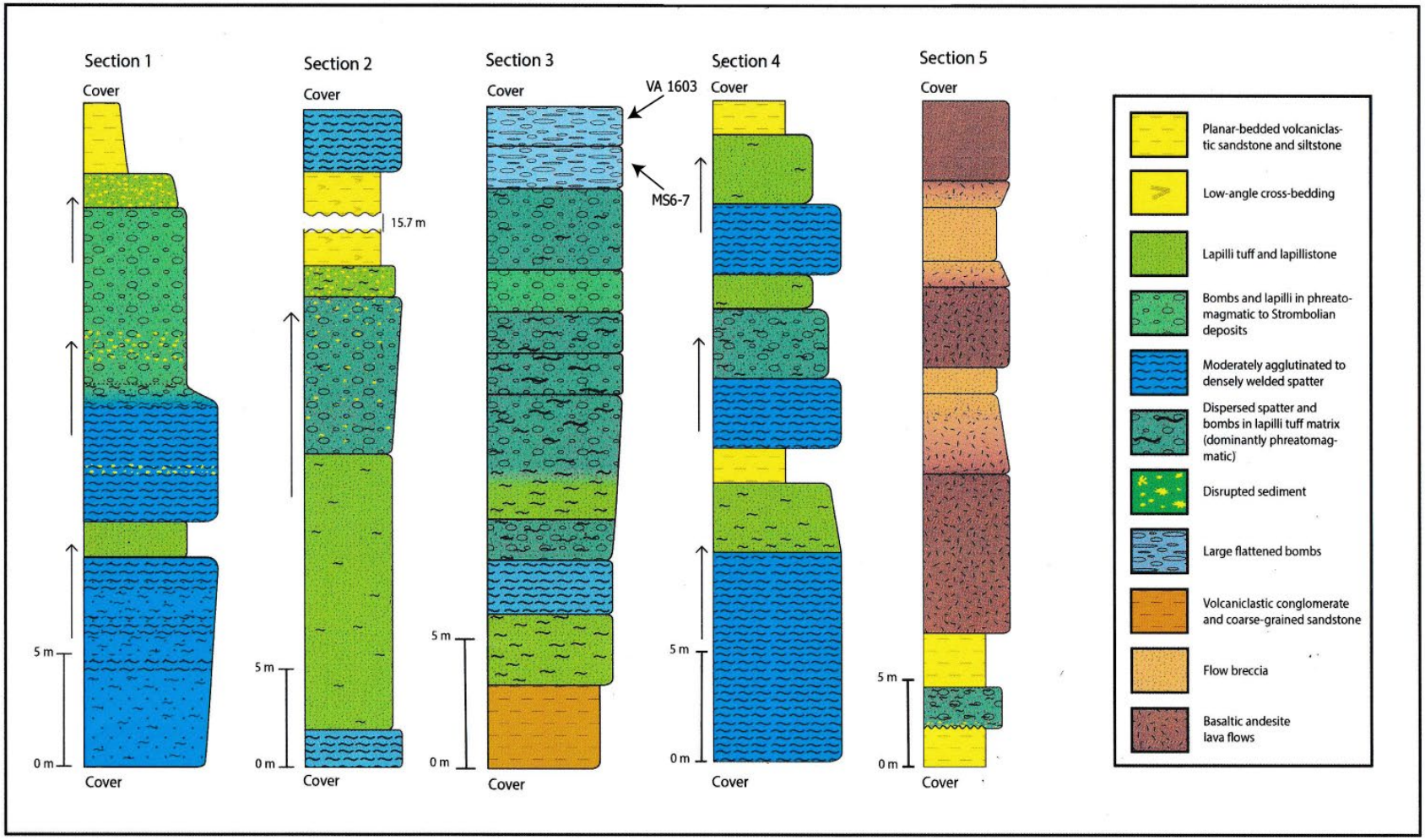

Figure 5. Measured sections done by Andrews et al. (2016). Arrows pointing upwards indicate an increase in phreatomagmatic activity. See Figure 4 for locations of measured sections.

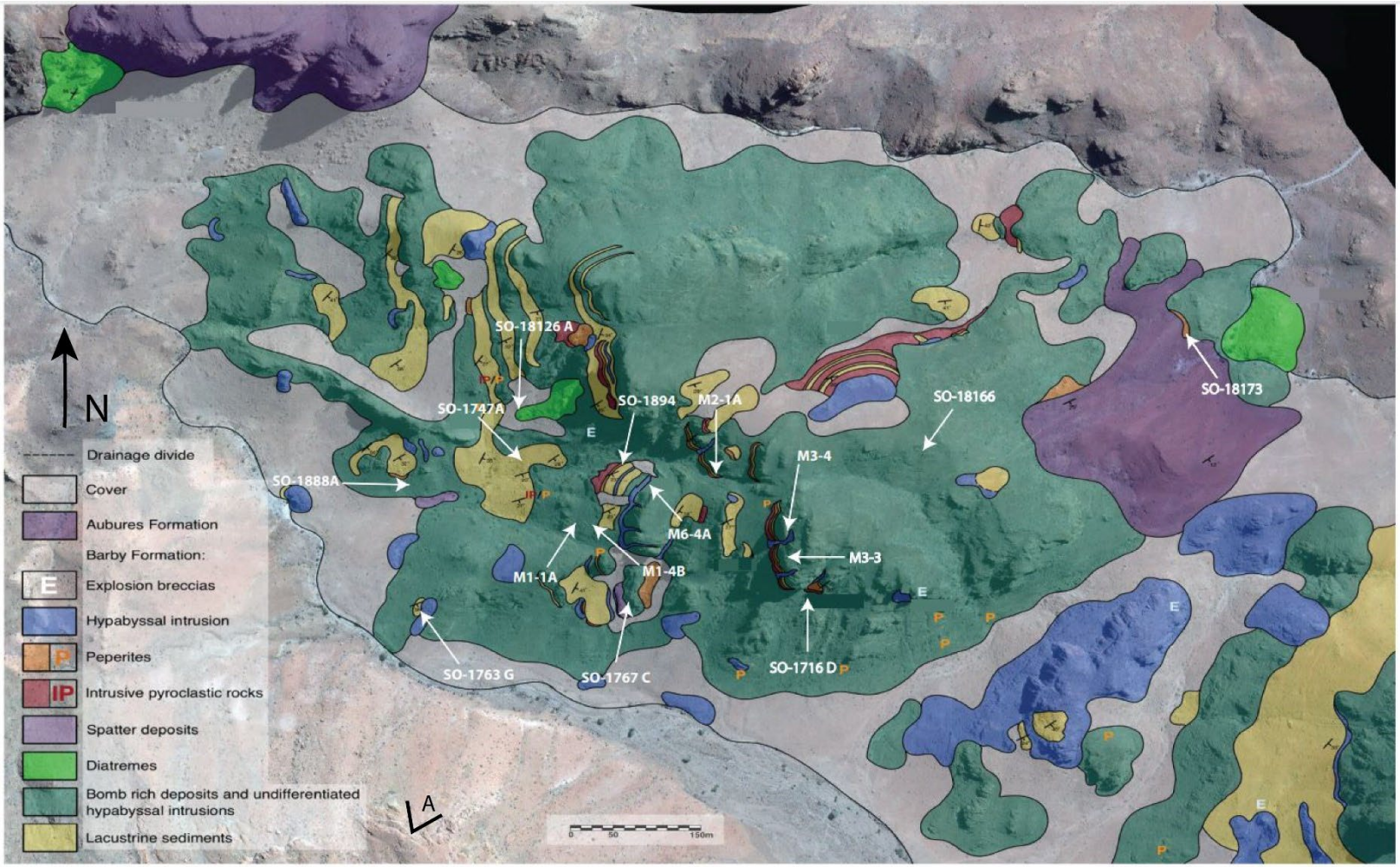

Figure 6. Map modified from Ohrmundt (2020) of the Barby Formation in a well exposed area to the west of the Aubures half graben (Figure 3). White arrows indicate locations of samples analyzed in this study. A= location of panoramic photo shown in Figure 7.

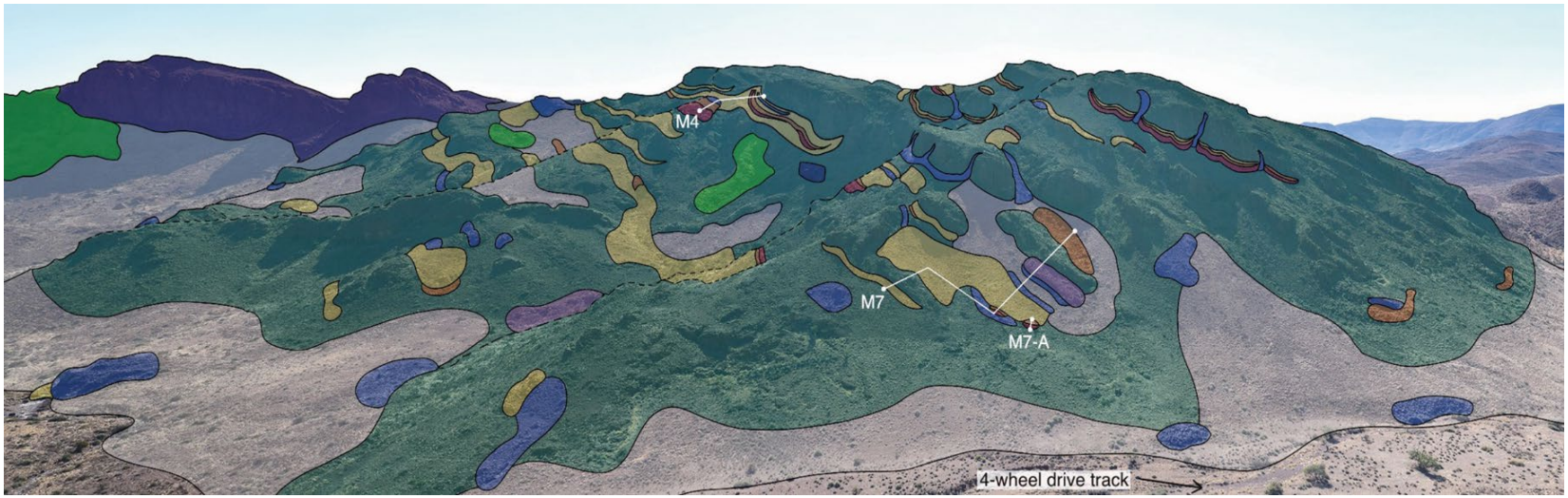

Figure 7. Oblique view of Ohrmundt's (2020) field area. Legend is the same as in Figure 6. Photo taken from west edge of the map in Figure 6 looking northeast from point A. Labels in photo represent locations of measured sections done by Ohrmundt (2020) and do not pertain to this project.

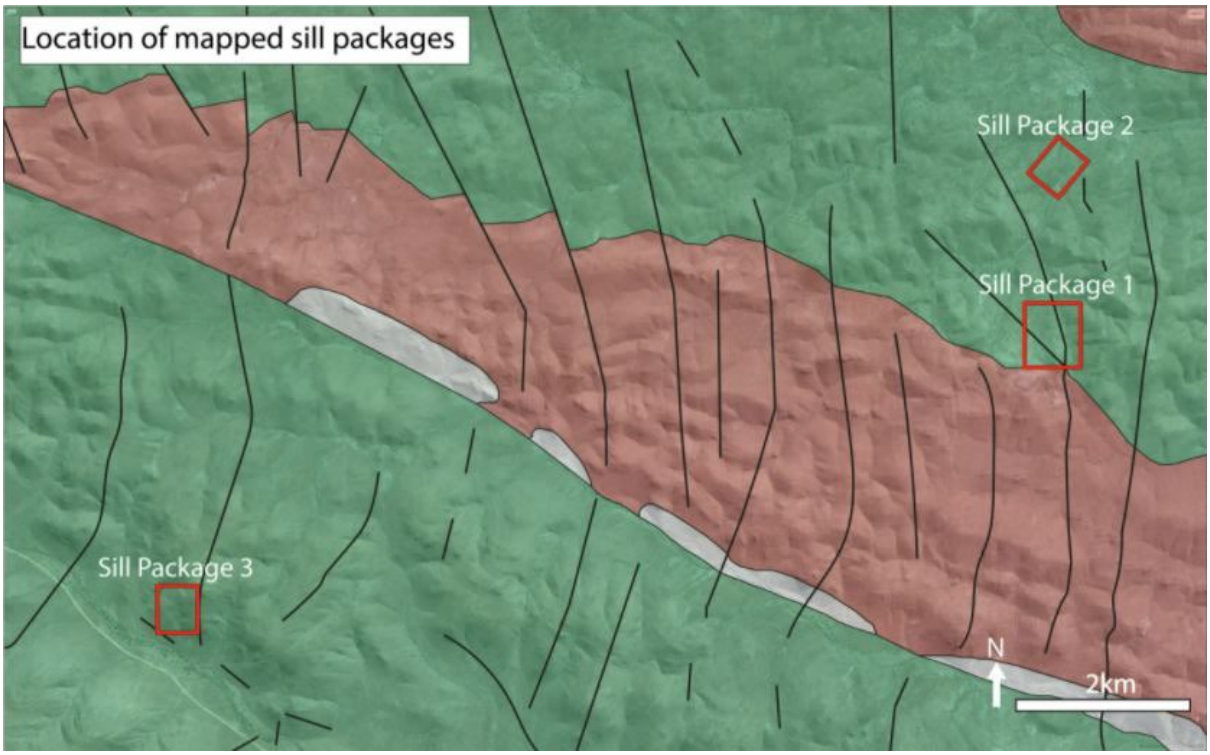

Figure 8. Locations of mapped sill packages. See Figure 3 for general location with respect to other study areas in the Barby Formation. Map is from von Brunn (1969). Green = typical Barby Formation (lavas, pyroclastic deposits, etc.); brown = sandstone and tuff in the Barby Formation, in fault contact to the south with the typical Barby Formation; grey = Kunjas Formation. Heavy black lines are other faults.

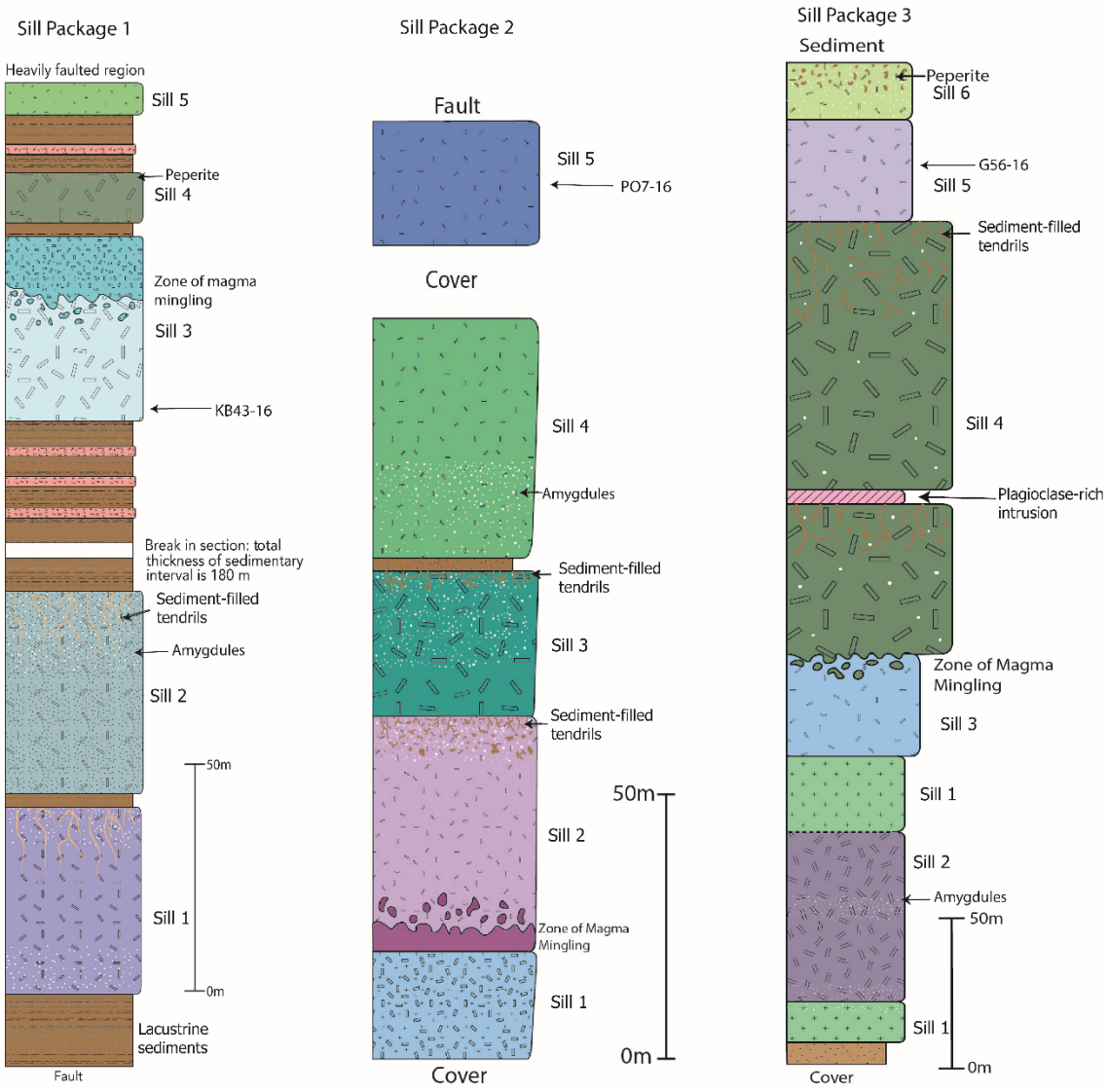

Figure 9. Measured sections of sill packages 1-3 in Figure 8 (Andrews and Hanson unpublished data), showing location of samples analyzed in the present study. Brown color represents lacustrine sediment.

Whole-rock Chemistry for the Barby Formation

Whole-rock geochemical data from Lehman (2019) and Ohrmundt (2020) for samples used in the present study are shown in Figures 10-19. Colored fields in those figures encompass data for all the samples analyzed by Lehman (2019) and Ohrmundt (2020). Harker variation diagrams indicate a decrease in CaO, MgO, and FeO with increasing silica content (Figures 10-

12). This is consistent with fractionation of phenocrysts of olivine and cpx, which are the main phenocrysts present. On the other hand, TiO_2, Na_2O, and K_2O show scattered data with increasing silica content (Figures 13-15), which reflects mobility of some of these elements and SiO_2 during alteration.

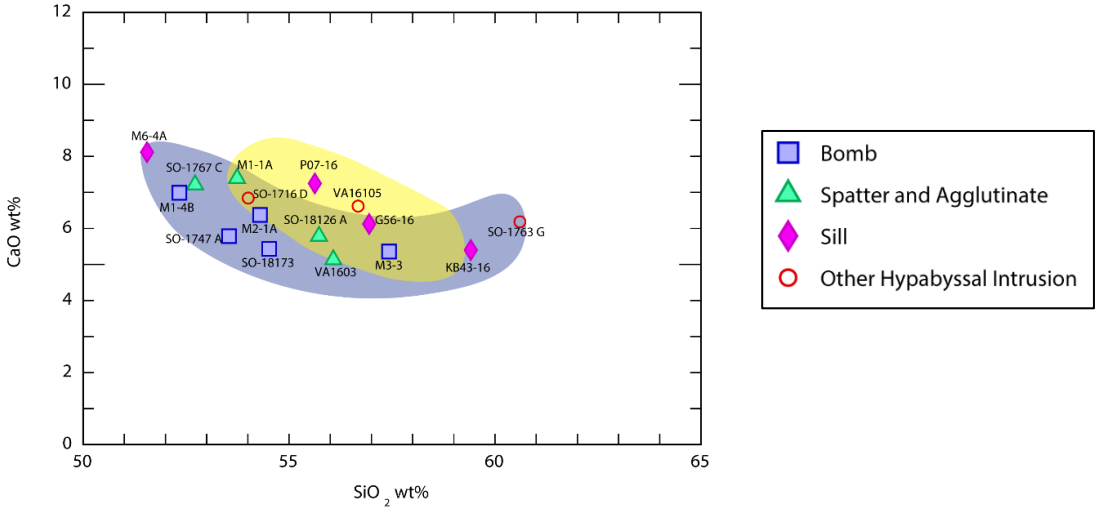

Figure 10. Harker variation diagram for CaO. Blue field represents samples from Ohrmundt (2020) and yellow field represents samples from Lehman (2019).

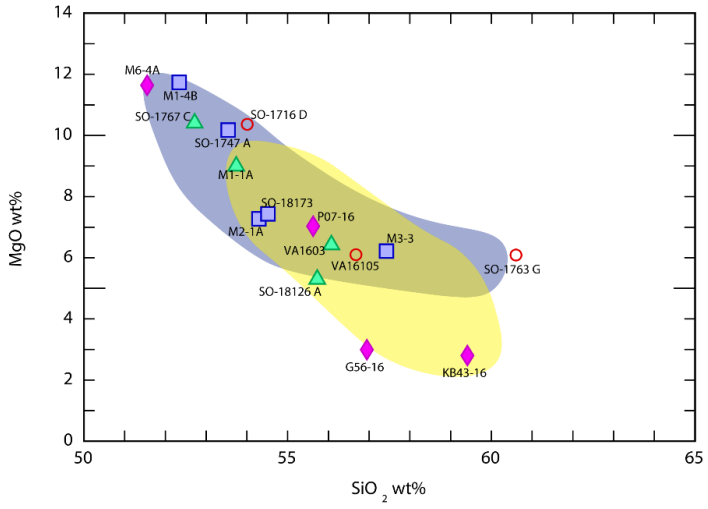

Figure 11. Harker variation diagram for MgO. See Figure 10 for explanation of fields and legend.

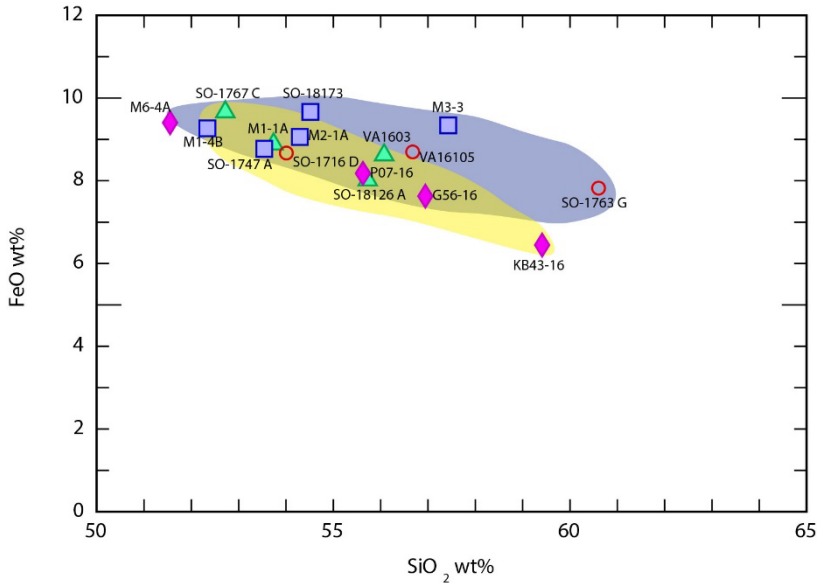

Figure 12. Harker variation diagram for FeO. See Figure 10 for explanation of fields and legend.

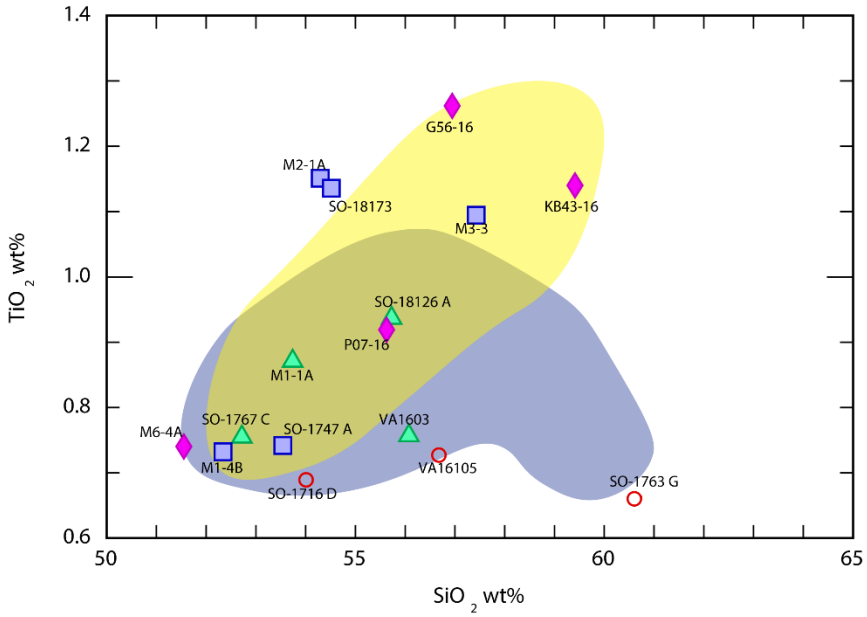

Figure 13. Harker variation diagram for TiO_2. See Figure 10 for explanation of fields and legend.

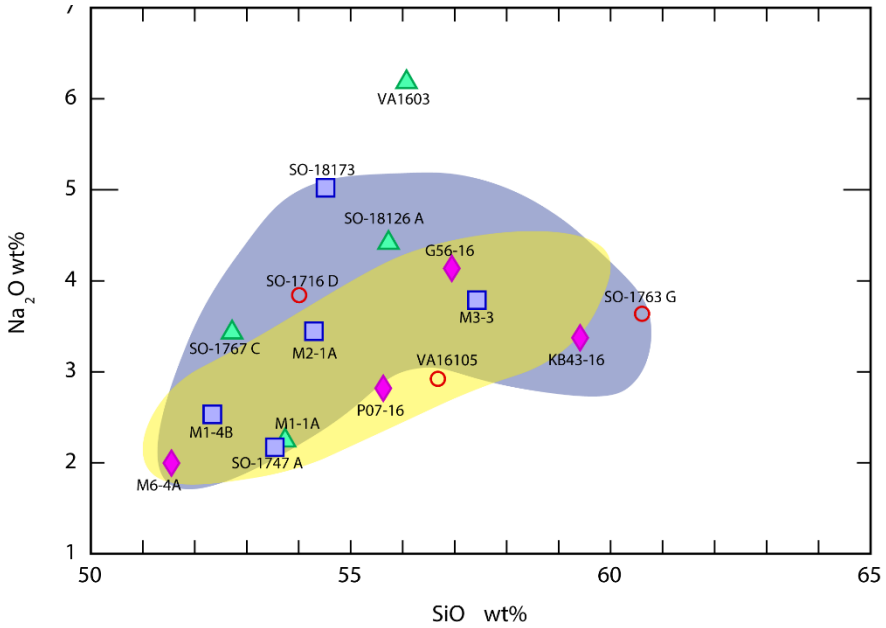

Figure 14. Harker variation diagram for Na_2O. See Figure 10 for explanation of fields and legend.

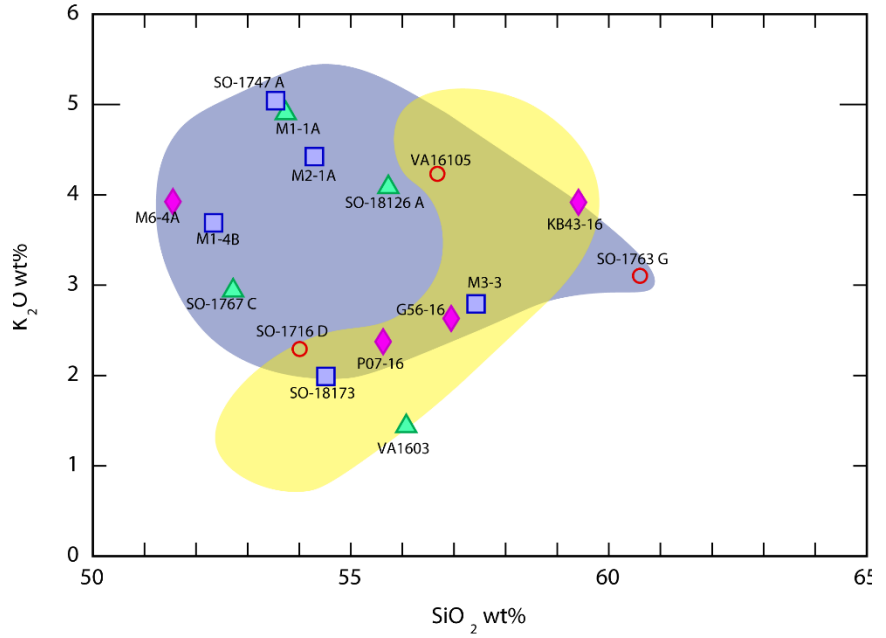

Figure 15. Harker variation diagram for K_2O. See Figure 10 for explanation of fields and legend.

All samples plot within fields for subalkaline andesite and basaltic andesite in Figure 16, which uses trace elements that are resistant to alteration. Figures 17 and 18 show that the samples

cluster tightly together in calc-alkaline fields on standard discrimination diagrams. Figure 19 shows that the samples cluster on the border between calc-alkaline andesites to shoshonites with the majority of the samples plotting in the shoshonitic field.

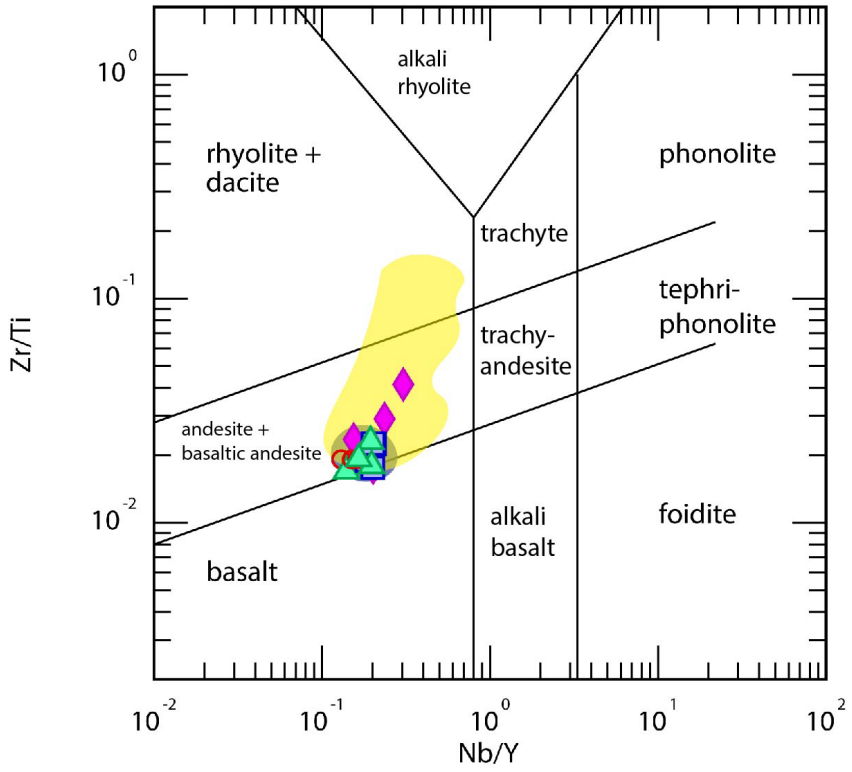

Figure 16. Nb/Yb vs. Zr/Ti classification diagram from Pearce (1996). See Figure 10 for explanation of fields and legend.

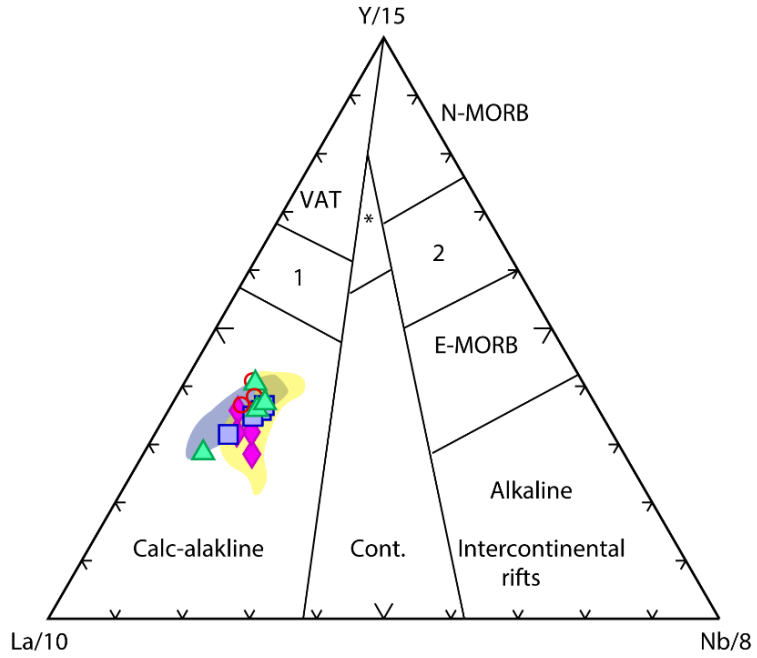

Figure 17. La/10-Y/15-Nb/8 discrimination diagram from Cabanis and Lecolle (1989). VAT: volcanic arc tholeiite; N-MORB: normal mid-ocean ridge basalt; E-MORB: enriched mid-ocean ridge basalt; Cont.: Continental; 1 represents overlap between calc-alkaline and VAT; 2 represents weakly enriched MORB; *: back arc basalts. See Figure 10 for explanation of fields and legend.

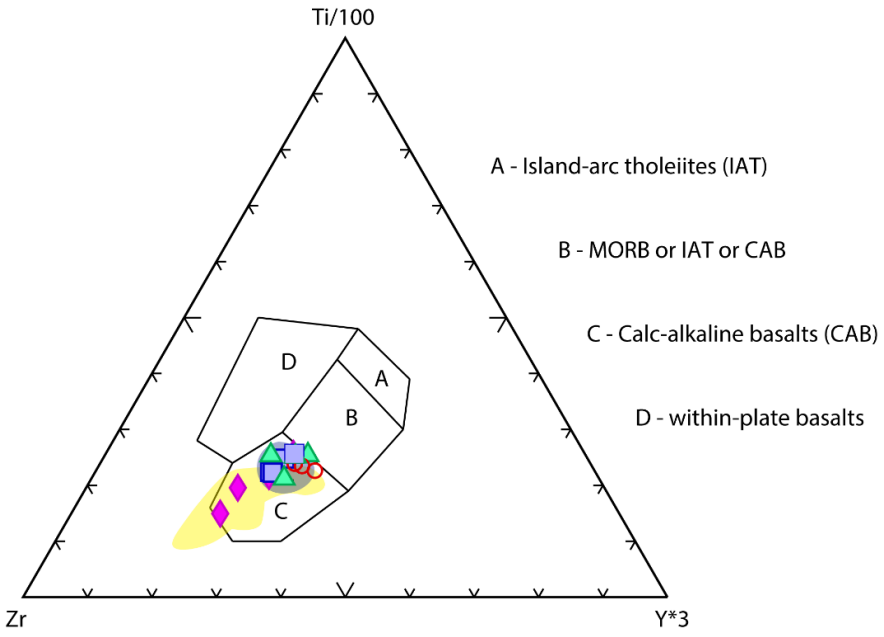

Figure 18. Zr-Ti/100-Y*3 discrimination diagram from Pearce and Cann (1973). See Figure 10 for explanation of fields and legend.

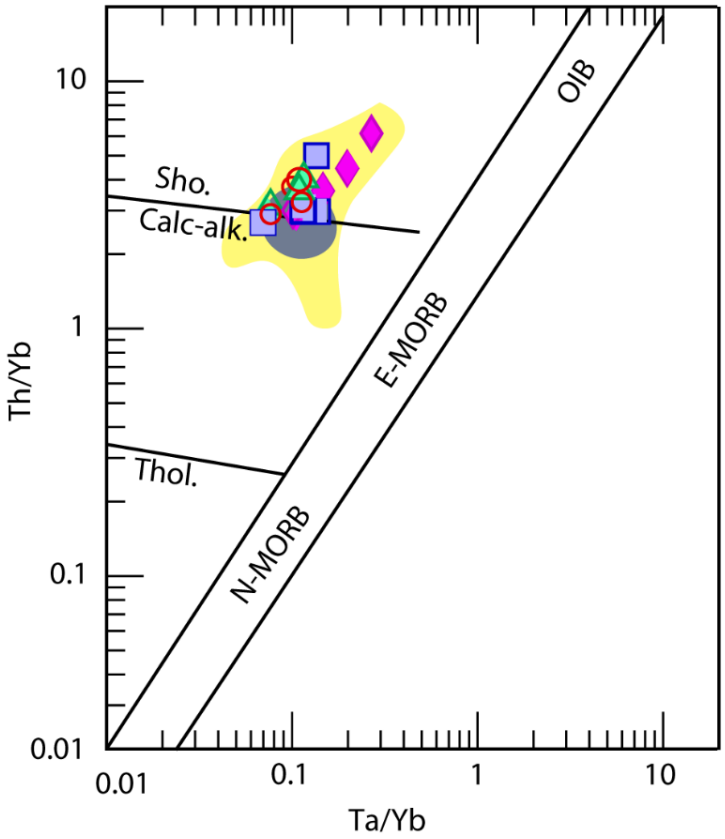

Figure 19. Ta/Yb vs. Th/Yb discrimination diagram from Pearce (1982). N-MORB: normal mid-ocean ridge basalt; E-MORB: enriched mid-ocean ridge basalt; OIB: ocean island basalt; Thol.: tholeiite; Calc-alk.: calc-alkaline; Sho.: shoshonite. See Figure 10 for explanation of fields and legend.

II. METHODOLOGY

Petrographic studies on standard thin sections were used to visually estimate phenocryst and vesicle percentages. Scanning electron microscope (SEM) images of cpx were taken to compare the textures seen with optical microscopy. Sample locations are given in Table 1. A wide range of samples were analyzed, including spatter and agglutinate, bedded lapillistone, bombs in pyroclastic deposits, one bomb in a diatreme feeder conduit, one bomb within intrusive pyroclastic rocks, and hypabyssal intrusions including sills and fluidal, irregular bodies. Not all samples used in this study have whole-rock chemical analyses, and the additional samples

analyzed here for cpx chemistry provide useful new information on petrogenetic relations in the Barby Formation.

Table 1. Sample locations. CA = chemical analysis done for whole-rock

Sample	CA	Rock Type	Field Area	Latitude	Longitude
KB43-16	Yes	Sill from sill package 1	Andrews	-25°51’22”	16°40’03”
PO7-16	Yes	Sill from sill package 2	Andrews	-25°50’31”	16°40’08”
G56-16	Yes	Sill from sill package 3	Andrews	-25°52’37”	16°35’18”
M6-4	Yes	Sill	Ohrmundt	-25°40'06"	16°29'49"
VA 1603	Yes	Spatter and agglutinate	Andrews	-25°43’30”	16°34’42”
SO-18126 A	Yes	Spatter and agglutinate	Ohrmundt	-25°40'02"	16°29'43"
SO-1767 C	Yes	Spatter and agglutinate	Ohrmundt	-25°40'14"	16°29'49"
M1-1A	Yes	Spatter and agglutinate	Ohrmundt	-25°40'09"	16°29'46"
VA 16105	Yes	Hypabyssal intrusion	Andrews	-25°43’34”	16°34’48”
SO-1716 D	Yes	Hypabyssal intrusion	Ohrmundt	-25°43’13”	16°29’59”
SO-1763 G	Yes	Hypabyssal intrusion	Ohrmundt	-25°40’15”	16°29’43”
M3-4	No	Hypabyssal intrusion	Ohrmundt	-25°40'08"	16°29'57"
SO-1888 A	No	Hypabyssal intrusion	Ohrmundt	-25°40'07"	16°29'36"
SO-1894	No	Hypabyssal intrusion	Ohrmundt	-25°40’05”	16°29’46”
SO-18166	No	Hypabyssal intrusion	Ohrmundt	-25°40’05"	16°30'08"
MS6-7	No	Pyroclastic bomb	Andrews	-25°43’29”	16°34’43”
M1-4B	Yes	Pyroclastic bomb	Ohrmundt	-25°40'09"	16°29'47"
M2-1A	Yes	Pyroclastic bomb	Ohrmundt	-25°40'05"	16°29'53"
M3-3	Yes	Pyroclastic bomb	Ohrmundt	-25°40'09"	16°29'57"
SO-18173	Yes	Pyroclastic bomb	Ohrmundt	-25°39'57"	16°30'26"
SO-18176 B	No	Pyroclastic bomb	Ohrmundt	-25°39'51"	16°30'11"
SO-1747 A	Yes	Pyroclastic bomb	Ohrmundt	-25°40’06”	16°29’43”
1601.2A	No	Bedded lapillistone	Andrews	-25°43’28”	16°34’45”

Electron Microprobe Analysis

Electron microprobe analysis (EPMA) was conducted under the supervision of Dr. Steven Singletary. Data were collected from twenty-three samples using the JEOL JXA-8530F electron microprobe at the Southeastern North Carolina Regional Microanalytical and Imaging Consortium at Fayetteville State University (Figure 20), which is funded by U.S. Department of Defense Grant W911NF-09-1-0011. Mineral compositions measured were collected using a beam current of 20 nA with an accelerating voltage of 15 kV and a beam size of 5 µm. Five

wavelength dispersive spectrometers (WDS) with ten diffracting crystals were used to measure the major oxides of Si, Ti, Al, Fe, Mn, Mg, Ca, Na, Cr, and K, with counting times of thirty seconds on the peak and fifteen seconds on the backgrounds. To ensure the accuracy of each analysis, appropriate natural and synthetic standards from the Astimex mineral block were used.

Data collection consisted of a single core-to-rim traverse with four to eight analysis points on each phenocryst. Two to four phenocrysts were analyzed per sample. Once EPMA data were collected, they were examined for any discrepancies or outliers between data points. For example, points that were unknowingly analyzed too close to the crystal edge or to a crack within the crystal would not give accurate weight percents or cation totals. Inconsistent data points of this type were not used in the final data analysis. Compositional changes from core to rim in each phenocryst were examined for differentiation trends and compared to trends seen in the whole-rock data. In addition, Mg# was calculated as a measure of differentiation in the magma chamber. Mg# can be calculated using different formulas based on the overall cation ratio of magnesium to iron within rocks or minerals. For this study, Mg# was calculated for each data point using the equation,

$$\text{Mg\#} = \frac{\text{Mg}}{(\text{Mg}+\text{Fe}^{\text{tot}})} * 100.$$

Figure 20. Electron microprobe at Fayetteville State University.

Geothermobarometry

Geothermobarometry follows methods outlined by Putirka (2008) and Wang et al. (2021) using cpx-only thermobarometers. Both models were calibrated using experimental hydrous systems for mafic lavas (Putirka, 2008; Wang et al., 2021). Cpx components are calculated on a six-oxygen basis with a cation sum of 4 ± 0.02. Al^{VI} and Fe^{2+} in equations were calculated from original cation data for atoms per formula unit (a.p.f.u.) using the Carleton College Mineral Formula Recalculation spreadsheet (Brady and Perkins, 2008). Use of the Putirka (2008) thermometer and barometer required the calculation of diopside + hedenbergite (DiHd) and enstatite + ferrosilite (EnFs) obtained using the same recalculation spreadsheet (Brady and Perkins, 2008).

The Putirka barometer used the following equation:

$$P(kbar) = 3205 + 0.384T(K) - 518\ln T(K) - 5.62(X_{Mg}^{cpx}) + 83.2(X_{Na}^{cpx}) + 68.2(X_{DiHd}^{cpx}) + 2.52\ln(X_{Al(VI)}^{cpx}) - 51.1(X_{DiHd}^{cpx})^2 + 34.8(X_{EnFs}^{cpx})^2$$

The Putirka thermometer uses the following equation:

$$T(K) = \frac{93100 + 544P(kbar)}{61.1 + 36.6(X_{Ti}^{cpx}) + 10.9(X_{Fe}^{cpx}) - 0.95(X_{Al}^{cpx} + X_{Cr}^{cpx} - X_{Na}^{cpx} - X_{K}^{cpx}) + 0.395[\ln(a_{En}^{cpx})]^2}$$

The barometer has a standard error of estimate (SEE) of ± 5 kbar, and the SEE for the thermometer is ± 50-60 °C. The term X_{Al}^{cpx} is used to represent total Al. Temperature is recorded in degrees Kelvin and is converted to degrees Celsius for ease of comparison with Wang et al. (2021).

The thermometer and barometer from Wang et al. (2021) use a nonlinear term (NLT) dependent on Al^{VI} in jadeite (Jd). Al^{VI} is pressure dependent during crystallization and is used to calculate the NLT in Wang et al. (2021). The Wang et al. barometer uses the following equation:

$$P(kbar) = a \times NLT \times \ln(Al^{VI}) + b\mathrm{Si} + c\mathrm{Fe}^{tot} + d\mathrm{Mg} + e\mathrm{Ca} + f\mathrm{Na} + g$$

The Wang et al. thermometer uses the following equation:

$$T(°C) = 100\,[a \times NLT + b\mathrm{Ti} + c\mathrm{Al} + d\mathrm{Mn} + e\mathrm{Mg} + f\mathrm{Ca} + g\mathrm{Fe}^{2+} + h\mathrm{H_2O(wt\%)} + i$$

The barometer has an SEE of ±1.66 kbar and the thermometer has an SEE equal to ±36.6 °C. The thermometer accounts for H_2O (wt%) in solving for temperature. However, because rocks used in this study have been altered, H_2O is neglected. Results from both geothermobarometric methods are compared as a check on their validity and to highlight any discrepancies such as negative pressures or extremely high temperatures.

III. **RESULTS**

Petrography

Petrographic analysis indicates that low-grade metamorphic and alteration products are abundant in every sample. Thin section descriptions of the samples are shown in Tables 2-6. Representative photomicrographs of phenocrysts are shown in Figures 21-23. Olivine phenocryst content ranges from 5-15%, forming 1-2 mm long typically euhedral crystals that are completely altered to hematite, serpentine, chlorite, and brucite. Some samples have minor secondary epidote and iddingsite. Cpx phenocryst content ranges from 5-20%, forming 1-3 mm long, euhedral crystals. Simple and polysynthetic twinning occurs in some crystals. The cpx shows alteration in centers of crystals and along some oscillatory zones, but the alteration products are too fine-grained to identify with certainty. Olivine and cpx sometimes form glomerocrysts. The groundmass in the samples consists of plagioclase microlites, cpx, and opaque microlites with textures ranging from intersertal to hyalopilitic. Some bomb and intrusive samples show pilotaxitic texture. Vesicles range from 15-30%, are 1-3 mm across, have round to elongate shapes and are filled with quartz, chalcedony, zeolites, calcite, prehnite and minor pumpellyite (see also Ohrmundt, 2020).

Plagioclase phenocrysts are only present in sill package samples KB43-16, PO7-16, and G56-16. Plagioclase content in these samples ranges from 20-25%, forming 2-5 mm long phenocrysts in PO7-16 and G56-16 and reaching up to 1 cm in length in KB43-16. The plagioclase is almost completely sericitized in anorthite-rich cores, which pass into albite-rich rims. Sill samples typically have coarser grained diabasic or subophitic texture.

Igneous disequilibrium textures characteristic of intermediate volcanic rocks are common. Oscillatory zoning in cpx can be seen in SEM imagery (Figure 24) and under the petrographic microscope, indicating changes in magma chamber composition or disequilibrium effects during crystal growth. Plagioclase phenocrysts in KB43-16, PO7-16, and G56-16 also show sieve texture in anorthite-rich cores, representing an influx of hotter magma in the chamber causing dissolution of plagioclase. Other textures in thin section include reaction rims of cpx on olivine in hypabyssal intrusions and bomb samples.

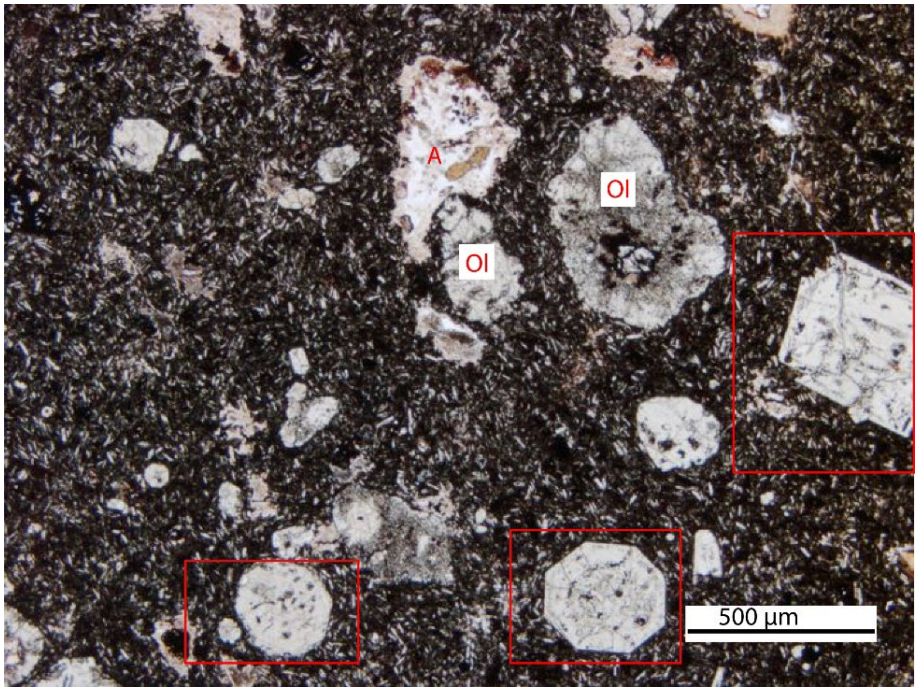

Figure 21. Pyroclastic bomb sample SO-1747A with rectangles outlining cpx phenocrysts. Groundmass shows intersertal texture. A: amygdule; Ol: olivine.

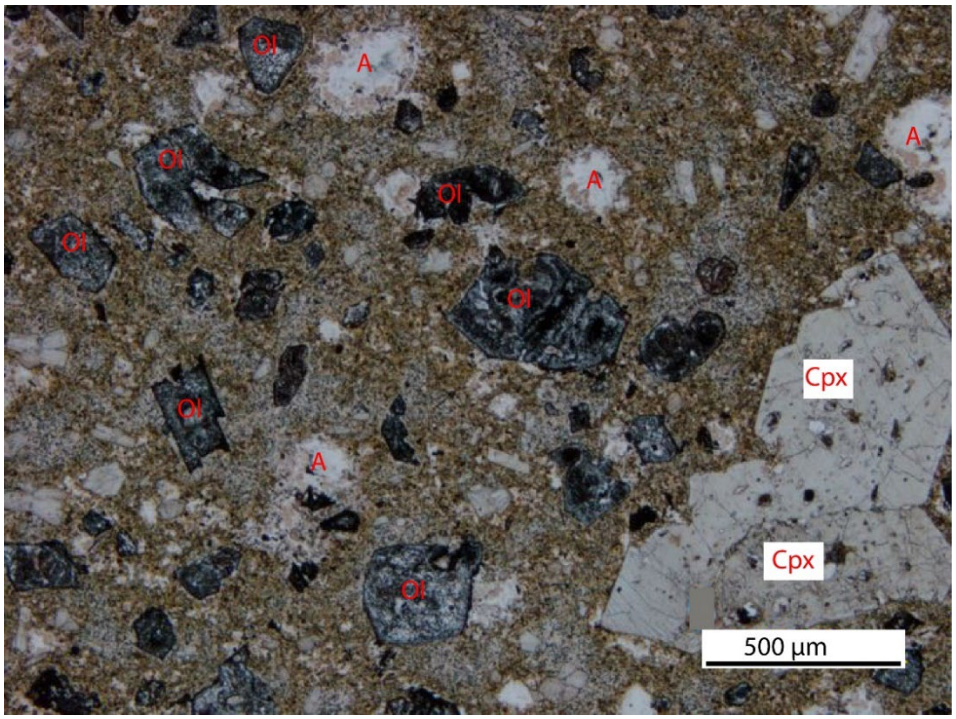

Figure 22. Pyroclastic bomb sample SO-18176 B, showing olivine (Ol) almost completely altered to hematite, serpentine, and chalcedony, with unaltered cpx phenocrysts. A: amygdules.

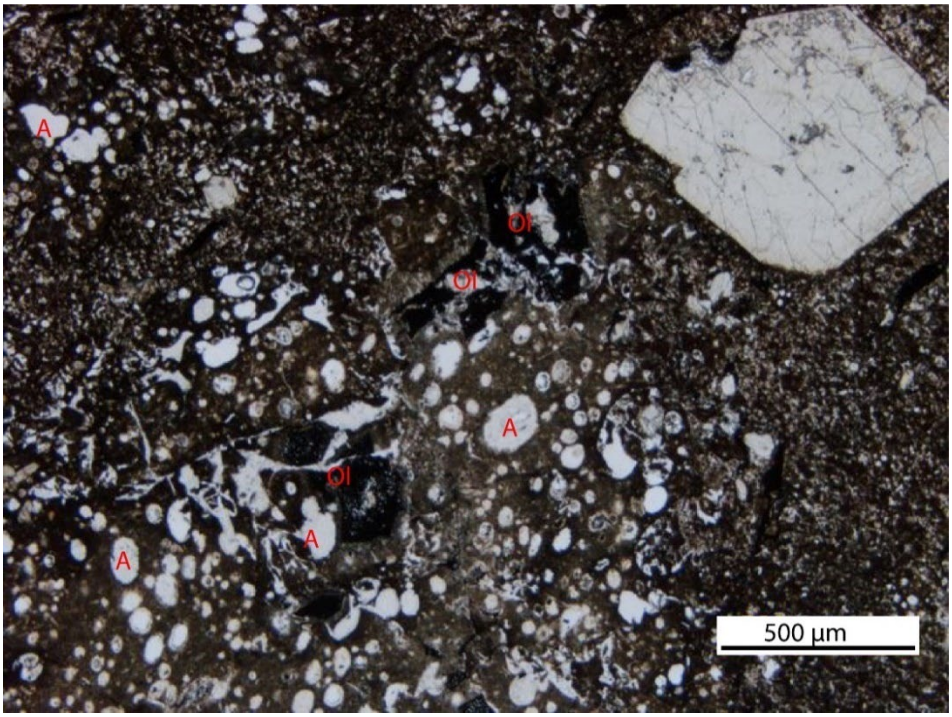

Figure 23. Agglutinate sample SO-1767 C, showing round to elongate amygdules (A), olivine (Ol) completely altered to hematite, and cpx in the upper right corner with some alteration visible.

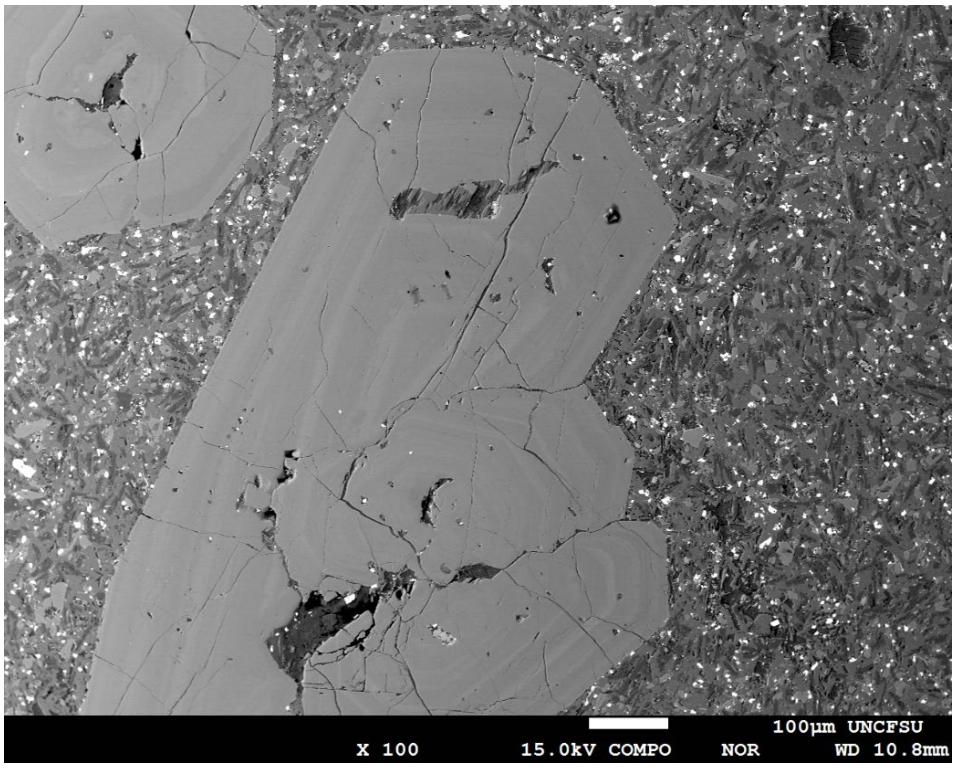

Figure 24. Hypabyssal intrusion sample SO-1894 showing cpx phenocrysts with excellent oscillatory zoning. The larger crystal in the center is a glomerocryst. White scale bar (100 µm) is shown at the bottom of the image.

Table 2. Thin section description of sill samples

Sample	Location	Vesicle Characteristics	Groundmass	Olivine	Cpx
KB43-16 (Also contains plagioclase phenocrysts discussed in text)	Sill Package 1- Andrews field area	No vesicles in sample.	Intersertal	10%; 0.25-1 mm; altered to hematite, serpentine, chlorite	10%; 1-3 mm
PO7-16 (Also contains plagioclase phenocrysts discussed in text)	Sill Package 2- Andrews field area	No vesicles in sample.	Intersertal	15%; 0.5-1 mm; altered to hematite, chlorite, serpentine, minor epidote and iddingsite	15%; 1-2 mm
G56-16 (Also contains plagioclase phenocrysts discussed in text)	Sill Package 3- Andrews field area	No vesicles in sample.	Intersertal	5%; 0.25-0.5 mm; altered to hematite, serpentine, and chlorite	10%; 1-2 mm
M6-4	Ohrmundt field area	10%; 1-2mm, elongate and irregular; filled with calcite, zeolites, prehnite	Intersertal to pilotaxitic	10%; 1-2 mm; altered to hematite, serpentine, secondary quartz	15%; 1-2 mm

Table 3. Thin section description of spatter and agglutinuate samples

Sample	Location	Groundmass	Vesicle Characteristics	Olivine	Cpx
VA1603	Andrews field area	Intersertal to hyalopilitic-hematite alteration and sericitization of plagioclase	40%; 0.5-1 mm; round to elongate, filled with quartz, chalcedony, chlorite, zeolites, and prehnite	5%; 0.5-1 mm; altered to hematite	5%; 0.5-1 mm
SO-18126 A	Ohrmundt field area	Hyalopilitic	30%; 0.5-2 mm; irregular, filled with quartz, chalcedony, chlorite, zeolites, prehnite, calcite, minor epidote	5%; 0.5-1 mm; altered to hematite, serpentine, and some quartz	10%; 1-2 mm
SO-1767 C	Ohrmundt field area	Intersertal to hyalopilitic	40%; 1-2 mm; round to elongate, filled with quartz, chalcedony, chlorite, zeolites, calcite, prehnite	10%; 0.5-1 mm; altered to hematite and serpentine	15%; 0.5-2 mm
M1-1A	Ohrmundt field area	Intersertal to hyalopilitic	15%; 1-2 mm, round to irregular; filled with quartz, chalcedony, chlorite, prehnite, zeolites, minor epidote	15%; 1-2 mm; altered to hematite, serpentine, and quartz	15%; 1-2 mm

Table 4. Thin section description of other hypabyssal intrusions

Sample	Location	Groundmass	Vesicle Characteristics	Olivine	Cpx
VA 16105	Andrews field area	Hyalopilitic to pilotaxititic	10%; 1-2 mm; irregular; filled with quartz, titanite, chlorite, serpentine, calcite, zeolites, minor smectite	15%; 1-2 mm; altered to hematite, chlorite, serpentine	10%; 1-2 mm
SO-1716 D	Ohrmundt field area	Hyalopilitic to intersertal	30%; 1-6 mm, irregular; filled with quartz, chalcedony, calcite, chlorite, zeolites, prehnite	10%; 0.25-1 mm; altered to hematite, serpentine, quartz	10%; 0.5-3 mm
SO-1763 G	Ohrmundt field area	Hyalopilitic to intersertal	30%; 1-6 mm, irregular; filled with quartz, chalcedony, calcite, chlorite, zeolites, prehnite	10%; 0.25-1 mm; altered to hematite, serpentine, quartz	10%; 0.5-2 mm
M3-4	Ohrmundt field area	Intersertal	10%; 1-2 mm, round; filled with quartz, chalcedony, chlorite, zeolites, prehnite	15%; 0.25-1 mm; altered to hematite, serpentine, epidote, quartz	20%; 0.5-1 mm
SO-1888 A	Ohrmundt field area	Pilotaxitic	15%; 1-2 mm, elongate and irregular; filled with quartz, chalcedony, chlorite, calcite, zeolites, and prehnite	10%; 0.25-1 mm; altered to hematite, serpentine, quartz	15%; 0.25-2 mm
SO-1894	Ohrmundt field area	Hyalopilitic to intersertal	10%; 1-2 mm, round; filled with quartz, chalcedony, chlorite, zeolites, prehnite	15%; 0.25-1 mm; altered to hematite, serpentine, epidote, quartz	20%; 1-3 mm
SO-18166	Ohrmundt field area	Hyalopilitic to pilotaxitic	10%; 1-2 mm, round; filled with quartz, chalcedony, chlorite, zeolites, prehnite	15%; 0.25-1 mm; altered to hematite, serpentine, epidote, quartz	20%; 0.5-1 mm

Table 5. Thin section description of pyroclastic bomb samples

Sample	Location	Groundmass	Vesicle Characteristics	Olivine	Cpx
MS6-7	Andrews field area	Hyalopilitic	30%; 1-2 mm, round; filled with quartz, chalcedony, calcite, zeolites, prehnite	5% 0.5-1 mm; altered to hematite, serpentine	5%; 0.25-1 mm
M1-4B	Ohrmundt field area	Hyalopilitic	30%; 0.25-3 mm, elongate; filled with chlorite, calcite, zeolites	5%; 0.25-1 mm; altered to hematite, serpentine	15%; 0.25-0.5 mm
M2-1A	Ohrmundt field area	Hyalopilitic	25%; 0.5-1 mm, irregular; filled with quartz, zeolites, calcite, epidote, prehnite and pumpellyite	10%; 1-2 mm; altered to hematite, serpentine, quartz	10%; 1-3 mm
M3-3	Ohrmundt field area	Hyalopilitic	25%; 0.5-1 mm, irregular; filled with quartz, zeolites, calcite, epidote, prehnite and pumpellyite	10%; 1-2 mm; altered to hematite, serpentine, quartz	10%; 1-2 mm
SO-18173	Ohrmundt field area-bomb in a diatreme	Hyalopilitic	25%; 0.5-1 mm, irregular; filled with quartz, zeolites, calcite, epidote, prehnite and pumpellyite	10%; 1-2 mm; altered to hematite, serpentine, quartz	10%; 1-2 mm
SO-18176 B	Ohrmundt field area-intrusive pyro. rock	Hyalopilitic	15%; 0.5-1 mm, irregular; filled with quartz, chalcedony, zeolites, hematite, calcite, prehnite	15%; 1-2 mm; altered to hematite, serpentine, chalcedony	10%; 1-2 mm
SO-1747 A	Ohrmundt field area	Intersertal	10%; 0.5 mm, irregular; filled with quartz, zeolites, epidote, chlorite, prehnite and pumpellyite	5%; 0.25-2 mm; altered to hematite, quartz, some brucite	10%; 0.5-2 mm

Table 6. Thin section description of bedded lapillistone sample

Sample	Location	Groundma	Vesicle Characteristics	Olivine	Cpx
1601.2A	Andrews field area	Hyalopilitic	20%; 0.25-0.5 mm, round; filled with quartz, chalcedony, zeolites, calcite, and prehnite	5% 0.5-1 mm; altered to hematite, serpentine	15%; 0.25-1 mm

Cpx Chemistry

Complete data for cpx analyses are shown in Appendices I and II and are plotted on the pyroxene quadrilateral from Morimoto (1988) in Figures 25-30. Data from Ohrmundt's field area are tightly clustered in the diopside and augite field. Diopside is generally more abundant in these samples. Data from Andrews' field area are also tightly clustered in the diopside and augite field (Figure 25). However, cpx from sill packages 1, 2, and 3 generally shows more abundant augite, including some subcalcic augite in sample KB43-16 (Figure 26).

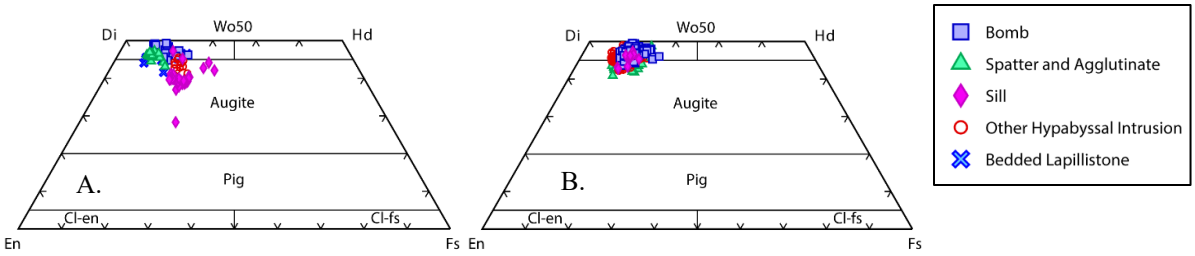

Figure 25. All data points for cpx analyzed in this study. Left quadrilateral (A) shows data for Andrews' samples and right quadrilateral (B) is for Ohrmundt's samples. En: enstatite; Cl-en: clinoenstatite; Fs: ferrosilite; Cl-fs: clinoferrosilite; Pig: pigeonite; Di: diopside; Wo: Wollastonite; Hd: hedenbergite.

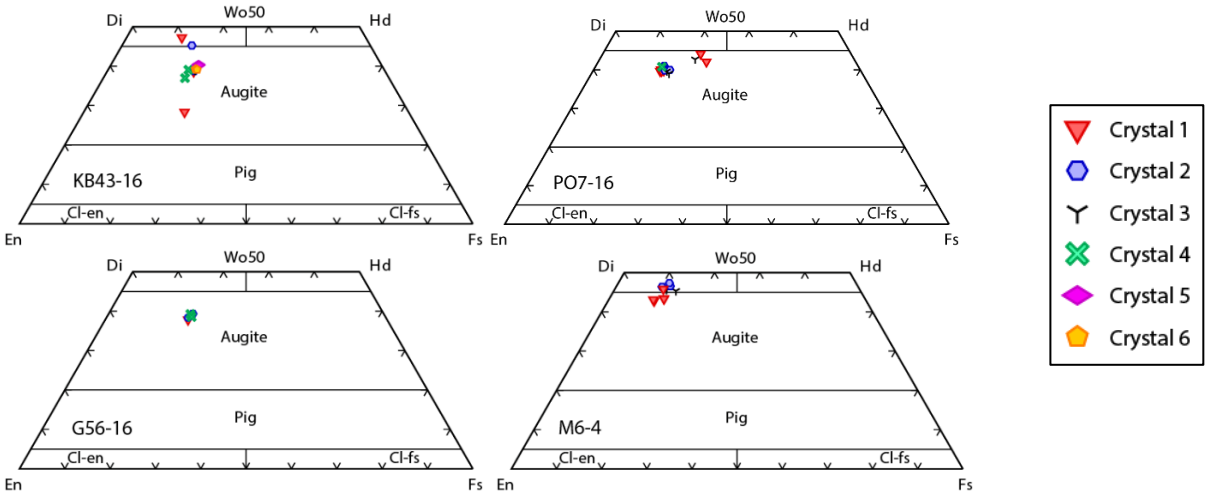

Figure 26. Cpx compositions for sills. Symbols indicate sites probed on individual cpx crystals. See Figure 25 for explanation of abbreviations.

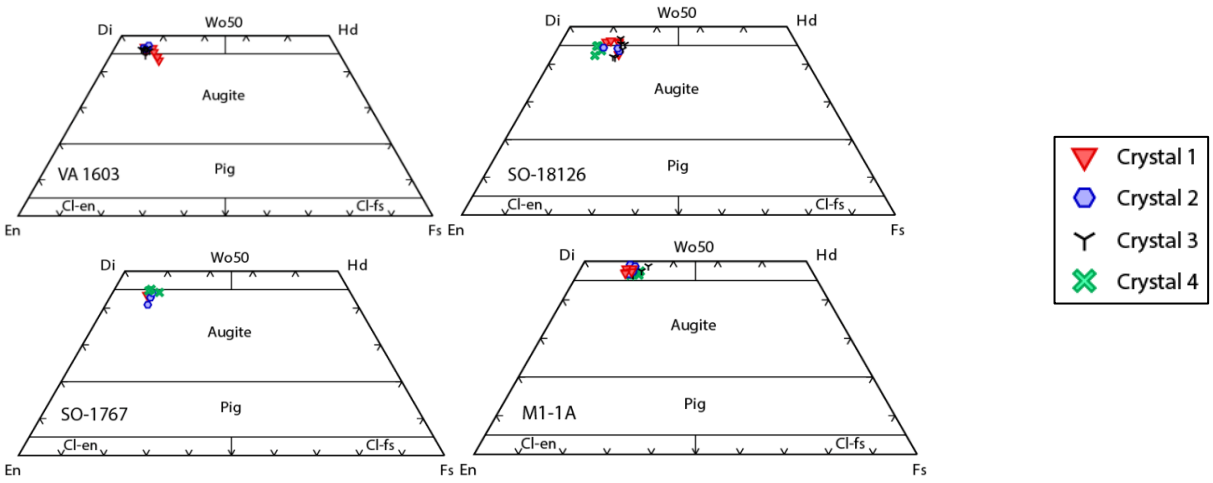

Figure 27. Cpx compositions for spatter and agglutinate. Symbols indicate sites probed on individual cpx crystals. See Figure 25 for explanation of abbreviations.

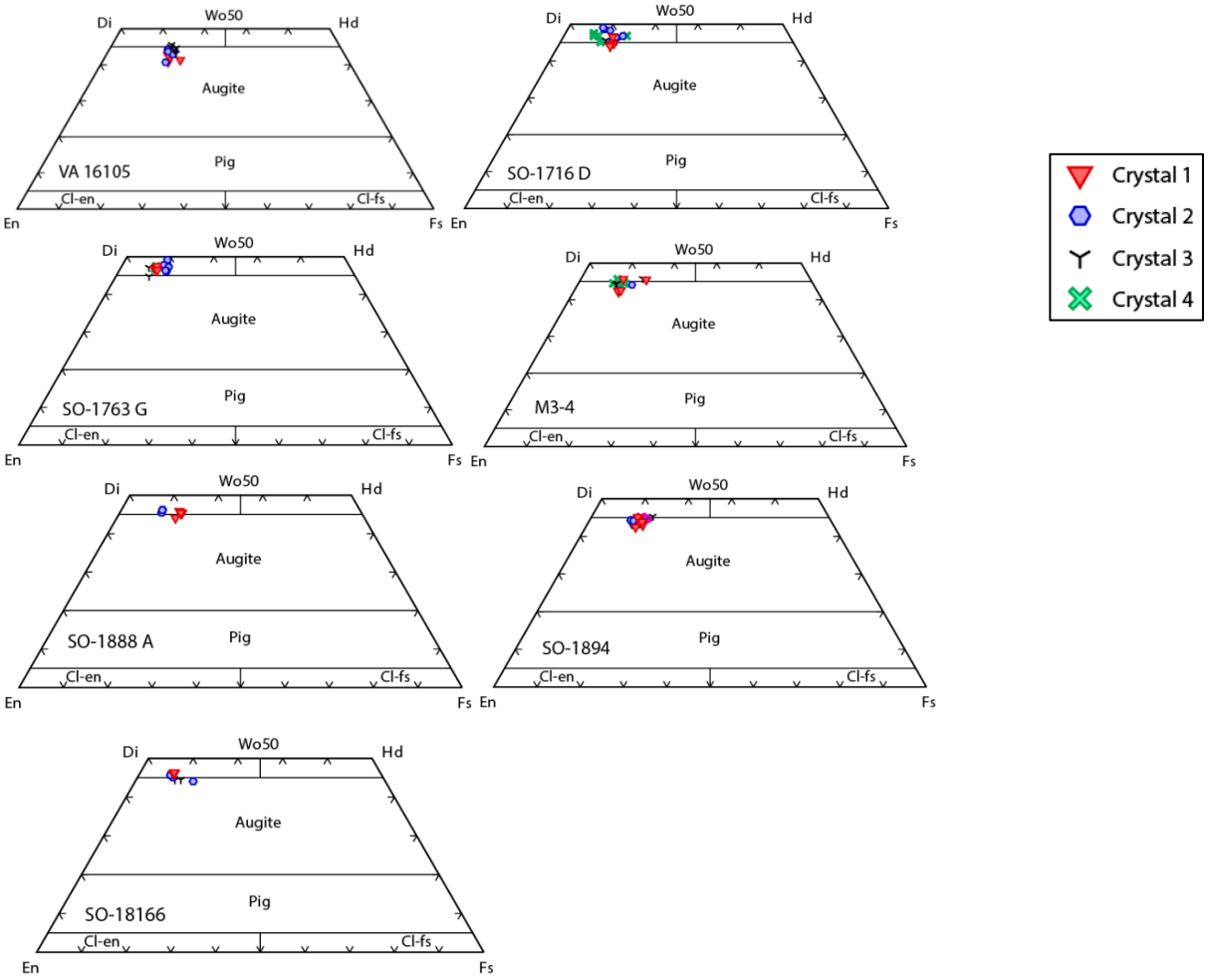

Figure 28. Cpx compositions for other hypabyssal intrusions. Symbols indicate sites probed on individual cpx crystals. See Figure 25 for explanation of abbreviations.

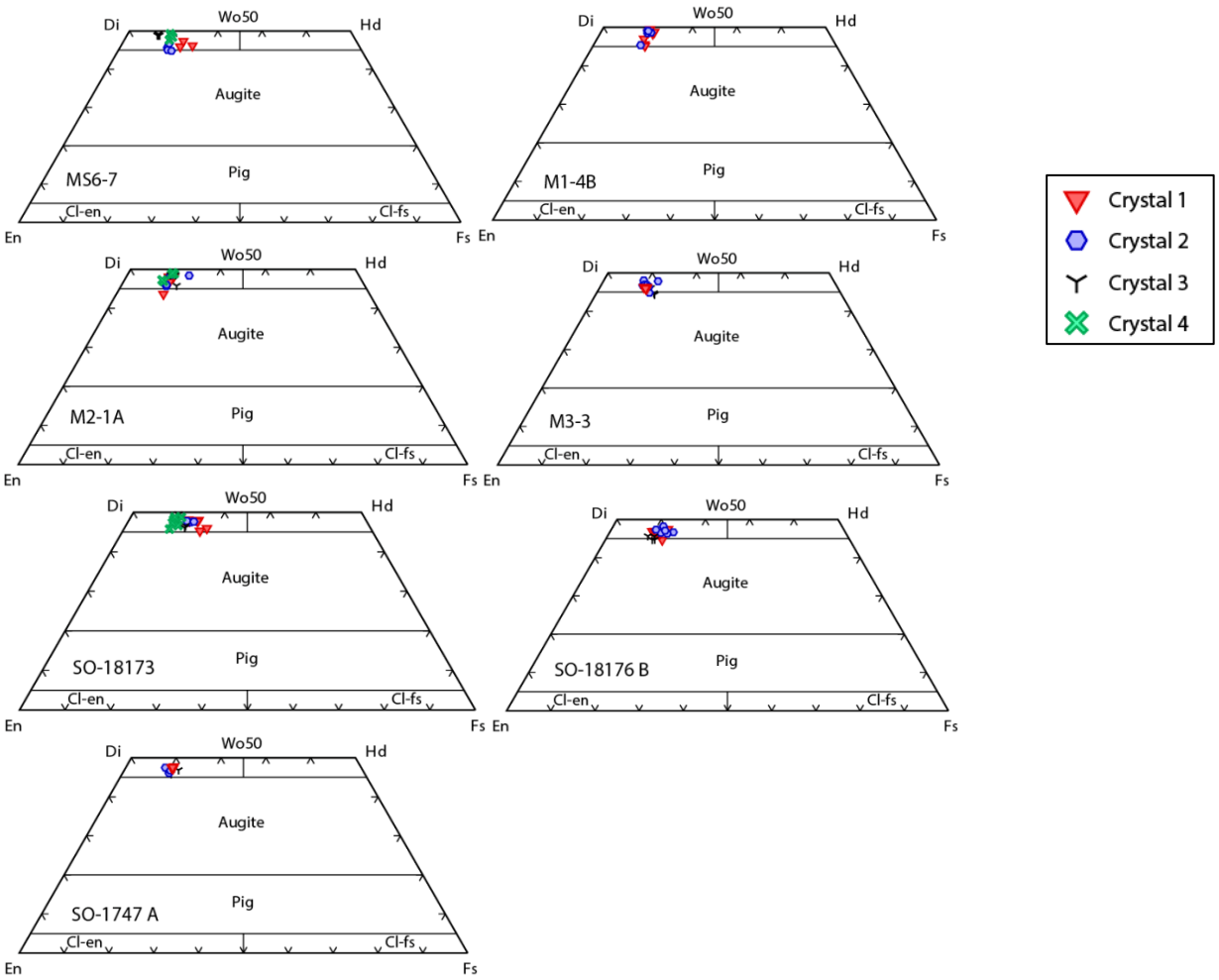

Figure 29. Cpx compositions for pyroclastic bombs. Symbols indicate sites probed on individual cpx crystals. See Figure 25 for explanation of abbreviations.

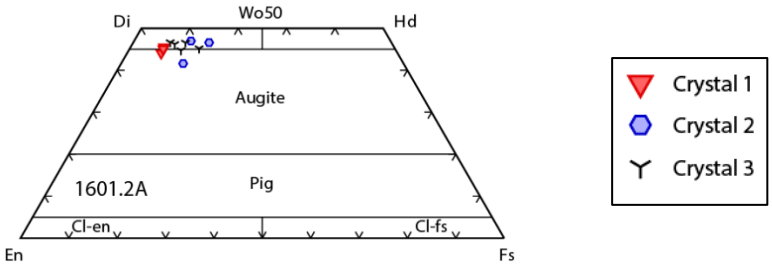

Figure 30. Cpx compositions for bedded lapillistone from Andrews' area. Symbols indicate sites probed on individual cpx crystals. See Figure 25 for explanation of abbreviations.

Variations in average values for major oxides FeO, MnO, MgO, TiO_2, Al_2O_3, CaO, Na_2O, and Cr_2O_3 as well as for Mg# are shown in Table 7 and Figures 31-36. All samples show

a strong trend of decreasing FeO with increasing Mg# (Figure 31), while most samples show a weaker trend of decreasing FeO with increasing MgO (Figure 32). Generally, samples show increasing FeO with decreasing MnO (Figure 33). All three of these trends are typical fractionation trends in cpx (Deer et al., 2013). In contrast, Cr_2O_3 increases with Mg# (Figure 34) which is expected because Cr is compatible in cpx (Deer et al., 2013).

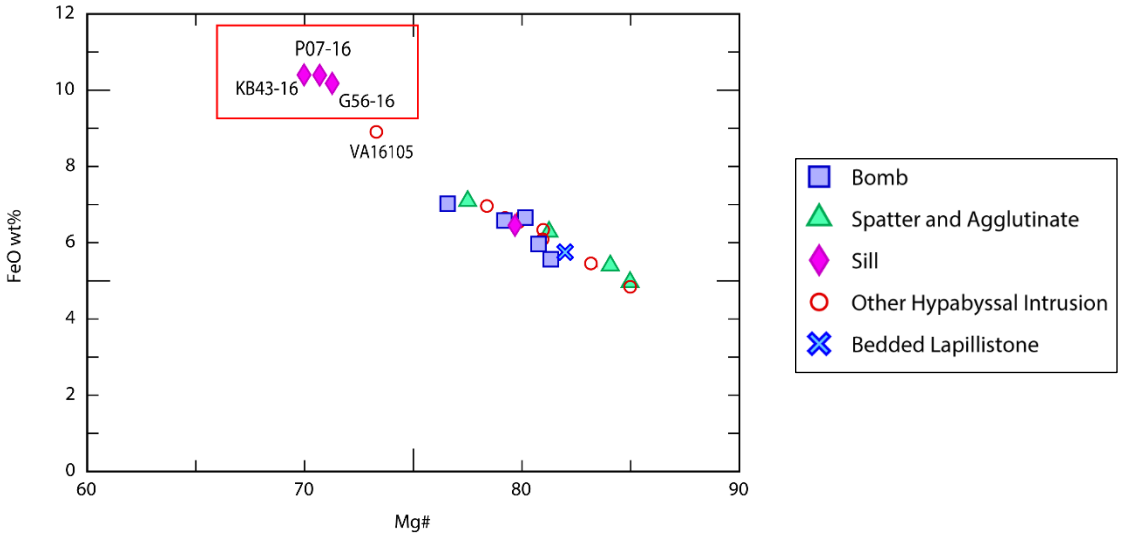

Figure 31. Average Mg# vs. FeO wt% for individual crystals. Red box indicates samples from sill packages.

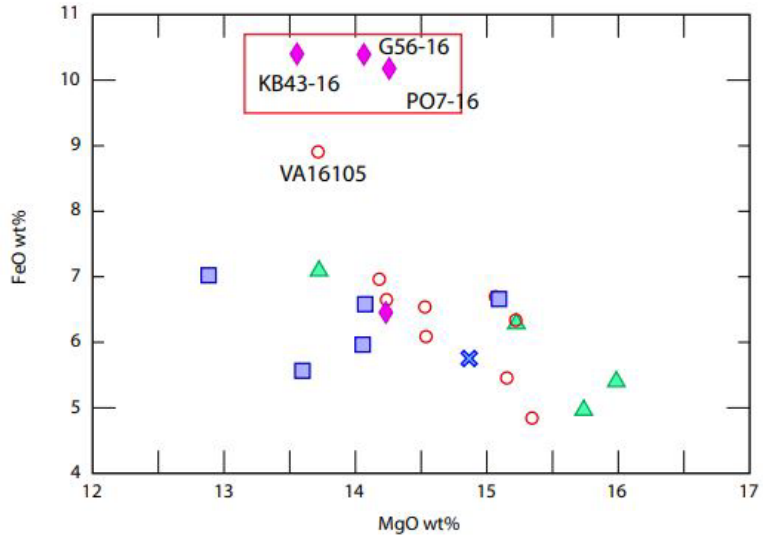

Figure 32. Average FeO vs. MgO wt% for individual crystals. Red box indicates sill packages. See Figure 31 for legend.

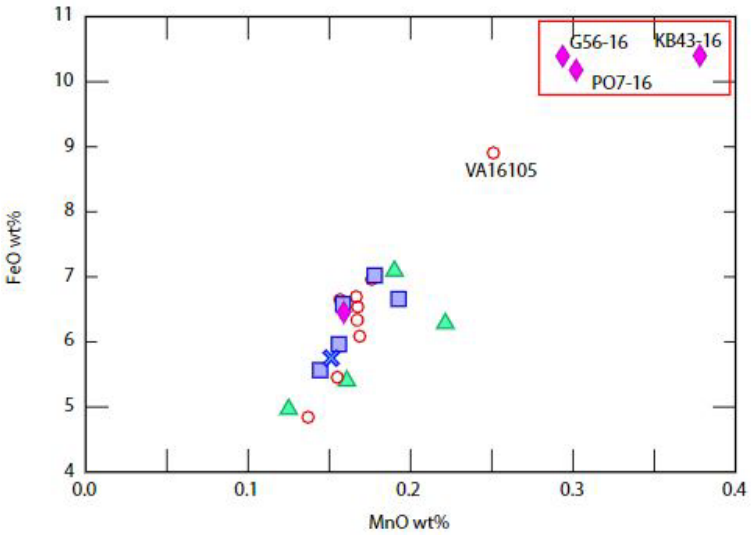

Figure 33. Average FeO vs. MnO wt% for individual crystals. Red box indicates samples from sill packages. See Figure 31 for legend.

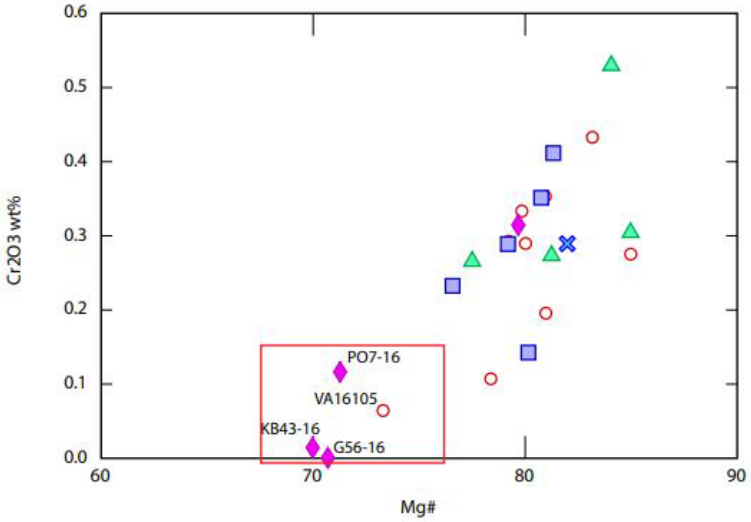

Figure 34. Average Mg# vs. Cr_2O_3 wt% for individual crystals. Red box indicates sill packages and one other hypabyssal intrusion. See Figure 31 for legend.

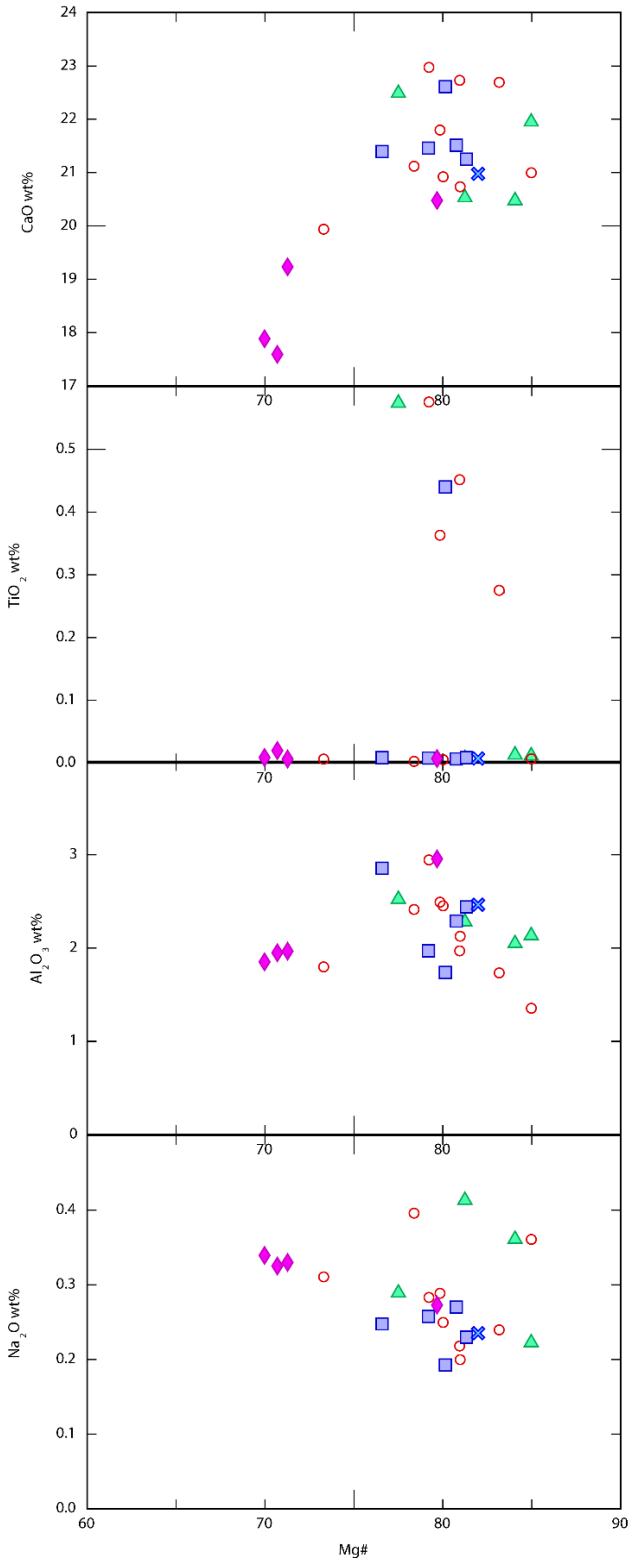

Figure 35. Diagram showing variations between CaO, TiO_2, Al_2O_3, Na_2O and contents vs. Mg# for individual crystals. See Figure 31 for legend.

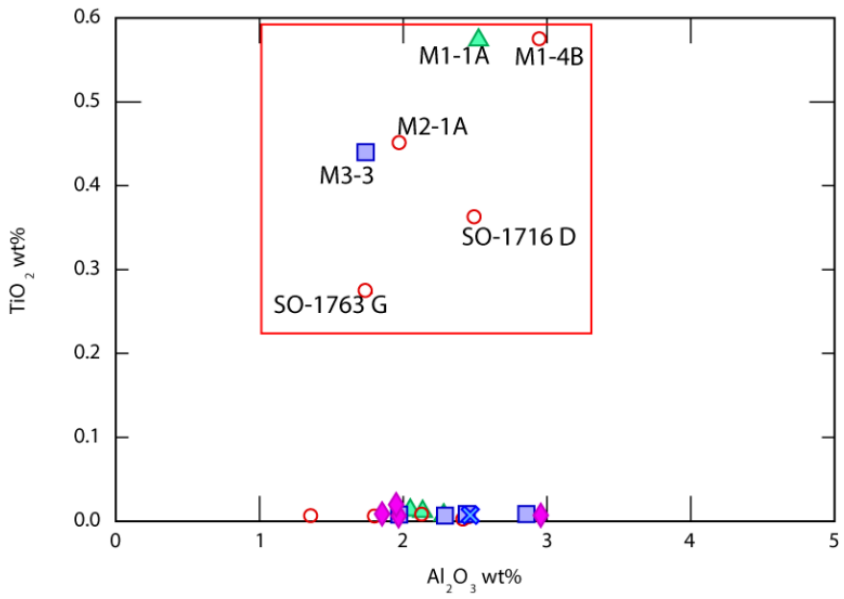

Figure 36. Average Al_2O_3 vs. TiO_2 wt%. Red box indicates samples enriched in TiO_2.

In Figure 35, all samples show scattered data for CaO and Na_2O when plotted against Mg#. Most of the data for Al_2O_3 show a slight increase when plotted against Mg#. Six samples show unusually high TiO_2 values, although, these same samples show a decreasing trend with increasing Mg#. When these five samples are plotted against Al_2O_3, the data for TiO_2 are scattered (Figure 36).

Cpx phenocrysts in sill packages 1-3 in Andrews' study area (PO7-16, G56-16, and KB43-16) area show unusual trends as compared to the rest of the samples, with higher total FeO and MnO, low Cr_2O_3, and low Mg# (Figures 31, 33, and 34). Sample VA 16105, a hypabyssal intrusion discussed previously in Chapter 1, also tends to plot away from the main trend and closer to the sill package samples.

Table 7. Average cpx wt% of major oxides in each sample. FeO* indicates total Fe is reported as FeO

	SO-18126 A	SO-1767 C	M1-1A	SO-1716 D	SO-1763 G	M3-4	SO-1888A
SiO_2	51.47	51.28	50.85	51.07	52.20	50.87	51.29
TiO_2	0.01	0.01	0.57	0.36	0.28	0.01	0.00
Al_2O_3	2.28	2.05	2.52	2.49	1.73	2.13	2.41
FeO*	6.28	5.40	7.09	6.54	5.46	6.34	6.96
MnO	0.22	0.16	0.19	0.17	0.16	0.17	0.18
MgO	15.22	15.99	13.72	14.53	15.15	15.22	14.18
CaO	20.53	20.47	22.49	21.8	22.69	20.73	21.12
Na_2O	0.41	0.36	0.29	0.29	0.24	0.20	0.40
K_2O	0.03	0.01	0.00	0.01	0.00	0.02	0.00
Cr_2O_3	0.12	0.53	0.27	0.33	0.43	0.20	0.11
Total wt%	96.16	96.27	97.99	97.58	98.34	95.88	96.65

	M3-3	SO-18173	SO-18176 B	SO-1747A	M6-4	PO7-16	G56-16	KB43-16
SiO_2	52.31	50.53	49.85	51.13	48.87	50.78	51.33	50.40
TiO_2	0.44	0.01	0.01	0.01	0.01	0.01	0.02	0.01
Al_2O_3	1.74	2.86	1.97	2.29	2.96	2.15	1.95	1.85
FeO*	6.66	7.02	6.58	5.96	6.45	8.82	10.39	10.40
MnO	0.19	0.18	0.16	0.16	0.16	0.26	0.29	0.38
MgO	15.09	12.88	14.07	14.06	14.23	15.05	14.06	13.56
CaO	22.61	21.39	21.46	21.51	20.48	19.29	17.59	17.88
Na_2O	0.19	0.25	0.26	0.27	0.27	0.33	0.33	0.34
K_2O	0.01	0.00	0.01	0.01	0.03	0.00	0.00	0.05
Cr_2O_3	0.14	0.23	0.29	0.35	0.31	0.12	0.00	0.01
Total wt%	99.39	95.35	94.65	95.74	93.77	97.19	95.97	94.53

	SO-1894	SO-18166	M1-4B	M2-1A	VA1603	VA16105	MS6-7	1601.2A
SiO_2	50.76	51.19	50.75	51.23	51.85	50.60	51.60	51.12
TiO_2	0.01	0.01	0.58	0.45	0.01	0.01	0.01	0.01
Al_2O_3	2.45	1.35	2.94	1.97	2.13	1.80	2.44	2.46
FeO*	6.70	4.84	6.65	6.09	4.96	8.91	5.57	5.75
MnO	0.17	0.14	0.16	0.17	0.12	0.25	0.14	0.15
MgO	15.07	15.34	14.24	14.54	15.74	13.72	13.60	14.87
CaO	20.92	21.00	22.97	22.73	21.95	19.94	21.25	20.98
Na_2O	0.25	0.36	0.28	0.22	0.22	0.31	0.23	0.24
K_2O	0.01	0.01	0.01	0.01	0.00	0.01	0.02	0.00
Cr_2O_3	0.29	0.28	0.29	0.35	0.30	0.06	0.41	0.29
Total wt%	96.62	94.51	98.87	97.76	97.30	95.60	95.27	95.86

Cpx discrimination diagrams for basalts and basaltic andesites from Leterrier et al. (1982) are shown in Figures 37 and 38. These are calculated using atoms per formula unit (a.p.f.u). Most samples plot as calc-alkaline to tholeiitic basalts except for the five that are enriched in Ti (Figure 37). The reason for the Ti enrichment remains unclear and was previously noted in the same samples in Figure 35. All samples, however, plot in the field for orogenic basalts consistent

with a volcanic arc setting (Figure 38). This result is also consistent with the fact that all the samples plot in calc-alkaline fields using whole-rock discrimination diagrams (Figures 17 and 18).

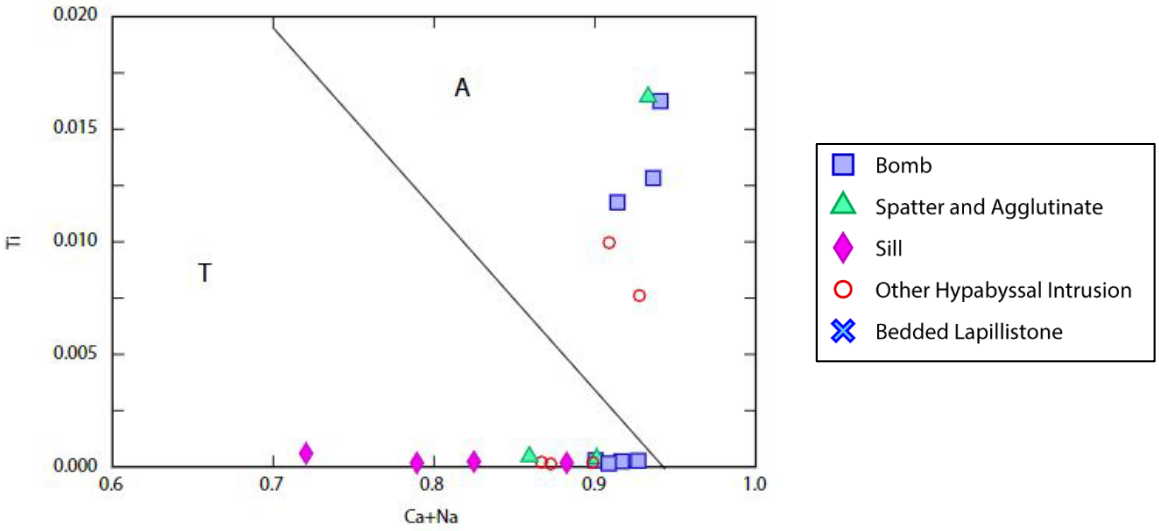

Figure 37. Ca+Na vs. Ti discrimination plot from Leterrier et al. (1982) measured in a.p.f.u. Field T represents orogenic basalts and non-orogenic tholeiites. Field A represents alkaline basalt compositions.

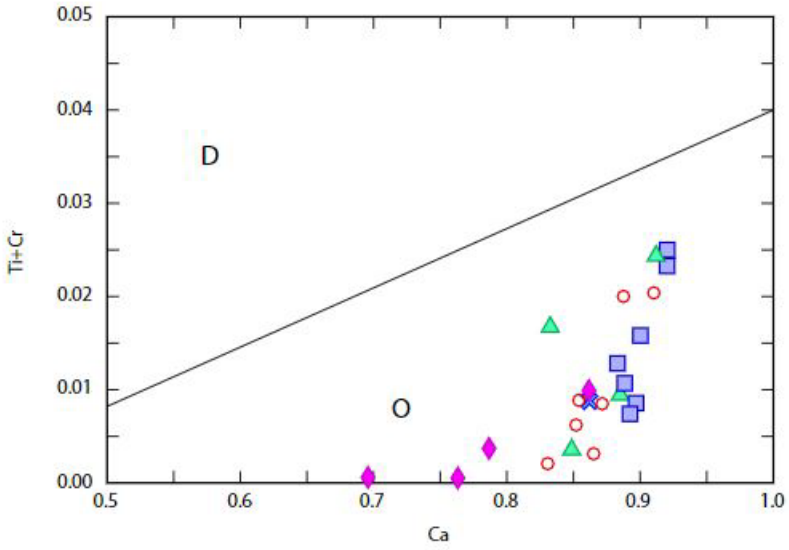

Figure 38. Ca vs. Ti+Cr discrimination plot from Leterrier et al. (1982). Cations measured in a.p.f.u. Field D represents non-orogenic tholeiites. Field O represents orogenic basalts characteristic of volcanic arc settings. See Figure 37 for legend.

Geothermobarometry

Geothermobarometric results using the Putirka (2008) and Wang et al. (2021) calibrations resulted in a wide range of temperatures and pressures. Pressure and temperature values for all cpx samples are shown in Appendix III and the average values for each sample are shown in Table 8. It is important to note that both thermobarometers only use compositions of cpx (rather than cpx plus liquid, for example) and are calibrated using experimental data. Both thermobarometers are used in this study as a check on the validity of the pressure and temperature results. Average temperature values range from ~1150-1300 °C and are consistent for both calibrations. However, the calculated pressures do not correlate closely between the two techniques. Also, both barometers yield negative pressures for some pyroclastic bomb and intrusion samples (Appendix III). Omitting the negative values, average pressure values range from ~0-10 kbar for the Wang et al. (2021) barometer and ~1.6-9 kbar for the Putirka (2008) barometer.

Results for the Wang et al. (2021) calibrations for all samples are shown in Figures 39-43 (omitting the negative pressure values). Crustal depth is shown on the right side of the figures and was calculated using an approximate increase of pressure of 0.3kbar/km. Overall, Wang et al. (2021) calibrations give lower temperatures consistent with basaltic andesites and fewer negative pressures, while also having a lower SEE for the thermobarometer than the calibration of Putirka (2008). For these reasons, results from the Wang et al. (2021) thermobarometer are preferred here.

Table 8. Average temperature and pressure values for each sample

Sample	Rock Type	Temperature (°C) Wang et al. (2021)	Temperature (°C) Putirka (2008)	Pressure (kbar) Wang et al. (2021)	Pressure (kbar) Putirka (2008)
KB43-16	Sill from sill package 1	1160 ± 35	1192 ± 35	4.19 ± 3.8	7.45 ± 2.2
PO7-16	Sill from sill package 2	1234 ± 65	1244 ± 49	9.63 ± 4.1	4.09 ± 1.7
G56-16	Sill from sill package 3	1214 ± 49	1208 ± 25	5.82 ± 2.5	9.25 ± 1.5
M6-4	Sill	1195 ± 12	1225 ± 10	3.91 ± 0.7	4.48 ± 1.0
VA 1603	Spatter and agglutinate	1217 ± 18	1241 ± 12	4.11 ± 1.3	1.64 ± 1.7
SO-18126 A	Spatter and agglutinate	1198 ± 34	1226 ± 27	4.67 ± 2.0	5.40 ± 1.2
SO-1767 C	Spatter and agglutinate	1218 ± 21	1244 ± 18	4.94 ± 2.0	3.27 ± 1.2
M1-1A	Spatter and agglutinate	1151 ± 12	1180 ± 10	0.85 ± 0.9	5.36 ± 1.5
VA 16105	Hypabyssal intrusion	1164 ± 13	1197 ± 8	3.24 ± 0.7	5.91 ± 0.8
SO-1716 D	Hypabyssal intrusion	1164 ± 26	1196 ± 15	1.50 ± 1.6	4.01 ± 2.7
SO-1763 G	Hypabyssal intrusion	1178 ± 26	1204 ± 19	1.12 ± 1.6	2.33 ± 1.3
M3-4	Hypabyssal intrusion	1195 ± 18	1220 ± 10	3.18 ± 0.7	3.30 ± 1.8
SO-1888 A	Hypabyssal intrusion	1209 ± 20	1235 ± 11	5.54 ± 0.7	4.70 ± 1.9
SO-1894	Hypabyssal intrusion	1185 ± 15	1214 ± 12	2.76 ± 1.4	3.78 ± 1.2
SO-18166	Hypabyssal intrusion	1242 ± 29	1256 ± 19	5.98 ± 1.3	1.95 ± 1.1
MS6-7	Pyroclastic bomb	1294 ± 44	1252 ± 16	6.19 ± 0.6	5.06 ± 1.8
M1-4B	Pyroclastic bomb	1152 ± 8.5	1178 ± 7.6	0.13 ± 0.7	5.08 ± 1.0
M2-1A	Pyroclastic bomb	1171 ± 34	1185 ± 13	0.14 ± 1.3	3.66 ± 1.9
M3-3	Pyroclastic bomb	1172 ± 28	1225 ± 15	0.32 ± 1.3	2.19 ± 1.6
SO-18173	Pyroclastic bomb	1225 ± 44	1226 ± 14	4.69 ± 0.6	5.51 ± 1.6
SO-18176 B	Pyroclastic bomb	1170 ± 17	1203 ± 11	1.68 ± 0.9	3.01 ± 1.3
SO-1747 A	Pyroclastic bomb	1232 ± 10	1235 ± 6	4.95 ± 0.7	3.87 ± 1.0
1601.2A	Bedded lapillistone	1233 ± 40	1226 ± 25	4.77 ± 2.2	4.00 ± 3.4

Sills typically give the largest pressure and temperature range compared to the other rock types. Cpx in samples from sill packages 1, 2, and 3 yields crystallization temperatures of 1086-1283 °C (Figure 39). The same samples yield a pressure range of 0.13-13.99 kbar (Figure 39). Cpx from spatter and agglutinate, other hypabyssal intrusions, pyroclastic bombs, and bedded lapillistone yields a temperature range of 1123-1349 °C, but pressures range from 0-9.2 kbar (Figures 40-43). Some data points from cpx in hypabyssal intrusions and bomb samples with higher TiO_2 yielded negative pressures due to a lower Al^{VI} content. These data points were omitted from Figures 41 and 42.

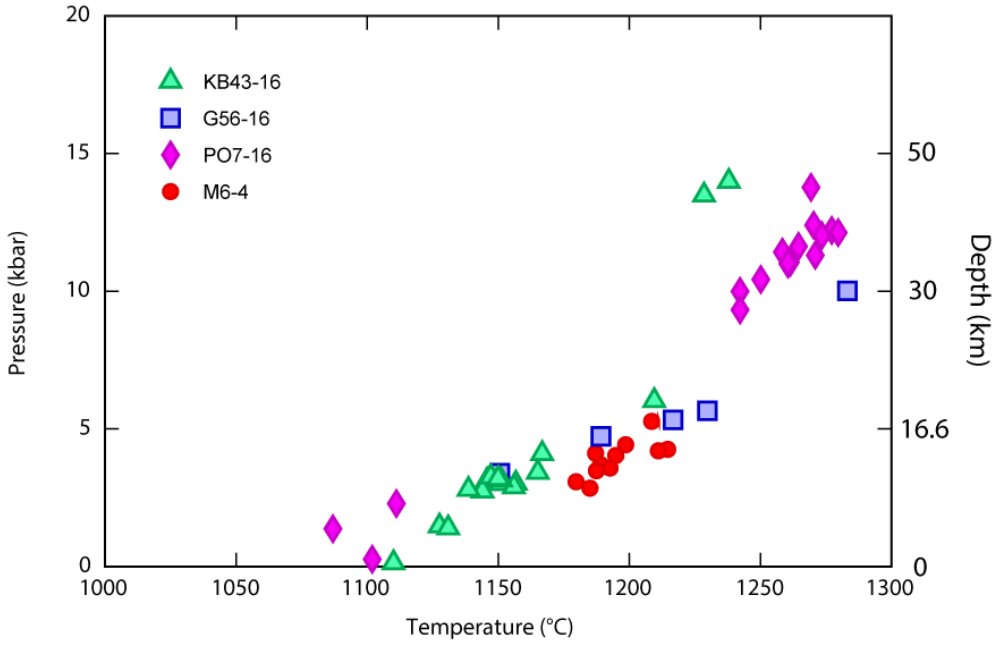

Figure 39. Temperature and pressure results for sills using the Wang et al. (2021) thermobarometer.

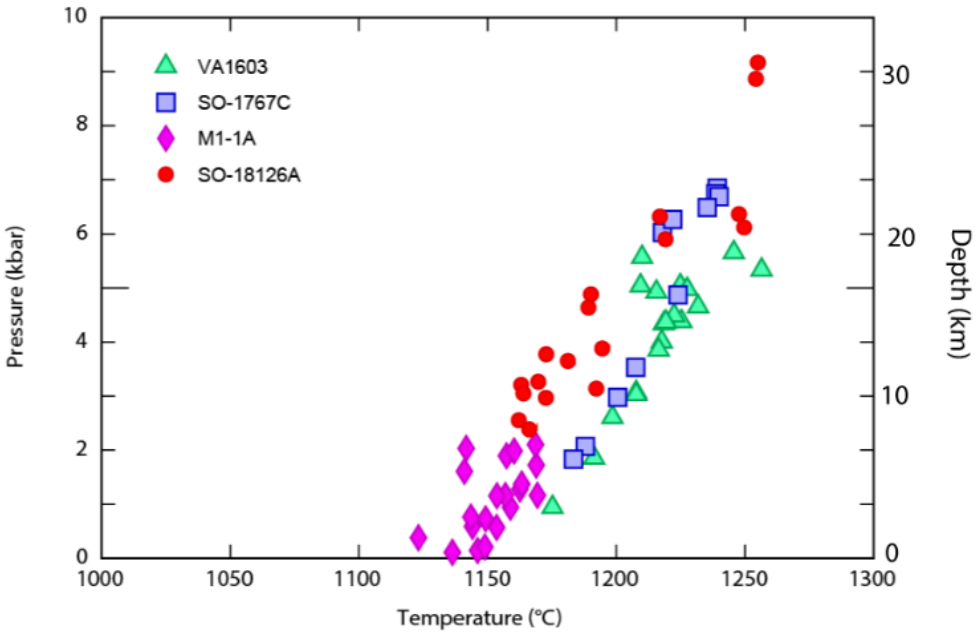

Figure 40. Temperature and pressure results for spatter and agglutinate using the Wang et al. (2021) thermobarometer.

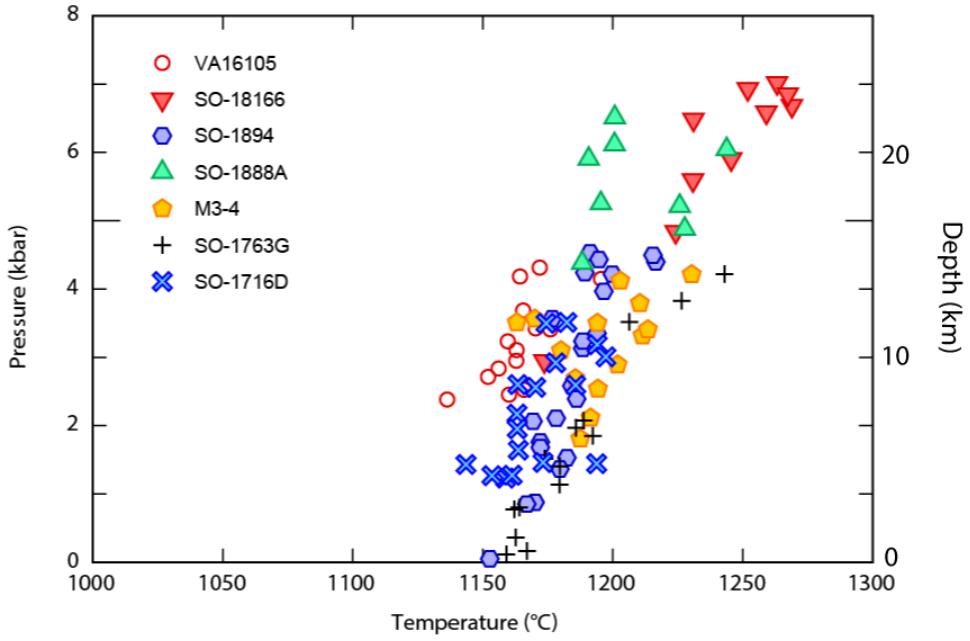

Figure 41. Temperature and pressure results for other hypabyssal intrusions using the Wang et al. (2021) thermobarometer.

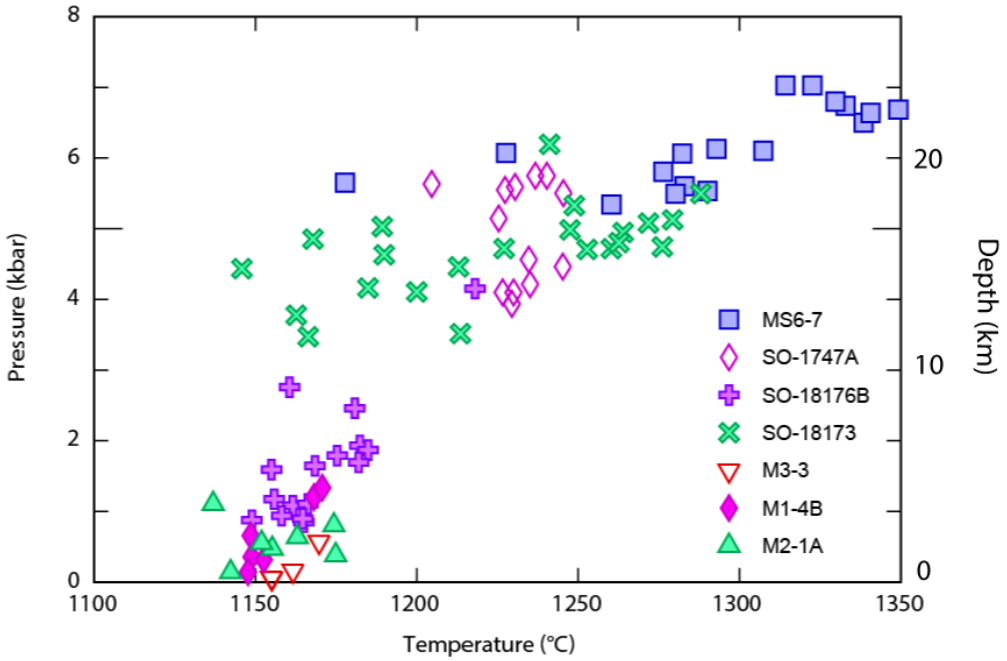

Figure 42. Temperature and pressure results for pyroclastic bombs using the Wang et al. (2021) thermobarometer.

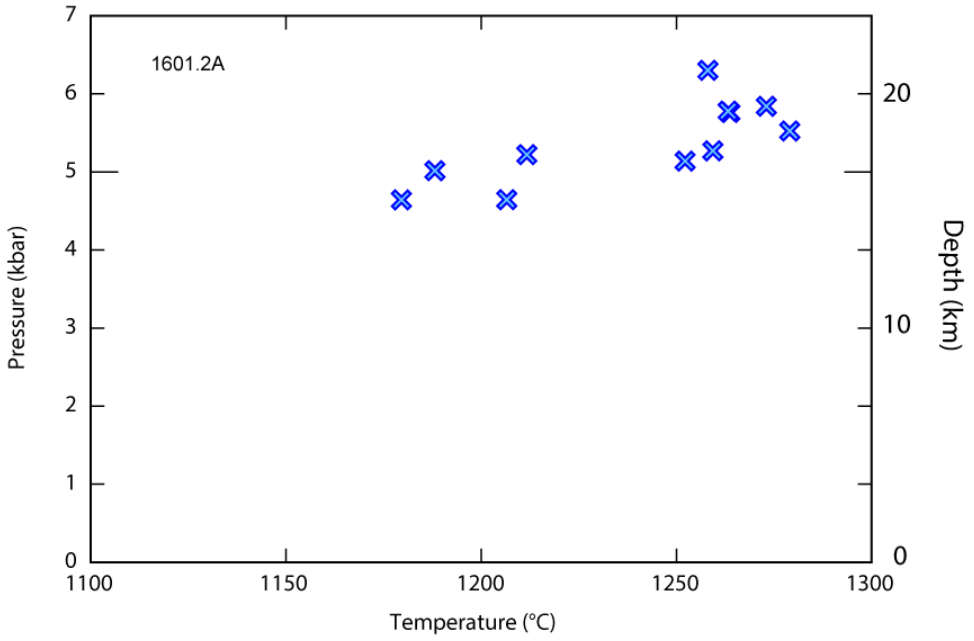

Figure 43. Temperature and pressure results for bedded lapillistone using the Wang et al. (2021) thermobarometer.

IV. DISCUSSION AND CONCLUSIONS

Cpx Chemistry

Cpx compositions generally range from diopside to augite for all samples analyzed in this study (Figure 25). The tight clustering of cpx compositions in pyroclastic deposits and the different types of hypabyssal intrusions suggests all these units are broadly petrogenetically related (Figures 26-30). This conclusion is also supported by the typical fractionation trends shown in cpx chemical variation diagrams (Figures 31-34). This is especially true for the well-defined trend between Mg# vs. FeO (Figure 31). The cpx fractionation trends are clearer than those seen in the whole-rock Harker variation diagrams (Figures 10-15). This could be due to the effects of alteration on the whole-rock oxides, which cpx is resistant to.

Samples from sill packages 1, 2, and 3 (samples KB43-16, PO7-16, and G56-16) cluster within the augite field on the pyroxene quadrilateral (Figure 26). Sample KB43-16 also contains some sub-calcic augite. This type of augite forms during rapid cooling of high temperature magma (Deer et al., 2013), consistent with the fact that this sample was collected from the sill's lower chilled margin. Cpx fractionation trends defined by FeO, MnO, MgO, Cr_2O_3, and Mg# differ from the other samples in Figures 31-34, indicating a somewhat different petrogenetic history and derivation from a separate magma reservoir. The data for the three sill packages are also tightly clustered in these figures, providing evidence that the sills are part of an interconnected feeder network, which may have transported magma laterally for significant distances through the host sedimentary sequences (e.g., Magee et al., 2016).

Another hypabyssal intrusion (sample VA16105) has cpx compositions that cluster mainly within the augite field on the pyroxene quadrilateral (Figure 28). This sample also tends to plot separately from the sill packages and other samples on cpx variation diagrams. This

indicates the intrusion represents a separate magma batch from all the other samples, pointing to additional complexities in the magma plumbing system. The additional insights that are provided by cpx compositions and fractionation trends for the sill packages and VA16105 are not seen in the whole-rock chemistry and discrimination diagrams.

Six samples from Ohrmundt's field area are enriched in Ti (Figure 36) relative to the other samples. However, it is important to note that these samples (M1-1A, M2-1A, M1-4B, M3-3, SO-1763G, and SO-1716D) do not plot separately from the other samples in composition or fractionation trends. Higher Ti is only seen in the whole-rock chemistry for two of these samples (M2-1A and M3-3). In Figure 37, these six samples also plot within a different field on the cpx discrimination diagram. The reason for the Ti enrichment in these six samples requires a more in-depth study.

Geothermobarometry

Comparisons between the Putirka (2008) and Wang et al. (2021) thermobarometers indicate that the latter thermobarometer may give more reliable results. It yields less negative pressures and better precision (lower SEE). Calculated temperatures using the Wang et al. (2021) thermometer for all the samples generally give reasonable values for basaltic andesites and other volcanic rocks of similar compositions (e.g., Sheehan and Barclay, 2016; Feng and Zhu, 2019). There is a wide range in temperatures (~1150-1250 °C) for the samples in this study, however, which is likely due to magma mixing during cpx crystallization.

Sill package samples with unusually high pressures result in cpx crystallization depths up to ~46 km. These pressures should be treated with great caution. Part of the problem with inconsistent pressures could be that the Wang et al. (2021) barometer is only calibrated for pressures up to 12 kbar, meaning that the cpx in some of my samples might have crystallized out

of the calibration range for the barometer. Some samples also give negative values for both the Putirka (2008) and Wang et al. (2021) techniques, but the error bars on these values (Appendix III) suggest that the cpx could have equilibrated at shallow depths beneath the surface.

Most cpx samples within the data set show a downward trend in pressures from 6-7 kbar for pyroclastic bombs, agglutinate, other hypabyssal intrusions, and bedded lapillistone. This trend could be consistent with magma staging in the mid-crust, as commonly seen in volcanic arc settings (e.g., Rossel et al., 2015). If this is a valid conclusion, the downward trend shown by the calculated pressures could record continued cpx crystallization and growth in the magma moving upwards within the crust, leading to eruption or intrusion at shallow depths beneath the surface. However, some of the downward trend could be partly the result of alteration or disequilibrium effects.

APPENDIX I: EPMA DATA

Table 9. Sample KB43-16 wt% of major oxides. FeO* indicates total Fe is reported as FeO

Crystal	SiO_2	TiO_2	Al_2O_3	FeO*	MnO	MgO	CaO	Na_2O	K_2O	Cr_2O_3	Total wt%
1	48.12	0.00	6.52	11.44	0.48	14.86	11.85	0.64	0.34	0.01	94.26
1	51.58	0.00	0.75	6.79	0.61	13.82	22.39	0.23	0.02	0.00	96.18
1	49.76	0.01	1.95	10.99	0.28	13.99	17.78	0.31	0.01	0.03	95.11
2	48.03	0.01	5.20	9.21	0.64	12.14	15.57	0.88	0.09	0.01	91.79
2	50.95	0.00	1.98	7.76	0.84	12.33	19.71	0.26	0.20	0.02	94.04
3	51.92	0.02	1.29	11.25	0.34	14.16	18.36	0.28	0.06	0.02	97.70
3	51.63	0.00	1.23	11.32	0.34	14.10	18.27	0.33	0.05	0.02	97.29
4	50.99	0.01	1.25	10.31	0.27	14.46	18.19	0.29	0.05	0.01	95.81
4	51.53	0.04	1.22	10.54	0.29	15.19	17.35	0.27	0.03	0.00	96.46
5	48.74	0.00	1.15	10.92	0.30	13.16	18.08	0.31	0.01	0.01	92.67
5	48.75	0.00	1.27	10.89	0.32	13.09	18.16	0.27	0.01	0.00	92.75
5	48.97	0.03	1.28	10.65	0.32	12.95	18.04	0.29	0.00	0.00	92.53
5	49.03	0.01	1.25	10.74	0.28	12.89	18.06	0.28	0.01	0.00	92.55
5	50.21	0.00	1.42	10.98	0.32	13.19	18.40	0.28	0.01	0.04	94.85
5	50.07	0.00	1.26	11.09	0.25	13.14	18.29	0.29	0.01	0.02	94.40
6	50.26	0.00	1.19	10.94	0.27	13.61	17.87	0.26	0.02	0.05	94.45
6	50.18	0.01	1.29	11.02	0.30	13.37	17.65	0.31	0.02	0.02	94.16

Table 10. Sample PO7-16 wt% of major oxides. FeO* indicates total Fe is reported as FeO

Crystal	SiO_2	TiO_2	Al_2O_3	FeO*	MnO	MgO	CaO	Na_2O	K_2O	Cr_2O_3	Total wt%
1	51.39	0.01	0.50	14.12	0.51	11.32	19.75	0.35	0.00	0.07	98.02
1	50.83	0.01	0.67	12.95	0.39	11.51	20.88	0.32	0.01	0.05	97.61
1	50.95	0.02	2.12	8.98	0.26	15.48	18.90	0.32	0.00	0.12	97.13
1	50.75	0.00	2.35	8.98	0.26	15.32	19.06	0.31	0.00	0.13	97.16
1	50.39	0.00	3.00	9.18	0.27	14.88	18.66	0.35	0.00	0.25	96.97
1	50.78	0.01	2.11	9.13	0.24	15.25	18.79	0.37	0.00	0.08	96.76
1	50.36	0.00	2.22	9.35	0.25	15.01	18.78	0.35	0.00	0.12	96.45
2	51.63	0.00	2.61	8.97	0.29	14.73	19.29	0.32	0.02	0.23	98.09
2	51.25	0.00	2.54	9.18	0.23	15.06	19.32	0.34	0.03	0.16	98.09
2	49.99	0.00	2.30	9.51	0.23	14.91	18.84	0.33	0.00	0.12	96.24
2	49.98	0.04	2.11	9.49	0.25	14.91	18.74	0.35	0.00	0.05	95.91
2	49.59	0.01	2.38	10.15	0.26	14.57	18.93	0.33	0.00	0.07	96.29
3	52.27	0.00	0.53	12.60	0.44	12.19	20.24	0.26	0.00	0.05	98.57
3	51.01	0.04	2.43	8.81	0.22	15.26	19.78	0.29	0.00	0.22	98.06
3	50.67	0.00	2.35	9.81	0.26	14.83	18.68	0.33	0.00	0.11	97.03
3	50.73	0.02	2.42	10.28	0.27	14.72	18.38	0.35	0.00	0.04	97.20
4	50.64	0.01	2.15	8.82	0.26	15.05	19.29	0.33	0.00	0.11	96.65

Table 11. Sample G56-16 wt% of major oxides. FeO* indicates total Fe is reported as FeO

Crystal	SiO_2	TiO_2	Al_2O_3	FeO*	MnO	MgO	CaO	Na_2O	K_2O	Cr_2O_3	Total wt%
1	53.09	0.00	2.62	10.08	0.33	14.04	16.83	0.56	0.00	0.00	97.54
2	50.39	0.07	1.64	10.60	0.34	13.88	18.05	0.27	0.00	0.00	95.24
3	51.08	0.00	1.80	10.31	0.28	14.39	17.59	0.26	0.00	0.00	95.72
4	51.78	0.02	1.95	10.22	0.25	13.87	17.75	0.26	0.00	0.00	96.11
4	50.31	0.01	1.73	10.76	0.26	14.14	17.73	0.28	0.00	0.00	95.22

Table 12. Sample M6-4 wt% of major oxides. FeO* indicates total Fe is reported as FeO

Crystal	SiO_2	TiO_2	Al_2O_3	FeO*	MnO	MgO	CaO	Na_2O	K_2O	Cr_2O_3	Total wt%
1	50.85	0.00	1.78	5.73	0.17	15.74	20.09	0.21	0.03	0.22	94.82
1	49.93	0.00	2.07	6.92	0.20	14.71	19.92	0.22	0.04	0.07	94.06
1	49.71	0.01	2.21	7.01	0.16	14.76	20.00	0.20	0.02	0.09	94.16
1	50.52	0.00	1.76	5.86	0.17	15.58	19.73	0.21	0.02	0.32	94.18
1	48.62	0.03	3.51	6.02	0.15	14.00	20.53	0.36	0.01	0.66	93.90
2	48.73	0.01	3.17	5.72	0.17	14.11	20.95	0.30	0.01	0.89	94.04
2	48.78	0.00	3.11	6.51	0.12	13.58	21.63	0.31	0.02	0.08	94.16
2	48.59	0.03	3.24	6.83	0.17	13.68	21.34	0.32	0.03	0.16	94.39
3	46.81	0.00	4.35	7.65	0.14	13.00	20.04	0.28	0.07	0.05	92.38
3	47.60	0.00	3.67	6.47	0.17	13.84	20.47	0.27	0.02	0.42	92.94
3	47.49	0.00	3.64	6.29	0.13	13.56	20.55	0.32	0.01	0.50	92.49

Table 13. Sample VA1603 wt% of major oxides. FeO* indicates total Fe is reported as FeO

Crystal	SiO_2	TiO_2	Al_2O_3	FeO*	MnO	MgO	CaO	Na_2O	K_2O	Cr_2O_3	Total wt%
1	50.84	0.00	3.23	5.44	0.11	14.97	21.95	0.24	0.01	0.12	96.90
1	52.50	0.00	1.82	4.15	0.10	15.78	22.32	0.20	0.00	0.62	97.48
1	51.91	0.00	2.32	4.78	0.12	15.78	21.95	0.22	0.00	0.38	97.44
1	52.17	0.00	2.16	4.57	0.11	15.78	21.95	0.24	0.02	0.40	97.38
1	51.00	0.05	3.08	5.87	0.15	14.99	21.30	0.25	0.01	0.15	96.85
1	50.37	0.00	3.62	7.19	0.16	14.80	19.95	0.29	0.01	0.12	96.51
1	50.72	0.02	3.04	6.70	0.16	14.80	20.53	0.27	0.01	0.10	96.33
2	52.19	0.01	1.72	4.81	0.11	15.93	22.50	0.17	0.01	0.12	97.56
2	52.41	0.02	1.85	4.62	0.09	15.83	22.42	0.19	0.00	0.14	97.58
2	51.73	0.01	1.89	4.71	0.10	15.34	22.50	0.20	0.01	0.24	96.73
2	52.45	0.01	1.89	4.20	0.11	16.09	22.46	0.20	0.01	0.57	97.98
2	52.55	0.03	1.69	4.55	0.16	16.05	22.37	0.22	0.00	0.16	97.79
3	52.44	0.00	1.92	4.85	0.10	15.91	22.61	0.21	0.00	0.17	98.21
3	52.17	0.03	1.99	4.84	0.11	16.03	21.95	0.26	0.00	0.29	97.66
3	52.02	0.00	1.95	4.31	0.14	16.18	21.97	0.27	0.00	0.71	97.55
3	52.21	0.02	1.61	4.00	0.14	16.45	22.43	0.21	0.00	0.48	97.54
3	52.23	0.00	1.35	4.29	0.15	16.23	22.32	0.23	0.00	0.44	97.24
3	51.97	0.02	1.65	5.15	0.10	16.33	21.50	0.21	0.00	0.49	97.41
3	51.20	0.00	1.78	5.29	0.17	15.76	22.08	0.18	0.00	0.08	96.52

Table 14. Sample SO-18126A wt% of major oxides. FeO* indicates total Fe is reported as FeO

Crystal	SiO_2	TiO_2	Al_2O_3	FeO*	MnO	MgO	CaO	Na_2O	K_2O	Cr_2O_3	Total wt%
1	50.08	0.01	2.90	6.09	0.14	14.76	21.60	0.28	0.01	0.39	96.25
1	48.33	0.00	4.24	7.59	0.15	13.46	21.17	0.30	0.00	0.10	95.33
1	51.12	0.00	1.66	8.77	0.22	14.40	20.12	0.33	0.00	0.03	96.63
1	48.59	0.00	4.44	7.70	0.17	13.50	20.98	0.36	0.00	0.08	95.83
1	49.49	0.00	3.70	6.60	0.15	14.29	21.66	0.33	0.02	0.23	96.47
2	52.50	0.02	2.37	5.44	0.32	16.34	19.98	0.60	0.07	0.26	97.91
2	52.25	0.00	2.08	6.09	0.16	15.44	20.37	0.31	0.05	0.31	97.06
2	51.40	0.01	2.40	5.03	0.27	15.19	20.57	0.55	0.04	0.38	95.83
2	51.00	0.00	2.23	5.01	0.30	15.89	21.33	0.56	0.08	0.04	96.44
3	49.47	0.02	3.37	8.52	0.23	14.10	20.32	0.39	0.00	0.00	96.42
3	49.40	0.01	3.14	8.17	0.19	14.18	20.80	0.33	0.01	0.00	96.24
3	50.49	0.00	2.60	6.04	0.29	15.22	20.86	0.59	0.06	0.01	96.16
4	47.68	0.01	4.89	7.70	0.14	13.29	21.67	0.32	0.01	0.22	95.93
4	47.88	0.00	4.28	8.61	0.22	13.15	20.85	0.36	0.02	0.03	95.41
4	48.54	0.00	3.67	8.78	0.23	13.64	20.41	0.37	0.03	0.01	95.68
4	48.34	0.00	4.14	8.11	0.20	13.46	20.94	0.31	0.01	0.08	95.57
4	50.56	0.00	1.93	8.17	0.30	14.37	19.08	0.32	0.00	0.00	94.73
4	52.41	0.00	2.23	7.90	0.28	14.58	19.29	0.30	0.04	0.00	97.03

Table 15. Sample SO-1767 C wt% of major oxides. FeO* indicates total Fe is reported as FeO

Crystal	SiO_2	TiO_2	Al_2O_3	FeO*	MnO	MgO	CaO	Na_2O	K_2O	Cr_2O_3	Total wt%
1	51.69	0.03	2.20	5.18	0.18	15.87	20.38	0.42	0.00	0.59	96.53
1	51.59	0.00	2.34	5.25	0.14	15.97	20.31	0.42	0.00	0.73	96.74
1	51.42	0.00	2.26	5.28	0.12	16.06	20.13	0.44	0.01	0.67	96.41
1	51.05	0.00	2.47	5.44	0.13	16.06	19.99	0.45	0.02	0.69	96.31
1	51.29	0.01	1.87	4.97	0.12	16.36	20.60	0.39	0.01	0.45	96.06
2	51.02	0.00	1.71	5.65	0.17	16.25	20.33	0.24	0.02	0.49	95.88
2	50.67	0.02	1.89	5.58	0.28	16.35	18.90	0.42	0.01	0.58	94.69
3	51.46	0.00	1.88	5.49	0.20	16.06	20.83	0.34	0.03	0.40	96.69
3	51.15	0.00	1.64	5.60	0.16	15.86	20.87	0.22	0.02	0.56	96.08
4	51.85	0.02	1.63	5.14	0.14	15.98	21.64	0.22	0.00	0.25	96.86
4	51.81	0.07	1.74	4.91	0.11	16.13	21.27	0.36	0.00	0.75	97.13
4	50.43	0.00	2.95	6.33	0.17	14.89	20.45	0.42	0.00	0.20	95.83

Table 16. Sample M1-1A wt% of major oxides. FeO* indicates total Fe is reported as FeO

Crystal	SiO_2	TiO_2	Al_2O_3	FeO*	MnO	MgO	CaO	Na_2O	K_2O	Cr_2O_3	Total wt%
1	51.66	0.45	2.33	6.38	0.19	14.61	22.47	0.29	0.00	0.34	98.70
1	50.66	0.54	2.34	7.06	0.18	13.93	22.47	0.29	0.00	0.30	97.77
1	51.33	0.39	1.95	6.43	0.13	14.54	22.57	0.23	0.00	0.31	97.88
1	51.25	0.47	1.73	6.20	0.17	14.39	23.16	0.24	0.00	0.33	97.94
1	50.38	0.59	2.69	6.84	0.29	13.78	22.90	0.32	0.00	0.26	98.05
2	50.95	0.59	2.95	7.16	0.17	13.66	22.19	0.29	0.00	0.28	98.24
2	50.36	0.74	3.10	7.12	0.19	13.40	23.08	0.34	0.01	0.37	98.70
2	51.89	0.41	1.71	6.94	0.24	14.35	22.35	0.26	0.00	0.17	98.32
2	52.64	0.42	1.80	6.37	0.22	14.61	22.92	0.25	0.02	0.28	99.53
2	51.53	0.54	2.37	6.40	0.15	13.79	23.42	0.25	0.01	0.63	99.09
2	51.67	0.51	2.37	6.56	0.16	13.93	23.10	0.32	0.00	0.46	99.08
2	51.62	0.55	2.47	6.41	0.20	13.66	22.89	0.29	0.00	0.44	98.52
3	50.45	0.60	2.75	6.88	0.18	13.50	22.71	0.34	0.03	0.33	97.77
3	49.33	0.89	4.36	8.18	0.21	12.85	22.07	0.36	0.00	0.09	98.34
3	49.99	0.62	2.54	6.98	0.17	13.52	23.00	0.27	0.00	0.32	97.40
3	50.37	0.58	2.71	7.38	0.19	13.78	21.76	0.39	0.03	0.23	97.43
3	48.19	0.92	3.74	8.60	0.19	11.95	22.31	0.29	0.00	0.05	96.24
4	49.55	0.73	3.51	8.00	0.24	13.00	22.11	0.36	0.00	0.14	97.64
4	51.30	0.55	1.95	7.11	0.18	13.83	22.26	0.23	0.00	0.28	97.69
4	51.32	0.45	2.03	7.35	0.18	13.46	22.22	0.25	0.00	0.16	97.41
4	52.01	0.55	2.03	7.24	0.19	14.20	22.02	0.21	0.00	0.10	98.54
4	49.69	0.53	2.22	8.11	0.16	13.16	21.47	0.29	0.00	0.10	95.73
4	51.36	0.57	2.40	7.38	0.21	13.73	21.78	0.29	0.00	0.15	97.87

Table 17. Sample VA16105 wt% of major oxides. FeO* indicates total Fe is reported as FeO

Crystal	SiO_2	TiO_2	Al_2O_3	FeO*	MnO	MgO	CaO	Na_2O	K_2O	Cr_2O_3	Total wt%
1	50.89	0.00	1.57	10.73	0.32	13.51	19.31	0.29	0.01	0.00	96.64
1	50.68	0.02	1.47	9.16	0.31	14.55	19.00	0.33	0.00	0.00	95.51
1	51.27	0.00	1.42	8.90	0.26	13.94	19.29	0.28	0.01	0.06	95.42
1	51.08	0.01	1.47	8.54	0.23	14.19	19.84	0.32	0.00	0.05	95.73
2	51.31	0.01	1.13	8.82	0.32	14.78	18.99	0.22	0.00	0.08	95.66
2	50.19	0.00	2.26	9.10	0.22	13.38	20.31	0.34	0.00	0.06	95.87
2	50.74	0.00	1.72	8.14	0.23	14.01	20.64	0.30	0.00	0.11	95.89
2	50.31	0.01	1.99	9.06	0.26	13.47	19.49	0.35	0.00	0.05	94.98
2	50.73	0.00	1.73	8.30	0.25	13.99	20.25	0.30	0.02	0.15	95.71
3	49.72	0.01	2.47	9.42	0.23	13.18	19.62	0.37	0.01	0.05	95.07
3	49.93	0.03	2.46	9.00	0.21	13.26	20.17	0.34	0.01	0.05	95.45
3	50.77	0.00	1.68	8.17	0.22	13.24	20.90	0.31	0.00	0.10	95.39
3	50.98	0.00	1.70	8.28	0.23	13.56	20.88	0.32	0.00	0.11	96.06
3	49.86	0.00	2.12	9.07	0.23	12.96	20.44	0.28	0.02	0.03	95.00

Table 18. Sample SO-1716 D wt% of major oxides. FeO* indicates total Fe is reported as FeO

Crystal	SiO_2	TiO_2	Al_2O_3	FeO*	MnO	MgO	CaO	Na_2O	K_2O	Cr_2O_3	Total wt%
1	52.03	0.27	2.51	7.23	0.22	14.93	20.99	0.30	0.01	0.16	98.64
1	51.40	0.30	2.31	7.24	0.25	14.79	21.19	0.29	0.00	0.20	97.97
1	50.33	0.43	2.74	6.87	0.19	14.15	21.94	0.30	0.03	0.37	97.34
1	50.20	0.40	3.06	7.41	0.19	14.13	20.70	0.37	0.00	0.28	96.73
2	49.95	0.45	3.05	7.31	0.14	13.77	21.69	0.33	0.00	0.32	97.00
2	50.57	0.38	3.24	7.16	0.18	14.36	21.55	0.33	0.00	0.32	98.08
2	50.09	0.51	2.85	7.27	0.18	13.82	21.60	0.24	0.01	0.22	96.77
2	49.24	0.69	3.80	8.10	0.18	13.11	21.70	0.28	0.00	0.12	97.21
2	50.92	0.40	2.09	4.89	0.07	14.66	23.35	0.28	0.00	0.59	97.25
2	51.11	0.35	2.51	5.08	0.15	14.52	22.97	0.23	0.00	0.65	97.58
2	50.29	0.54	2.92	5.93	0.17	13.95	22.56	0.26	0.01	0.46	97.08
3	52.19	0.29	2.08	7.45	0.16	14.96	20.65	0.27	0.03	0.19	98.26
3	52.36	0.32	2.03	6.88	0.16	14.94	21.21	0.27	0.00	0.20	98.37
3	50.69	0.43	2.72	6.72	0.17	14.10	22.02	0.26	0.01	0.30	97.42
3	52.23	0.23	2.15	7.13	0.19	14.92	21.53	0.32	0.01	0.09	98.80
3	50.78	0.34	2.63	7.75	0.21	14.00	21.31	0.34	0.00	0.08	97.44
3	51.12	0.29	2.30	6.20	0.13	15.00	21.67	0.36	0.01	0.18	97.27
4	49.32	0.76	4.16	8.57	0.20	12.74	21.63	0.26	0.01	0.04	97.68
4	53.59	0.14	1.23	4.22	0.12	15.99	22.59	0.26	0.00	0.76	98.90
4	52.05	0.19	1.71	5.62	0.16	15.48	21.45	0.28	0.00	0.55	97.50
4	51.32	0.15	1.41	4.83	0.15	15.51	22.44	0.29	0.00	0.57	96.66
4	51.76	0.13	1.30	4.04	0.11	15.80	22.83	0.26	0.01	0.69	96.92

Table 19. Sample SO-1763 G wt% of major oxides. FeO* indicates total Fe is reported as FeO

Crystal	SiO_2	TiO_2	Al_2O_3	FeO*	MnO	MgO	CaO	Na_2O	K_2O	Cr_2O_3	Total wt%
1	52.29	0.28	2.01	5.33	0.15	15.81	22.80	0.26	0.00	0.52	99.45
1	52.27	0.22	1.68	5.02	0.12	15.65	23.35	0.23	0.00	0.62	99.15
1	52.34	0.18	1.15	4.81	0.17	15.76	22.65	0.21	0.01	0.57	97.86
2	52.10	0.34	1.82	6.50	0.14	15.04	22.52	0.21	0.00	0.12	98.80
2	52.31	0.31	1.67	6.60	0.22	14.84	22.26	0.17	0.00	0.09	98.46
2	51.23	0.44	2.18	6.60	0.17	14.52	22.84	0.22	0.00	0.12	98.33
2	52.23	0.33	1.65	5.79	0.15	14.84	23.14	0.26	0.01	0.25	98.64
2	51.02	0.40	2.14	5.83	0.15	14.19	23.62	0.20	0.00	0.46	98.01
2	52.16	0.44	2.42	6.37	0.13	14.25	22.58	0.23	0.00	0.26	98.84
2	52.22	0.33	1.89	5.83	0.25	14.29	22.13	0.33	0.02	0.45	97.73
3	53.55	0.15	1.14	4.58	0.17	16.47	21.58	0.23	0.00	0.42	98.29
3	52.01	0.29	2.11	5.72	0.14	14.79	22.74	0.23	0.00	0.47	98.51
3	50.95	0.27	2.21	6.08	0.12	14.35	22.53	0.24	0.00	0.58	97.33
3	53.62	0.11	1.18	3.88	0.15	16.23	22.92	0.27	0.00	0.66	99.03
3	52.47	0.23	1.45	4.79	0.18	15.28	22.77	0.29	0.00	0.65	98.11
4	52.73	0.21	1.58	4.85	0.10	15.72	22.69	0.24	0.01	0.51	98.63
4	52.07	0.21	1.30	4.76	0.17	15.33	22.64	0.25	0.00	0.46	97.19
4	51.97	0.22	1.62	4.87	0.12	15.38	22.71	0.25	0.00	0.58	97.72

Table 20. Sample M3-4 wt% of major oxides. FeO* indicates total Fe is reported as FeO

Crystal	SiO_2	TiO_2	Al_2O_3	FeO*	MnO	MgO	CaO	Na_2O	K_2O	Cr_2O_3	Total wt%
1	48.64	0.00	3.51	8.79	0.26	12.69	20.64	0.31	0.13	0.00	94.96
1	51.53	0.03	1.65	6.48	0.20	15.76	20.15	0.22	0.01	0.07	96.10
1	52.14	0.00	1.42	6.07	0.18	16.00	20.06	0.16	0.00	0.20	96.24
1	51.97	0.01	1.60	6.28	0.20	16.11	20.03	0.17	0.00	0.12	96.49
1	50.73	0.01	2.65	5.82	0.17	14.80	21.23	0.22	0.03	0.50	96.15
2	49.29	0.00	2.92	7.45	0.18	14.27	20.33	0.22	0.01	0.00	94.66
2	50.65	0.00	1.65	6.21	0.12	15.85	19.97	0.15	0.01	0.09	94.71
3	48.67	0.01	4.32	8.34	0.21	13.03	20.88	0.24	0.07	0.00	95.76
3	51.98	0.03	1.42	5.34	0.16	15.98	21.04	0.17	0.01	0.29	96.42
3	51.47	0.00	1.56	5.45	0.13	15.97	21.27	0.19	0.02	0.20	96.25
4	50.91	0.00	2.03	6.50	0.17	15.11	21.01	0.18	0.01	0.05	95.96
4	51.60	0.00	1.54	5.87	0.13	15.74	20.87	0.15	0.00	0.16	96.05
4	52.04	0.00	1.24	4.92	0.12	16.23	21.23	0.19	0.00	0.31	96.27
4	50.63	0.02	2.27	5.20	0.11	15.56	21.60	0.22	0.02	0.75	96.37

Table 21. Sample SO-1888A wt% of major oxides. FeO* indicates total Fe is reported as FeO

Crystal	SiO_2	TiO_2	Al_2O_3	FeO*	MnO	MgO	CaO	Na_2O	K_2O	Cr_2O_3	Total wt%
1	50.96	0.00	2.63	7.70	0.19	14.29	20.55	0.29	0.00	0.02	96.63
1	50.83	0.00	2.77	7.89	0.19	13.38	20.77	0.46	0.00	0.01	96.29
1	50.71	0.00	3.16	7.91	0.19	13.43	20.77	0.50	0.00	0.04	96.70
1	50.61	0.00	3.14	7.73	0.16	13.63	21.26	0.42	0.00	0.01	96.96
1	50.62	0.00	2.98	8.05	0.23	13.40	20.81	0.47	0.00	0.03	96.60
2	52.44	0.00	1.47	5.49	0.14	15.17	21.84	0.31	0.00	0.27	97.13
2	51.86	0.01	1.52	5.43	0.15	14.96	21.62	0.36	0.00	0.27	96.19
2	52.30	0.00	1.65	5.51	0.16	15.21	21.34	0.35	0.00	0.21	96.73

Table 22. Sample SO-1894 wt% of major oxides. FeO* indicates total Fe is reported as FeO

Crystal	SiO_2	TiO_2	Al_2O_3	FeO*	MnO	MgO	CaO	Na_2O	K_2O	Cr_2O_3	Total wt%
1	51.58	0.00	1.67	6.84	0.19	15.69	20.16	0.23	0.00	0.16	96.52
1	50.11	0.00	2.16	7.33	0.19	15.01	20.90	0.20	0.00	0.06	95.97
1	49.72	0.00	2.51	7.54	0.20	14.79	20.05	0.19	0.01	0.18	95.19
1	50.66	0.02	2.51	6.37	0.16	15.05	21.43	0.27	0.02	0.29	96.77
1	51.47	0.01	2.52	6.63	0.13	15.14	21.33	0.24	0.00	0.30	97.76
2	51.13	0.00	2.14	7.01	0.17	15.26	20.86	0.20	0.03	0.16	96.96
2	50.90	0.00	2.03	6.12	0.18	15.74	21.18	0.24	0.01	0.34	96.73
2	51.14	0.02	1.72	6.99	0.20	15.43	20.56	0.23	0.02	0.07	96.39
2	51.61	0.00	1.58	6.52	0.21	16.01	20.73	0.20	0.02	0.22	97.11
2	51.29	0.03	1.69	5.71	0.13	15.90	21.17	0.25	0.00	0.36	96.52
2	51.81	0.00	1.57	5.95	0.15	15.95	21.24	0.20	0.02	0.37	97.24
3	49.83	0.00	3.66	7.47	0.21	14.33	20.64	0.32	0.02	0.10	96.58
3	48.68	0.00	4.13	8.14	0.15	13.41	20.80	0.26	0.00	0.05	95.62
3	50.00	0.04	2.51	6.51	0.17	14.98	21.10	0.24	0.00	0.34	95.88
3	50.76	0.00	2.33	6.26	0.18	14.99	21.12	0.28	0.02	0.48	96.42
3	51.17	0.01	2.50	5.95	0.15	15.65	21.50	0.29	0.00	0.58	97.80
4	50.35	0.00	3.24	7.07	0.16	14.21	21.02	0.30	0.01	0.30	96.66
4	51.85	0.00	2.36	6.29	0.15	15.17	21.04	0.22	0.00	0.35	97.43
4	50.96	0.00	2.58	6.31	0.15	14.89	21.28	0.32	0.00	0.54	97.02
4	50.99	0.00	2.49	6.39	0.17	15.03	20.76	0.27	0.01	0.48	96.59
4	51.23	0.00	2.36	6.14	0.15	14.91	20.90	0.24	0.00	0.47	96.41
4	49.50	0.00	3.71	7.78	0.13	13.92	20.49	0.28	0.00	0.17	95.98

Table 23. Sample SO-18166 wt% of major oxides. FeO* indicates total Fe is reported as FeO

Crystal	SiO_2	TiO_2	Al_2O_3	FeO*	MnO	MgO	CaO	Na_2O	K_2O	Cr_2O_3	Total wt%
1	51.52	0.00	1.30	4.37	0.09	15.32	21.46	0.39	0.00	0.24	94.70
1	51.31	0.00	1.31	4.37	0.13	15.36	21.22	0.42	0.00	0.36	94.50
1	51.49	0.00	1.46	4.54	0.13	15.52	21.71	0.38	0.02	0.24	95.49
2	50.37	0.02	1.48	7.40	0.24	14.20	20.25	0.26	0.02	0.00	94.25
2	51.41	0.00	1.04	4.08	0.11	15.67	21.06	0.32	0.00	0.36	94.04
2	51.43	0.00	1.11	4.55	0.15	15.65	20.93	0.33	0.00	0.30	94.46
3	51.05	0.00	1.05	4.98	0.18	15.62	20.60	0.29	0.01	0.14	93.92
3	51.57	0.04	1.20	4.08	0.11	15.58	21.31	0.39	0.01	0.42	94.72
3	50.14	0.00	2.21	5.69	0.15	14.97	20.36	0.46	0.00	0.19	94.17
3	51.57	0.00	1.38	4.35	0.09	15.55	21.06	0.37	0.00	0.50	94.87

Table 24. Sample MS6-7 wt% of major oxides. FeO* indicates total Fe is reported as FeO

Crystal	SiO_2	TiO_2	Al_2O_3	FeO*	MnO	MgO	CaO	Na_2O	K_2O	Cr_2O_3	Total wt%
1	48.67	0.00	4.50	8.88	0.21	11.88	20.26	0.35	0.04	0.00	94.78
1	50.66	0.02	2.58	7.04	0.23	12.24	19.27	0.29	0.03	0.03	92.38
1	49.60	0.00	3.81	7.40	0.18	12.31	20.72	0.34	0.01	0.12	94.49
2	52.05	0.02	1.93	5.99	0.20	14.09	20.53	0.22	0.08	0.12	95.22
2	52.05	0.01	1.99	6.21	0.16	14.06	20.09	0.18	0.06	0.05	94.86
2	51.87	0.03	2.16	6.78	0.16	13.83	20.01	0.17	0.03	0.00	95.02
2	51.60	0.00	2.30	5.98	0.18	13.78	21.02	0.18	0.00	0.02	95.04
3	53.06	0.00	1.80	4.22	0.09	14.27	22.16	0.19	0.00	0.68	96.48
3	52.85	0.00	1.78	4.06	0.10	14.53	22.37	0.26	0.00	0.65	96.59
3	52.25	0.00	1.23	3.89	0.12	14.30	22.04	0.20	0.00	0.49	94.52
3	53.37	0.02	1.30	4.06	0.12	14.51	22.50	0.24	0.02	0.49	96.63
3	53.44	0.00	1.34	4.00	0.09	14.40	22.48	0.18	0.00	0.45	96.37
3	53.18	0.01	1.34	3.92	0.10	14.58	22.38	0.18	0.00	0.44	96.13
4	51.08	0.02	3.20	5.32	0.12	13.09	21.82	0.23	0.01	0.95	95.81
4	50.58	0.00	3.39	5.50	0.11	12.94	21.33	0.27	0.03	0.97	95.12
4	50.57	0.02	3.26	5.63	0.16	13.46	21.14	0.21	0.01	0.89	95.36
4	50.29	0.00	3.62	5.77	0.12	12.89	21.14	0.23	0.01	0.66	94.72

Table 25. Sample M1-4B wt% of major oxides. FeO* indicates total Fe is reported as FeO

Crystal	SiO_2	TiO_2	Al_2O_3	FeO*	MnO	MgO	CaO	Na_2O	K_2O	Cr_2O_3	Total wt%
1	50.35	0.61	3.26	7.16	0.17	13.73	23.19	0.33	0.02	0.04	98.86
1	51.27	0.48	2.18	6.41	0.18	14.87	22.90	0.21	0.01	0.26	98.77
1	49.96	0.65	3.75	7.17	0.15	13.39	23.14	0.29	0.02	0.12	98.63
1	51.10	0.65	3.28	6.49	0.15	13.84	23.89	0.29	0.00	0.37	100.06
1	50.07	0.64	3.38	6.39	0.15	13.94	23.23	0.37	0.00	0.71	98.87
1	52.24	0.44	1.99	6.86	0.17	14.87	21.91	0.20	0.00	0.15	98.84
1	51.99	0.43	1.94	7.15	0.19	15.14	22.05	0.24	0.01	0.12	99.26
2	50.63	0.50	3.16	6.44	0.16	14.18	23.37	0.26	0.01	0.26	98.96
2	52.07	0.42	2.15	6.44	0.16	15.31	21.94	0.28	0.02	0.25	99.04
2	50.33	0.52	2.99	6.20	0.13	14.05	23.63	0.32	0.00	0.33	98.50
2	49.16	0.90	3.77	6.79	0.11	13.59	22.95	0.32	0.00	0.59	98.18
2	49.83	0.68	3.48	6.32	0.16	13.92	23.47	0.30	0.03	0.31	98.50

Table 26. Sample M2-1A wt% of major oxides. FeO* indicates total Fe is reported as FeO

Crystal	SiO_2	TiO_2	Al_2O_3	FeO*	MnO	MgO	CaO	Na_2O	K_2O	Cr_2O_3	Total wt%
1	50.24	0.49	2.27	6.02	0.15	14.15	23.35	0.19	0.00	0.34	97.20
1	50.45	0.43	2.23	5.60	0.15	14.52	22.88	0.26	0.00	0.87	97.39
1	52.45	0.27	1.42	6.27	0.21	15.92	21.08	0.13	0.00	0.40	98.15
1	50.92	0.53	2.47	6.26	0.16	14.16	22.88	0.27	0.00	0.29	97.93
1	52.08	0.35	1.30	5.81	0.15	14.71	23.03	0.17	0.02	0.21	97.84
1	52.09	0.36	1.20	6.13	0.15	14.70	22.32	0.18	0.01	0.16	97.29
2	49.63	0.94	3.88	8.08	0.17	12.64	22.51	0.29	0.02	0.00	98.17
2	51.59	0.44	2.15	5.74	0.14	14.33	23.09	0.22	0.00	0.42	98.12
2	51.88	0.30	1.09	6.06	0.19	15.37	22.08	0.19	0.00	0.24	97.40
2	51.81	0.30	1.06	5.96	0.20	15.23	22.17	0.20	0.01	0.24	97.18
3	51.04	0.54	2.72	6.37	0.17	13.95	23.12	0.27	0.00	0.45	98.63
3	50.74	0.69	2.50	7.32	0.23	14.37	21.85	0.22	0.00	0.00	97.93
3	51.21	0.48	1.99	5.71	0.15	14.32	23.11	0.23	0.00	0.40	97.61
4	50.54	0.51	2.62	6.12	0.17	13.98	23.23	0.22	0.03	0.40	97.82
4	51.88	0.31	1.23	5.42	0.13	15.42	22.74	0.18	0.00	0.44	97.74
4	52.17	0.24	1.39	5.01	0.18	15.44	22.88	0.24	0.01	0.62	98.18
4	50.76	0.46	2.08	5.86	0.16	14.27	23.33	0.28	0.00	0.43	97.61
4	50.67	0.51	1.93	5.83	0.20	14.18	23.52	0.19	0.00	0.43	97.46

Table 27. Sample M3-3 wt% of major oxides. FeO* indicates total Fe is reported as FeO

Crystal	SiO_2	TiO_2	Al_2O_3	FeO*	MnO	MgO	CaO	Na_2O	K_2O	Cr_2O_3	Total wt%
1	53.10	0.35	1.67	6.43	0.20	15.45	22.69	0.18	0.01	0.17	100.23
1	53.85	0.38	1.46	6.63	0.16	15.31	22.86	0.20	0.00	0.18	101.03
1	53.41	0.40	1.37	6.48	0.20	15.41	22.59	0.17	0.01	0.13	100.17
1	53.45	0.40	1.34	6.62	0.21	15.38	22.62	0.20	0.00	0.15	100.37
1	53.60	0.40	1.29	6.42	0.18	15.43	22.84	0.17	0.02	0.18	100.51
1	53.13	0.41	1.40	6.16	0.19	15.73	23.11	0.18	0.01	0.28	100.59
2	52.09	0.42	1.77	6.79	0.21	15.13	22.90	0.21	0.00	0.01	99.53
2	52.34	0.42	1.54	6.34	0.18	15.10	22.96	0.21	0.00	0.18	99.28
2	52.60	0.39	1.46	6.17	0.15	15.46	23.38	0.14	0.01	0.19	99.93
2	52.51	0.40	1.68	5.47	0.20	15.08	23.47	0.22	0.01	0.32	99.34
2	52.86	0.36	1.50	5.80	0.19	15.56	23.11	0.21	0.01	0.22	99.83
2	51.70	0.50	1.91	7.32	0.16	15.23	21.96	0.22	0.01	0.10	99.11
2	50.12	0.67	3.22	7.23	0.19	13.37	22.34	0.28	0.01	0.11	97.53
3	50.39	0.54	2.09	7.92	0.23	14.54	21.18	0.16	0.00	0.00	97.04
3	51.18	0.53	2.29	7.79	0.24	14.64	21.53	0.15	0.00	0.02	98.36
3	50.66	0.49	1.82	6.98	0.20	14.67	22.23	0.20	0.01	0.07	97.33

Table 28. Sample SO-18173 wt% of major oxides. FeO* indicates total Fe is reported as FeO

Crystal	SiO_2	TiO_2	Al_2O_3	FeO*	MnO	MgO	CaO	Na_2O	K_2O	Cr_2O_3	Total wt%
1	49.19	0.00	3.69	9.30	0.30	12.03	20.07	0.30	0.02	0.04	94.94
1	47.03	0.02	5.09	9.90	0.24	11.27	20.08	0.30	0.00	0.01	93.94
1	47.53	0.01	4.78	8.52	0.14	11.68	21.24	0.27	0.00	0.02	94.18
1	49.60	0.01	3.41	7.39	0.19	12.60	21.59	0.26	0.01	0.17	95.24
1	48.84	0.00	3.35	7.52	0.21	12.51	21.55	0.26	0.00	0.14	94.38
1	50.75	0.00	3.30	7.35	0.13	12.65	21.74	0.25	0.01	0.06	96.23
1	49.35	0.00	4.14	8.45	0.16	11.82	21.16	0.27	0.00	0.00	95.34
2	50.23	0.03	3.25	7.70	0.19	12.56	21.38	0.23	0.00	0.13	95.70
2	50.42	0.00	3.05	7.24	0.18	12.74	21.50	0.24	0.01	0.24	95.62
2	49.36	0.00	4.09	7.96	0.24	12.10	21.13	0.29	0.00	0.08	95.25
3	52.15	0.00	2.16	7.32	0.21	12.97	20.85	0.18	0.00	0.00	95.84
3	52.22	0.00	2.12	7.42	0.22	13.21	20.80	0.18	0.00	0.00	96.17
3	52.19	0.00	2.40	5.91	0.15	13.23	21.76	0.22	0.00	0.53	96.38
3	51.73	0.00	2.40	6.00	0.14	13.62	21.95	0.29	0.00	0.56	96.70
3	51.31	0.00	2.18	5.73	0.13	13.11	22.40	0.24	0.00	0.43	95.52
3	51.80	0.02	2.23	5.76	0.16	13.13	22.43	0.22	0.01	0.43	96.18
4	50.61	0.00	1.40	5.56	0.15	13.84	21.94	0.24	0.00	0.32	94.05
4	50.22	0.00	2.02	5.57	0.16	14.17	20.41	0.40	0.00	0.82	93.77
4	52.82	0.00	1.48	5.65	0.19	14.16	21.78	0.18	0.02	0.30	96.59
4	51.96	0.03	1.66	6.50	0.13	13.58	21.02	0.17	0.01	0.10	95.16
4	50.81	0.03	2.59	6.22	0.16	12.89	21.77	0.26	0.00	0.30	95.02
4	51.53	0.03	2.05	5.52	0.14	13.56	22.13	0.22	0.00	0.44	95.62

Table 29. Sample SO-18176 B wt% of major oxides. FeO* indicates total Fe is reported as FeO

Crystal	SiO_2	TiO_2	Al_2O_3	FeO*	MnO	MgO	CaO	Na_2O	K_2O	Cr_2O_3	Total wt%
1	50.75	0.00	1.63	5.55	0.10	14.65	21.95	0.28	0.01	0.63	95.55
1	49.88	0.00	1.54	7.43	0.20	14.13	20.65	0.21	0.00	0.03	94.08
1	50.20	0.00	1.61	5.74	0.13	14.29	21.71	0.26	0.01	0.62	94.57
1	48.24	0.01	2.50	7.31	0.19	13.04	21.69	0.30	0.01	0.10	93.38
1	48.49	0.00	2.31	6.64	0.15	13.84	21.23	0.30	0.00	0.31	93.27
1	49.72	0.02	2.12	6.15	0.15	14.21	21.51	0.27	0.02	0.25	94.42
2	50.64	0.00	2.24	6.52	0.11	13.21	21.91	0.26	0.01	0.19	95.07
2	48.78	0.03	3.05	8.22	0.17	12.72	21.20	0.29	0.01	0.07	94.54
2	49.19	0.03	2.59	6.79	0.13	13.95	21.57	0.31	0.00	0.35	94.92
2	48.89	0.00	2.58	7.59	0.20	13.41	21.32	0.29	0.00	0.15	94.43
2	48.80	0.02	2.57	7.16	0.15	13.49	21.76	0.28	0.03	0.13	94.40
2	49.58	0.00	2.10	5.91	0.13	14.20	21.98	0.27	0.00	0.56	94.73
3	50.63	0.00	1.37	6.17	0.18	14.71	21.26	0.25	0.04	0.51	95.11
3	51.57	0.00	0.98	5.36	0.17	15.33	21.54	0.21	0.02	0.38	95.57
3	50.90	0.01	1.21	6.56	0.18	14.92	21.05	0.19	0.03	0.10	95.15
3	51.28	0.01	1.13	6.18	0.18	15.10	21.00	0.16	0.00	0.27	95.31

Table 30. Sample SO-1747A wt% of major oxides. FeO* indicates total Fe is reported as FeO

Crystal	SiO_2	TiO_2	Al_2O_3	FeO*	MnO	MgO	CaO	Na_2O	K_2O	Cr_2O_3	Total wt%
1	51.07	0.00	3.06	5.98	0.14	13.85	21.82	0.33	0.00	0.64	96.90
1	51.11	0.00	2.84	6.05	0.16	13.63	21.76	0.31	0.01	0.24	96.11
1	51.71	0.00	2.28	5.96	0.13	14.13	22.09	0.17	0.04	0.14	96.65
1	50.85	0.01	3.07	6.09	0.13	13.77	21.51	0.33	0.00	0.61	96.38
2	51.93	0.00	1.64	6.00	0.17	14.36	21.77	0.20	0.00	0.20	96.27
2	52.45	0.02	1.37	5.11	0.18	14.68	22.20	0.22	0.00	0.46	96.69
2	51.85	0.00	1.49	5.78	0.10	14.47	22.00	0.22	0.01	0.17	96.08
2	51.70	0.00	1.61	5.99	0.17	14.55	21.41	0.21	0.03	0.24	95.90
3	51.46	0.03	1.90	5.67	0.15	14.55	21.37	0.24	0.01	0.41	95.78
3	51.34	0.00	2.02	6.18	0.19	14.10	20.87	0.29	0.01	0.40	95.41
3	50.51	0.00	2.18	6.01	0.20	13.97	20.69	0.32	0.00	0.43	94.31
3	49.91	0.01	2.75	5.96	0.16	13.49	21.27	0.29	0.02	0.42	94.28
3	48.78	0.00	3.56	6.77	0.14	13.17	20.90	0.38	0.00	0.21	93.90

Table 31. Sample 1601.2A wt% of major oxides. FeO* indicates total Fe is reported as FeO

Crystal	SiO_2	TiO_2	Al_2O_3	FeO*	MnO	MgO	CaO	Na_2O	K_2O	Cr_2O_3	Total wt%
1	52.50	0.00	1.32	4.06	0.10	16.27	21.64	0.20	0.02	0.43	96.53
1	51.53	0.00	1.31	4.26	0.12	17.06	21.40	0.32	0.00	0.36	96.36
1	52.86	0.00	1.33	4.17	0.12	16.43	21.46	0.17	0.00	0.41	96.95
1	52.71	0.02	1.50	4.15	0.11	16.48	21.57	0.20	0.00	0.64	97.38
2	48.43	0.00	4.19	8.55	0.19	11.78	20.23	0.28	0.00	0.06	93.72
2	49.74	0.00	2.96	6.41	0.16	12.94	20.48	0.31	0.00	0.13	93.13
2	51.25	0.02	1.82	7.14	0.18	14.60	18.53	0.15	0.00	0.20	93.89
3	49.80	0.00	3.68	8.23	0.20	13.35	20.74	0.32	0.00	0.03	96.35
3	50.12	0.00	3.70	6.29	0.14	14.17	21.52	0.22	0.00	0.19	96.35
3	52.09	0.00	2.07	4.47	0.12	15.41	21.86	0.18	0.00	0.69	96.90
3	52.04	0.04	2.21	5.07	0.17	15.07	21.52	0.22	0.00	0.16	96.50
3	50.38	0.00	3.49	6.24	0.19	14.84	20.77	0.24	0.00	0.17	96.32

APPENDIX II: CPX CHEMISTRY

Each site represents a single cpx crystal probed in each sample (Figures 44-66). Multiple points were analyzed in each crystal as indicated by the symbols on legends for the graphs.

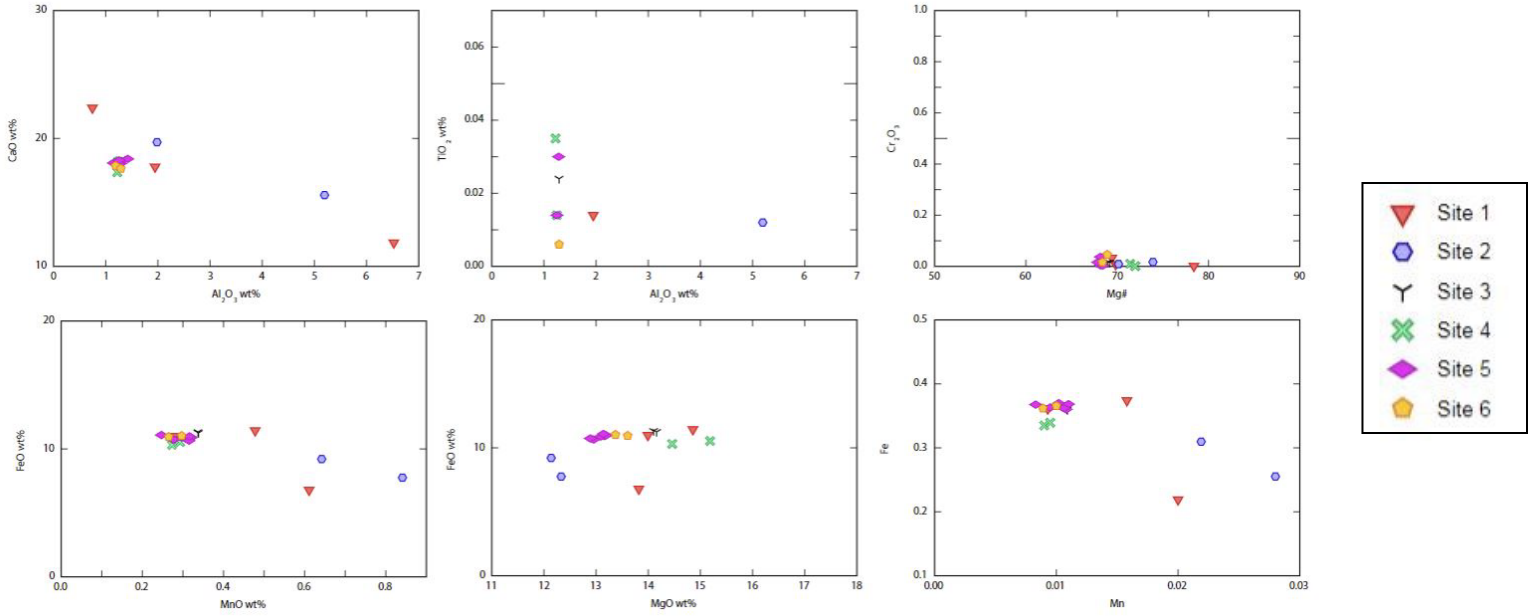

Figure 44. Sample KB43-16 from sill package 1 (Andrews).

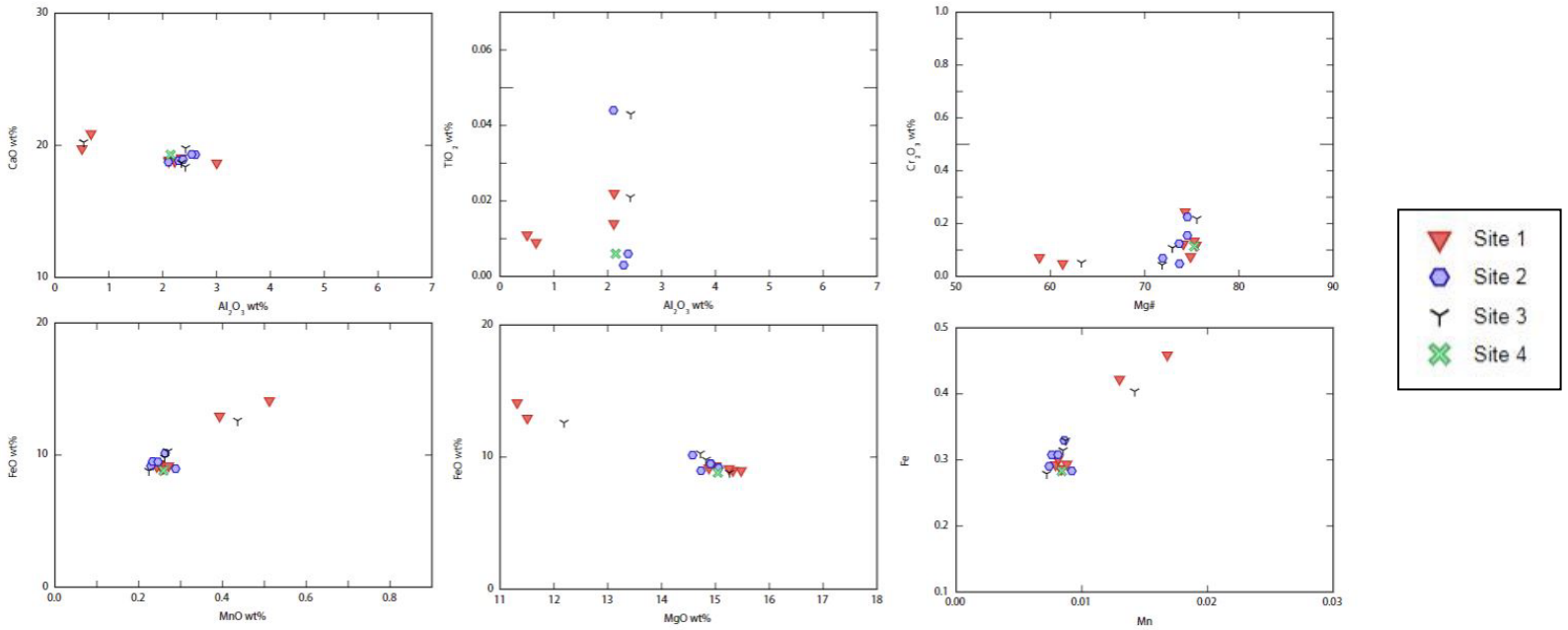

Figure 45. Sample PO7-16 from sill package 2 (Andrews).

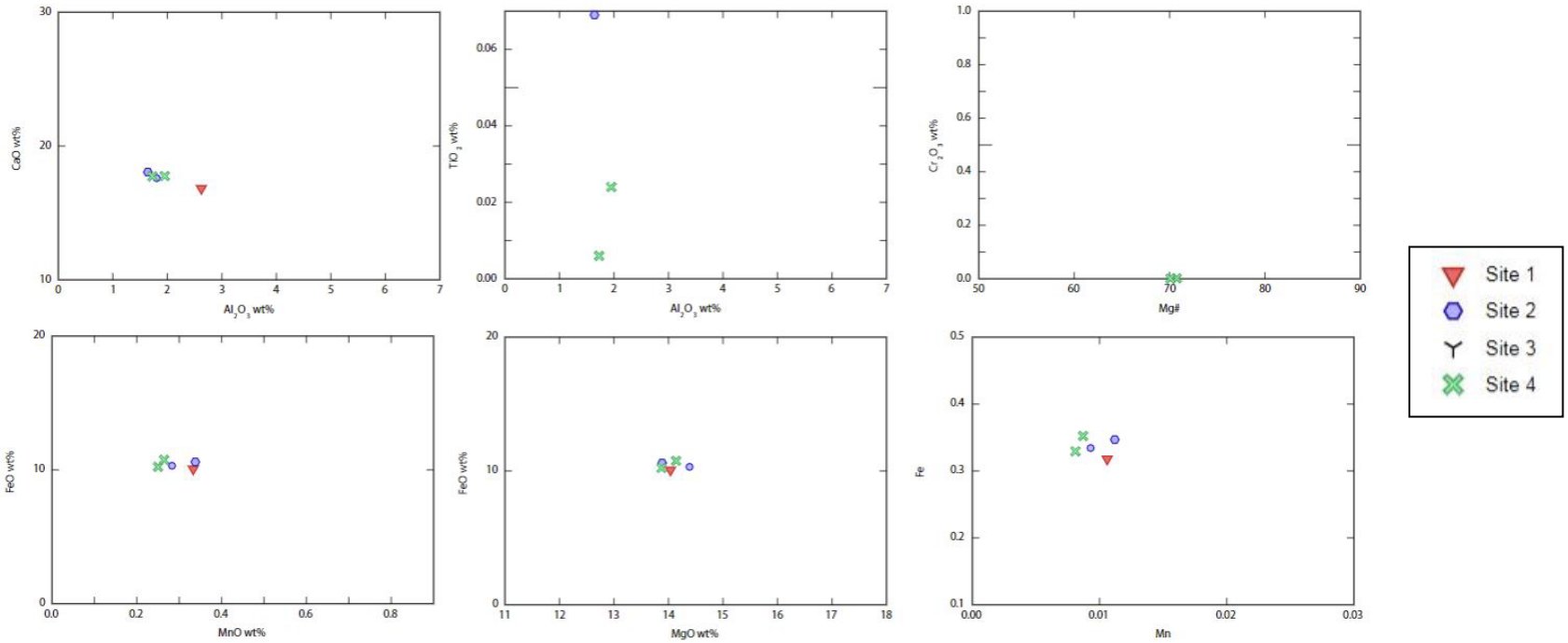

Figure 46. Sample G56-16 from sill package 3 (Andrews).

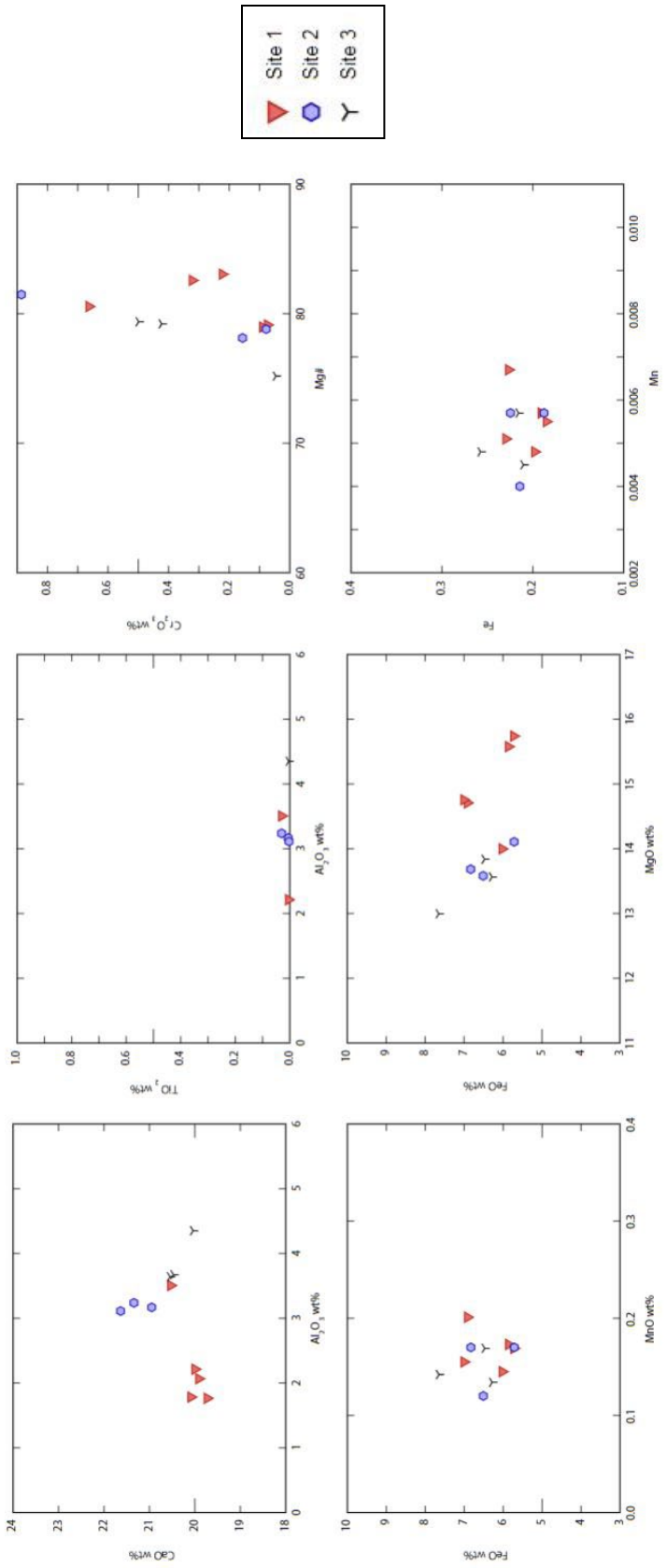

Figure 47. Sample M6-4 from a sill (Ohrmundt).

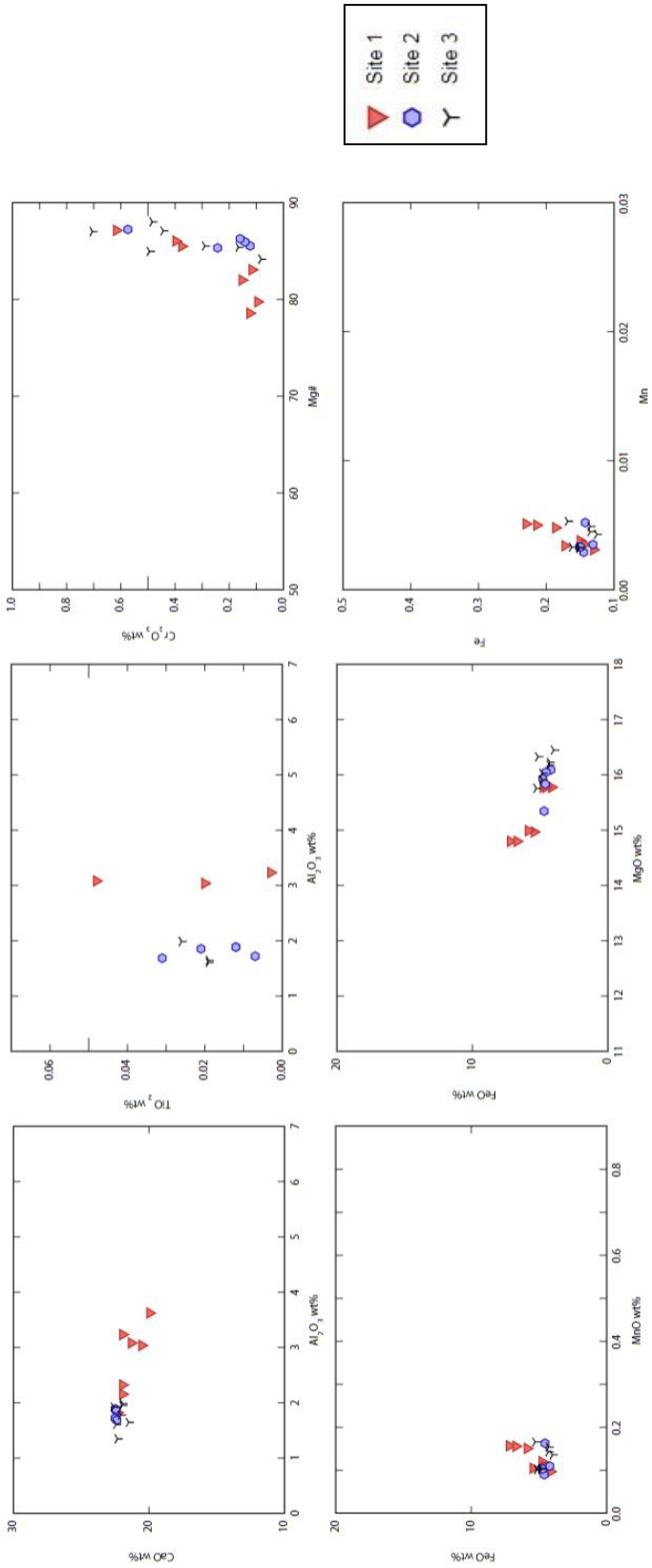

Figure 48. Sample VA 1603, agglutinate (Andrews).

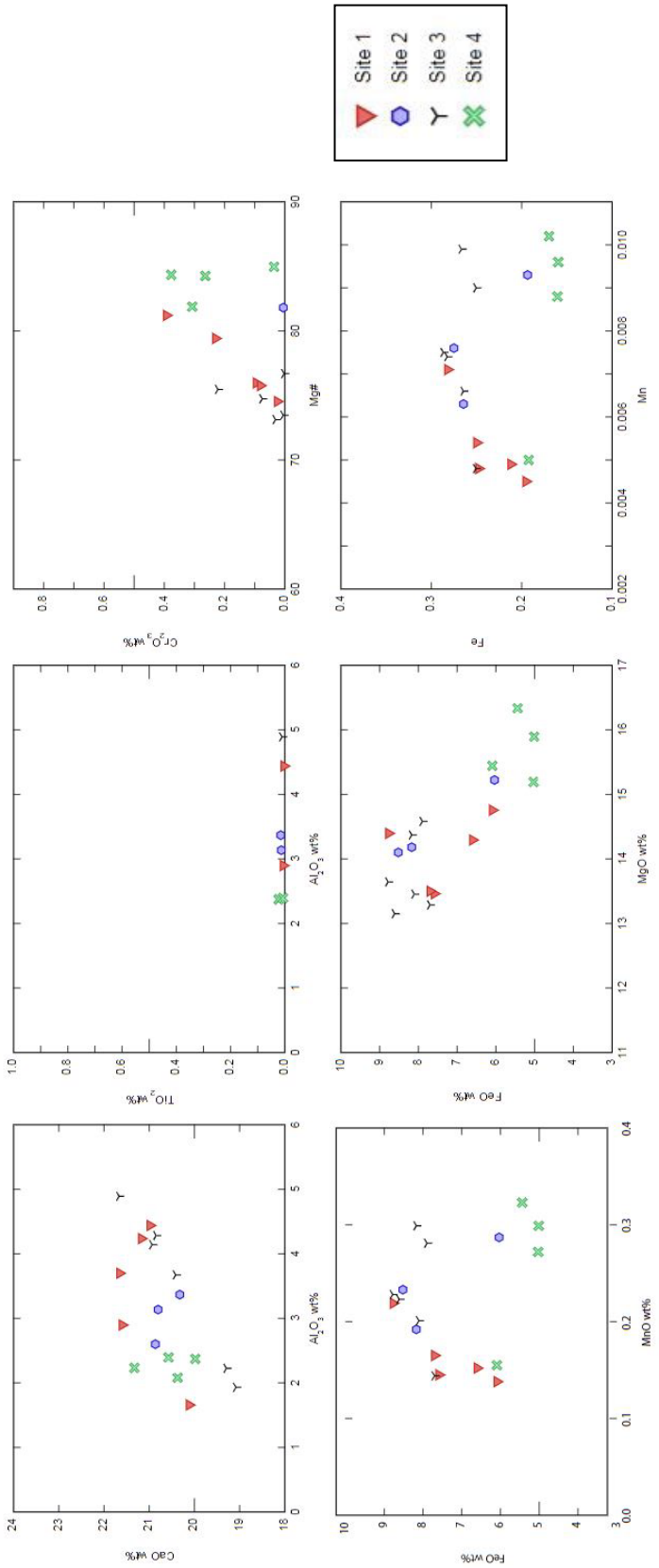

Figure 49. Sample SO-18126 A, agglutinate (Ohrmundt).

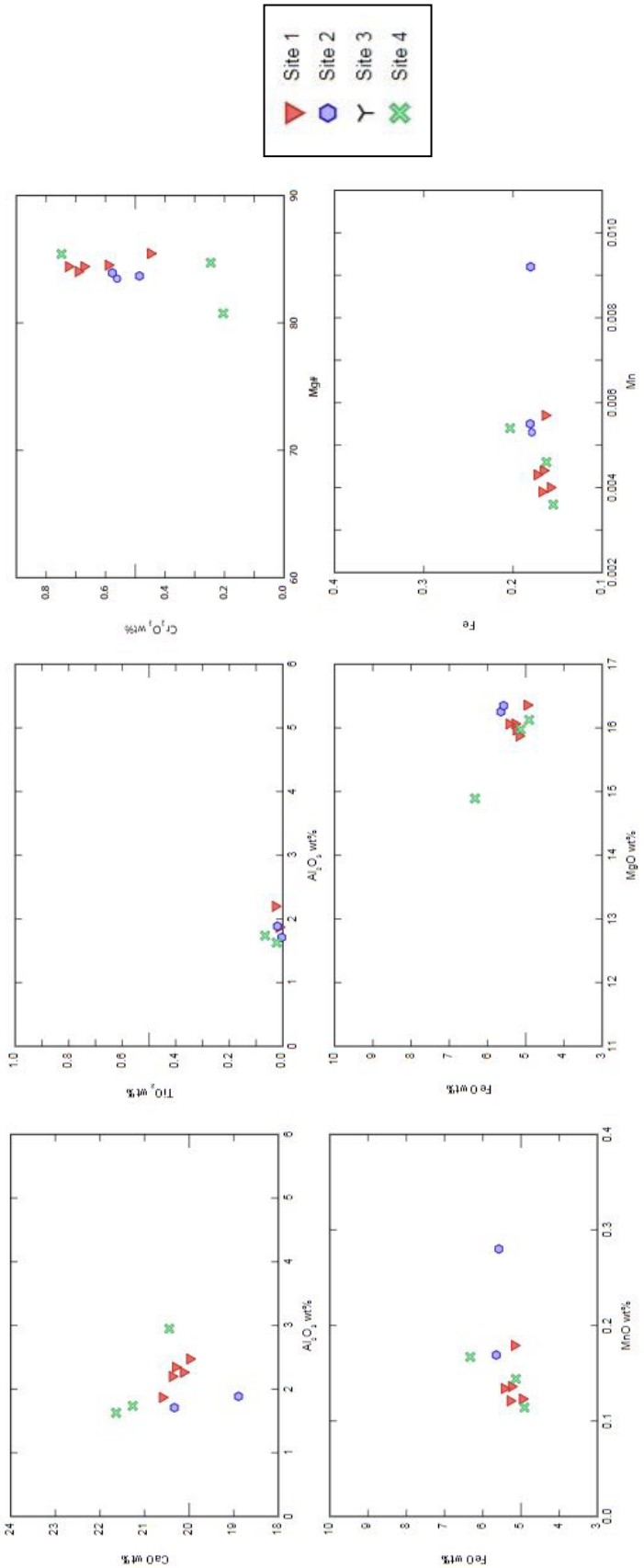

Figure 50. Sample SO-1767 C from agglutinate (Ohrmundt).

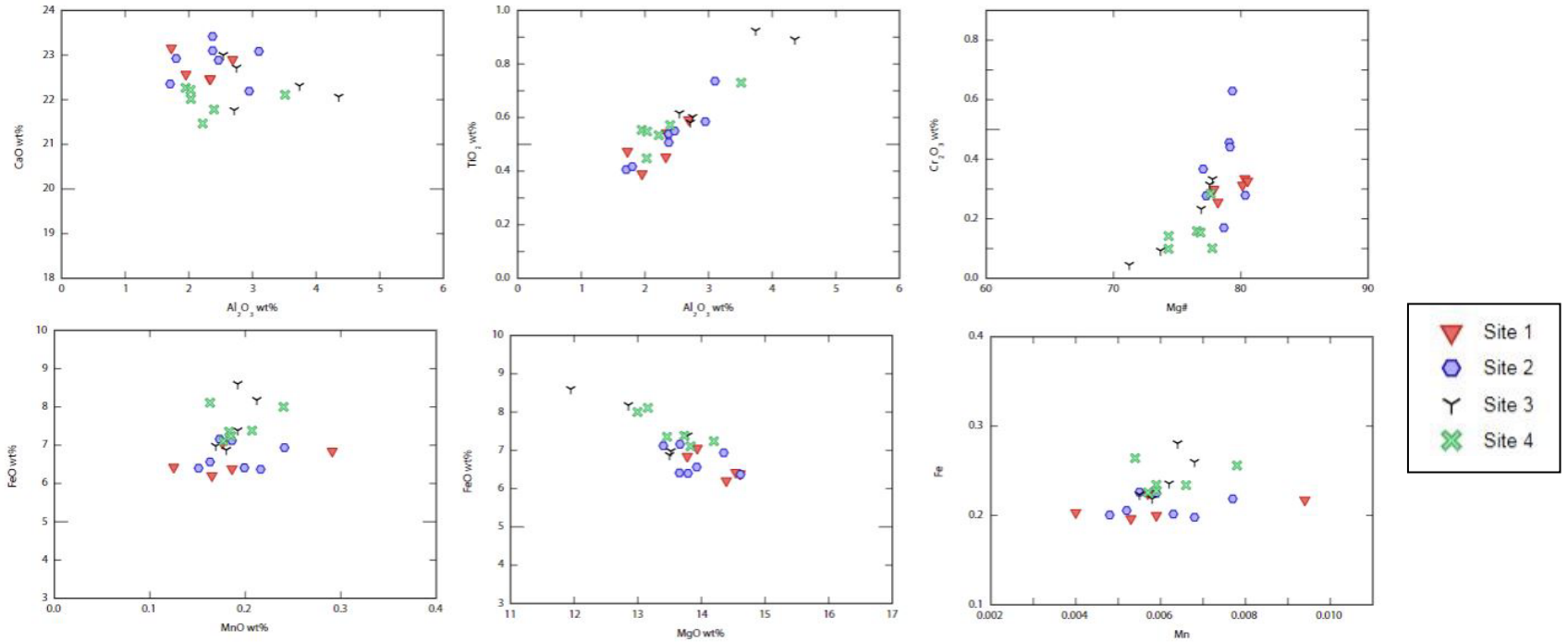

Figure 51. Sample M1-1A from agglutinate (Ohrmundt).

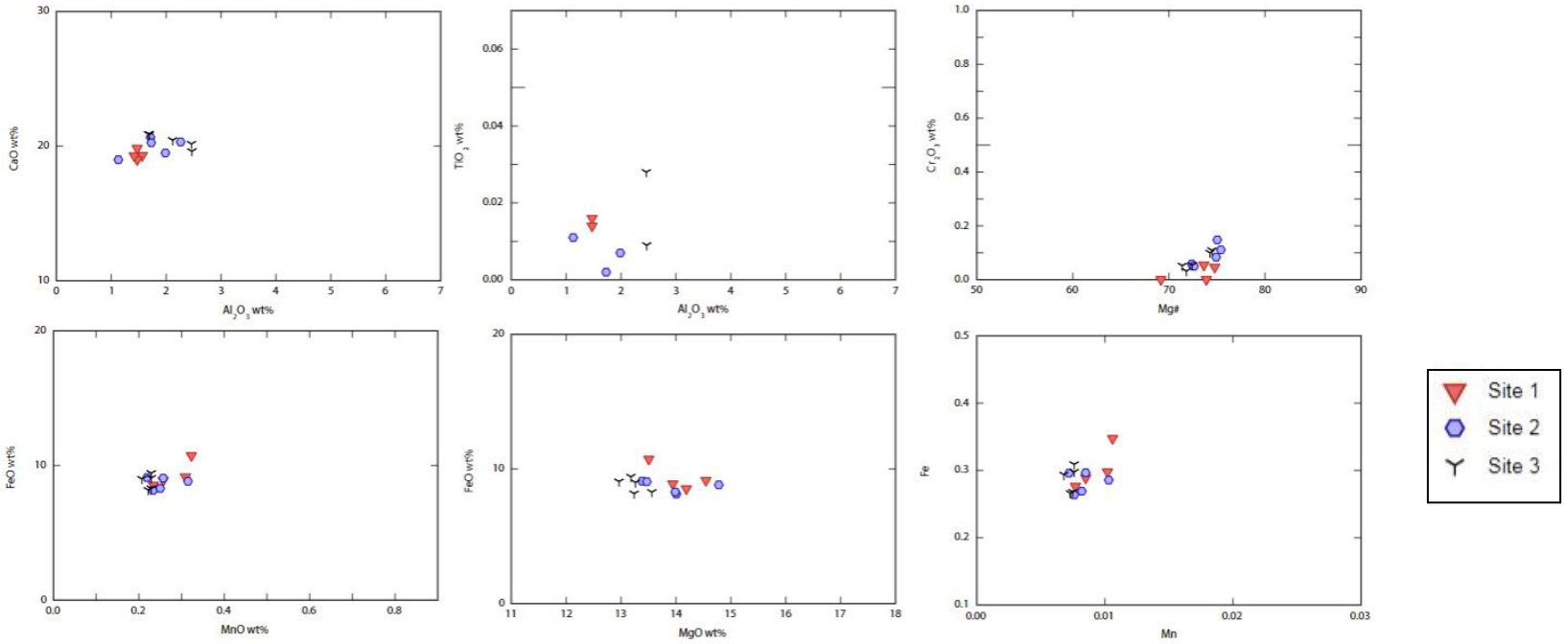

Figure 52. Sample VA 16105 from a hypabyssal intrusion (Andrews).

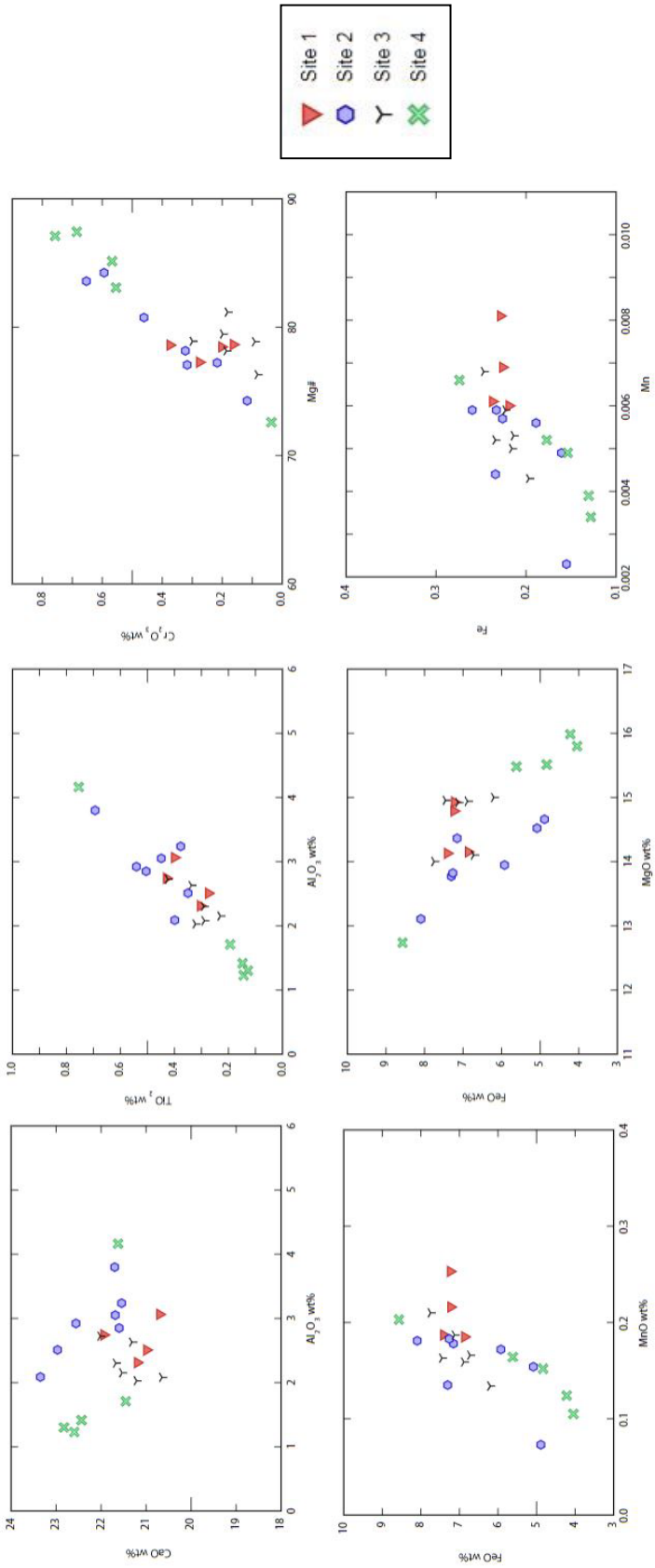

Figure 53. Sample SO-1716 D from a hypabyssal intrusion (Ohrmundt).

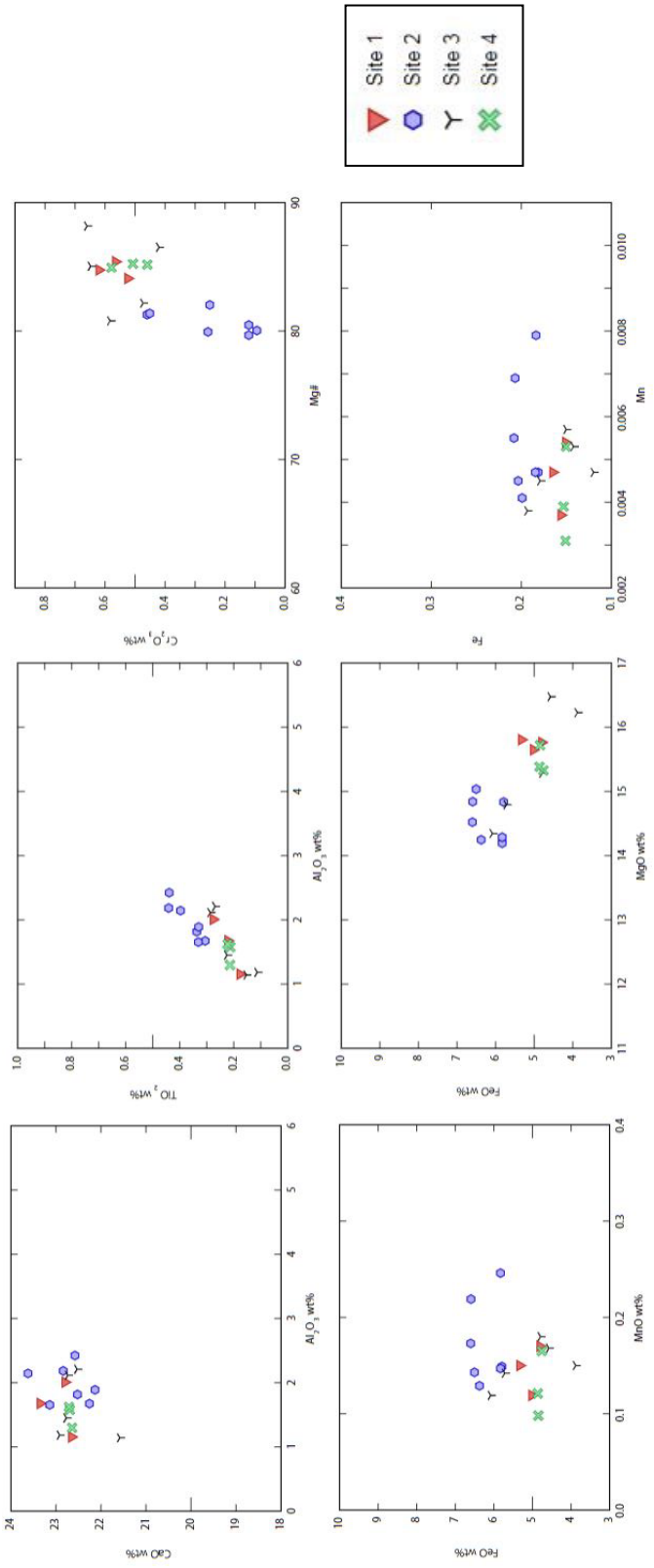

Figure 54. Sample SO-1763 G from a hypabyssal intrusion (Ohrmundt).

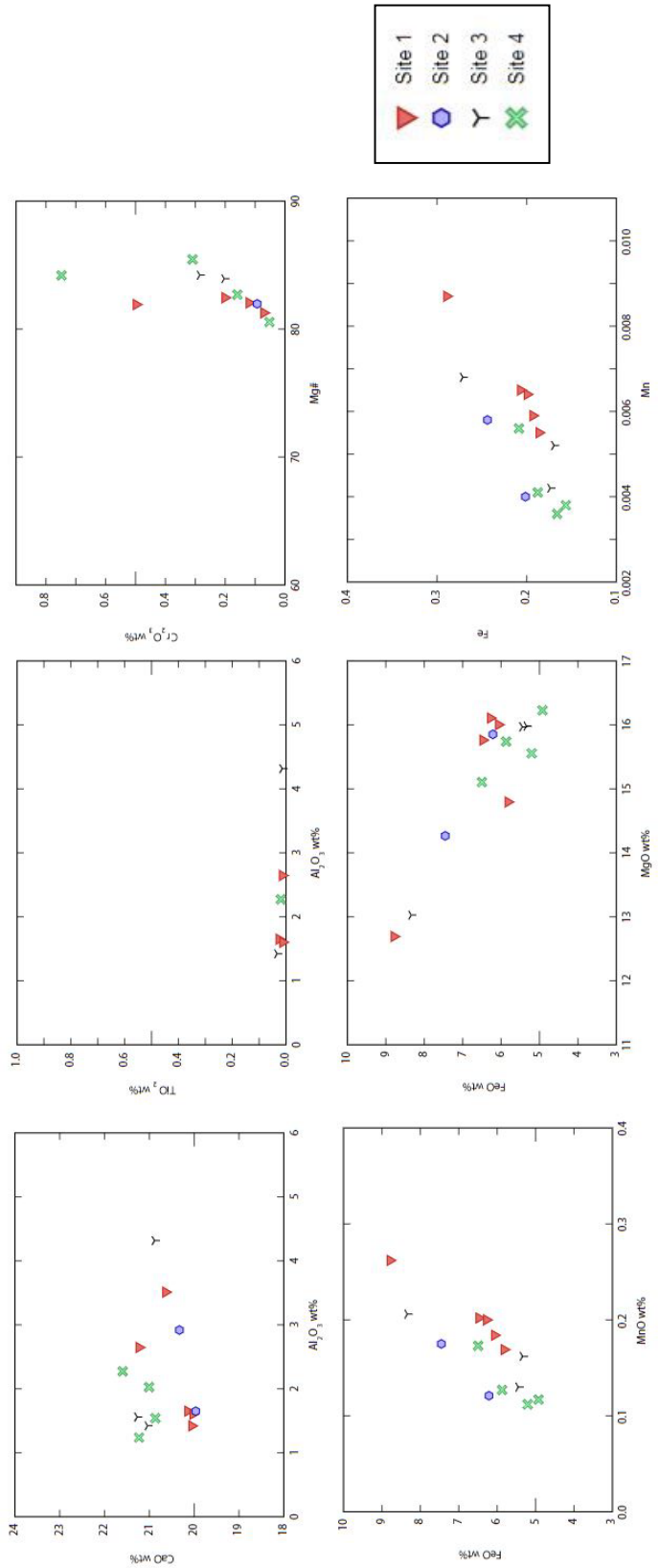

Figure 55. Sample M3-4 from a hypabyssal intrusion (Ohrmundt).

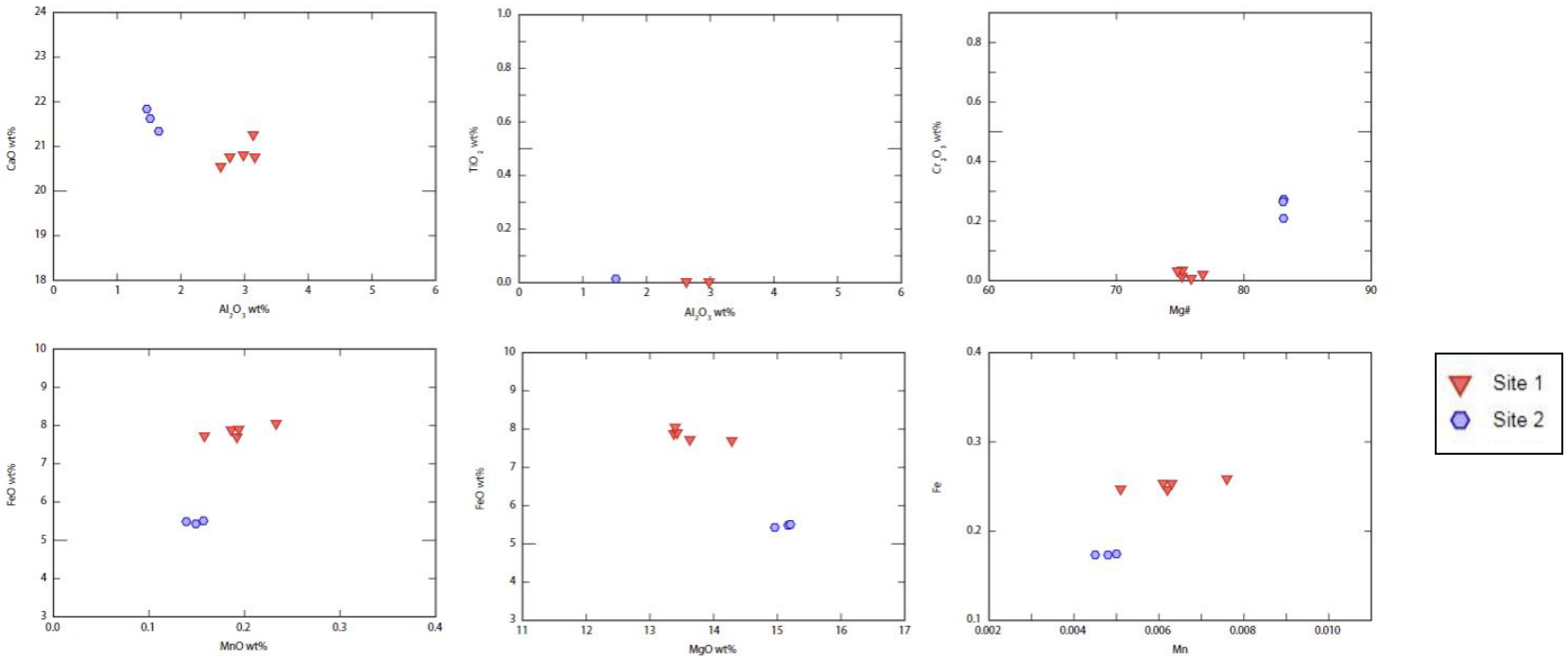

Figure 56. Sample SO-1888A from a hypabyssal intrusion (Ohrmundt).

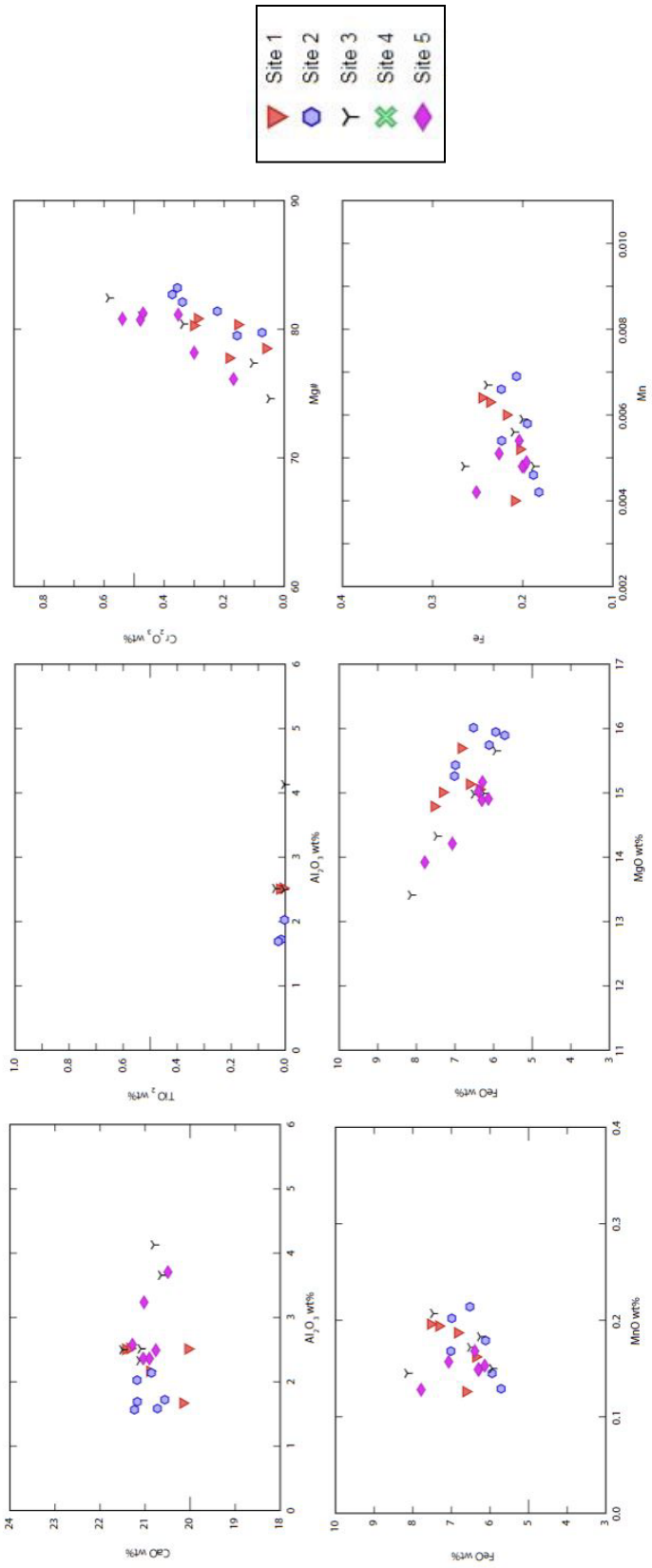

Figure 57. Sample SO-1894 from a hypabyssal intrusion (Ohrmundt).

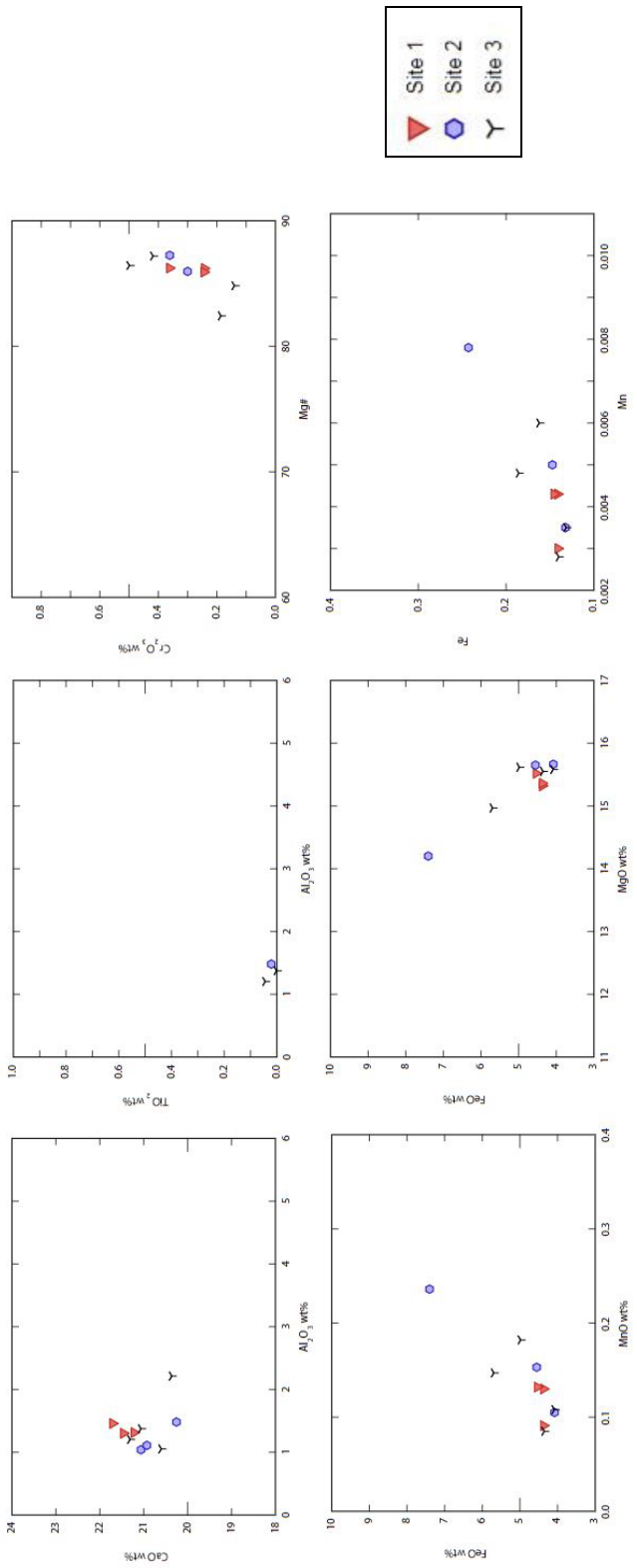

Figure 58. Sample SO-18166 from a hypabyssal intrusion (Ohrmundt).

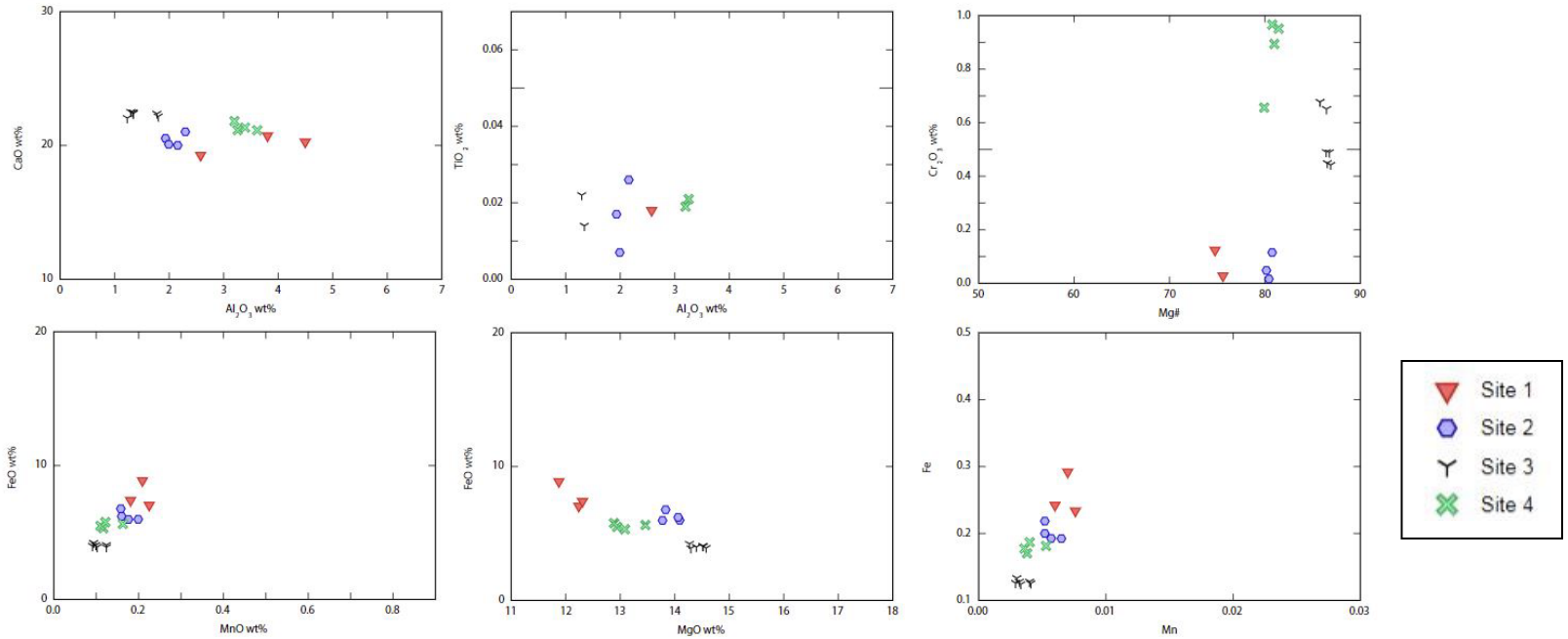

Figure 59. Sample MS6-7 from a pyroclastic bomb (Andrews).

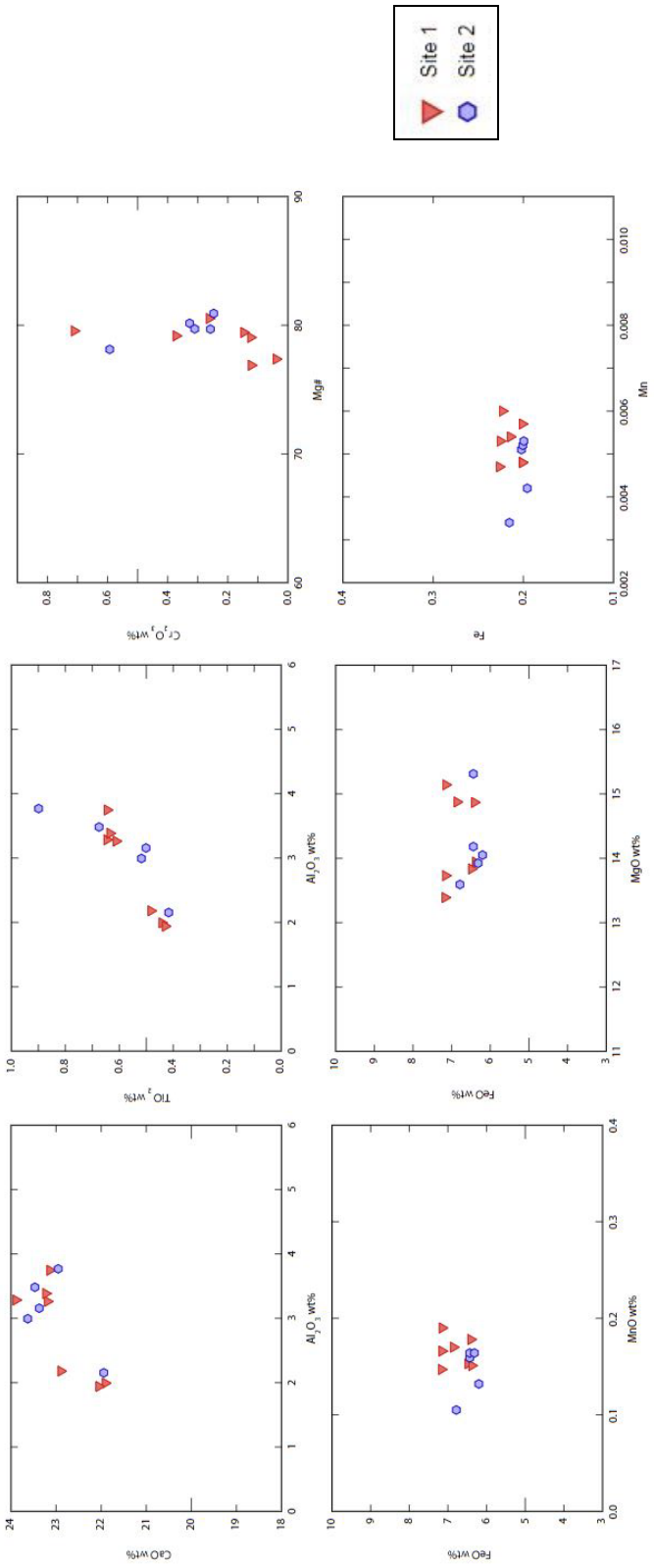

Figure 60. Sample M1-4B from a pyroclastic bomb (Ohrmundt).

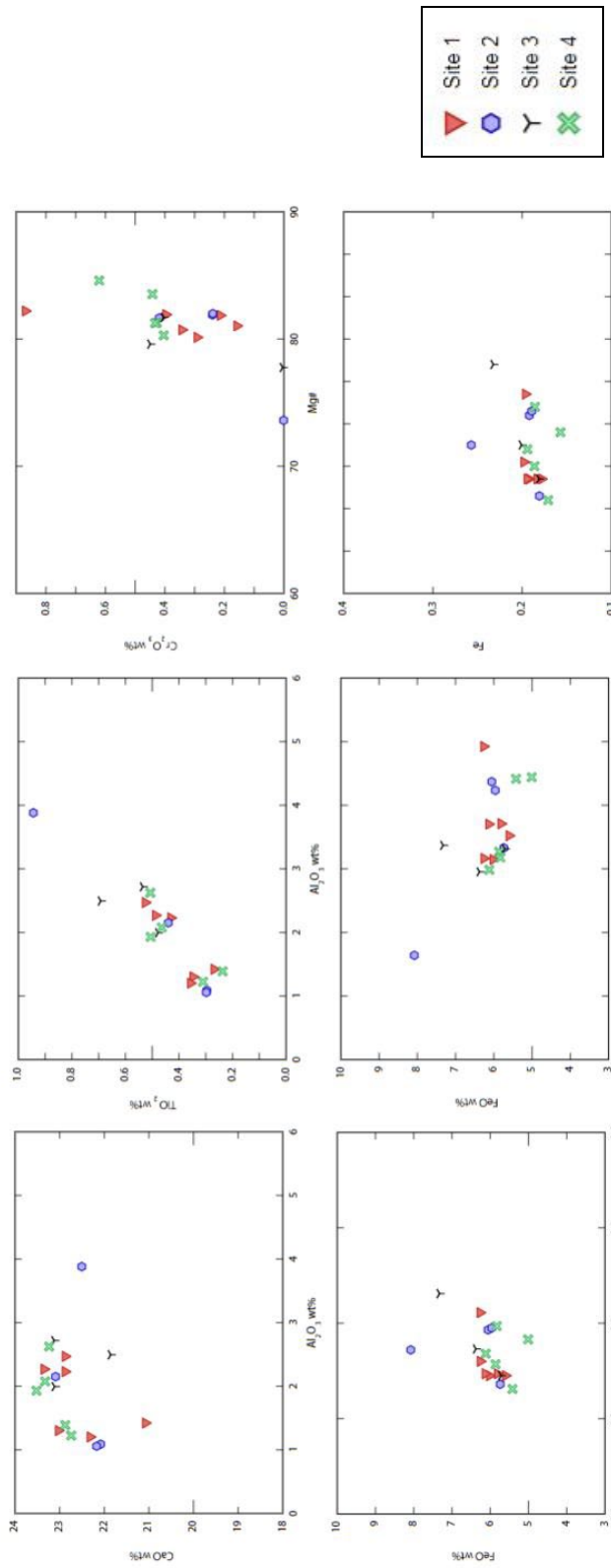

Figure 61. Sample M2-1A from a pyroclastic bomb (Ohrmundt).

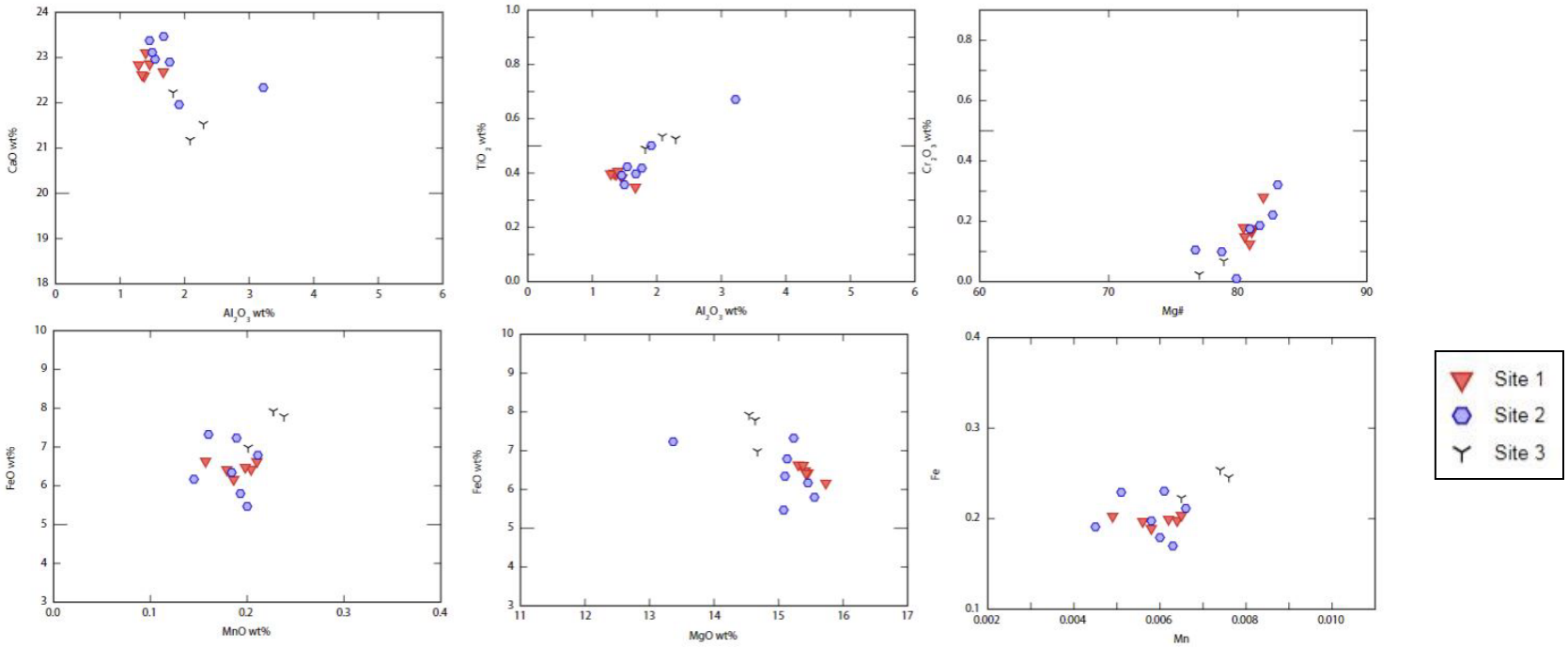

Figure 62. Sample M3-3 from a pyroclastic bomb (Ohrmundt).

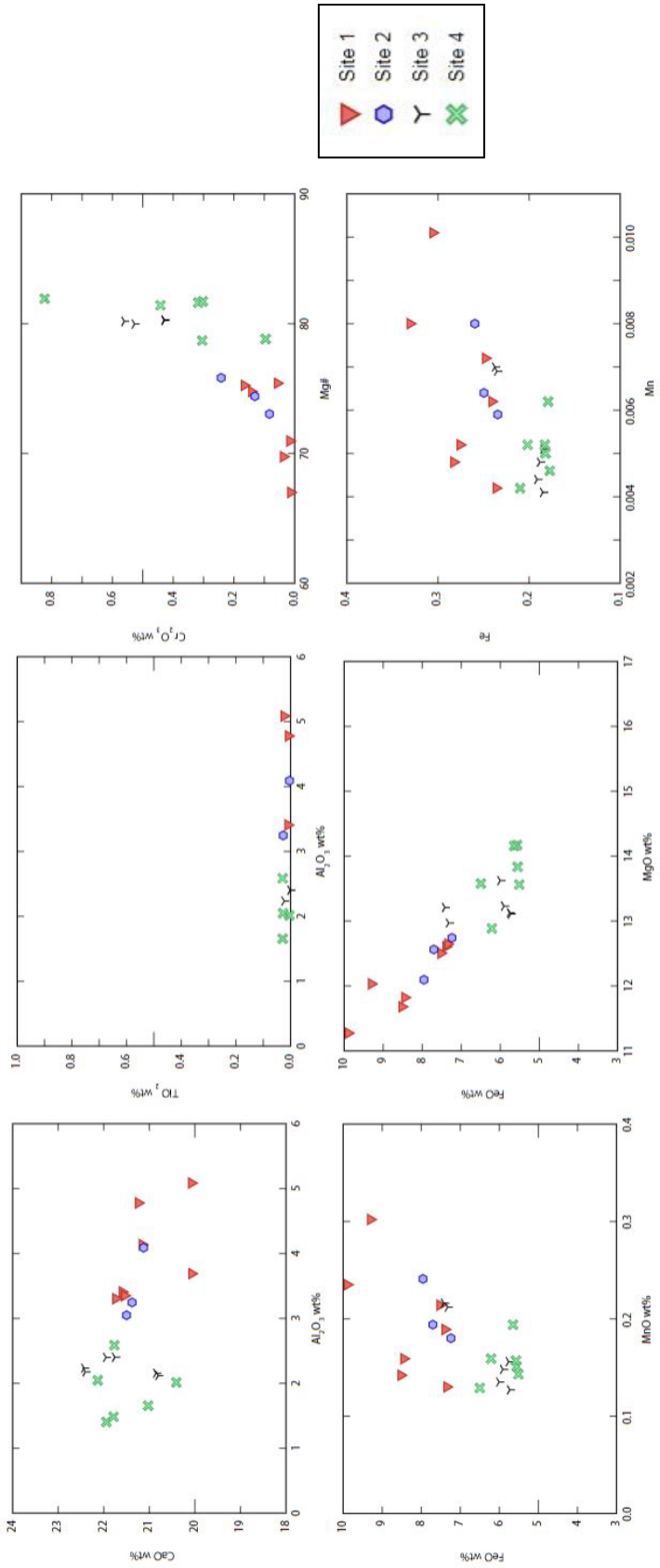

Figure 63. Sample SO-18173 from a pyroclastic bomb (Ohrmundt).

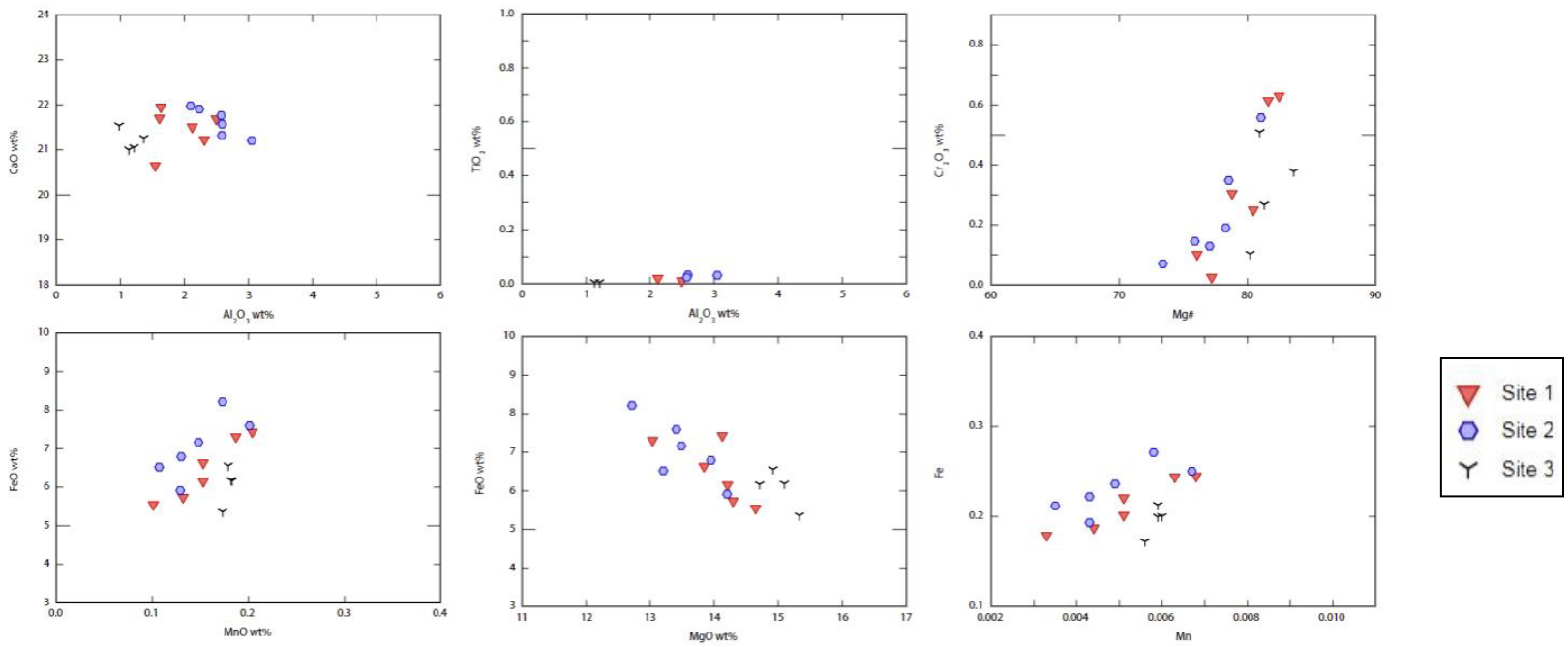

Figure 64. Sample SO-18176 B from a pyroclastic bomb (Ohrmundt).

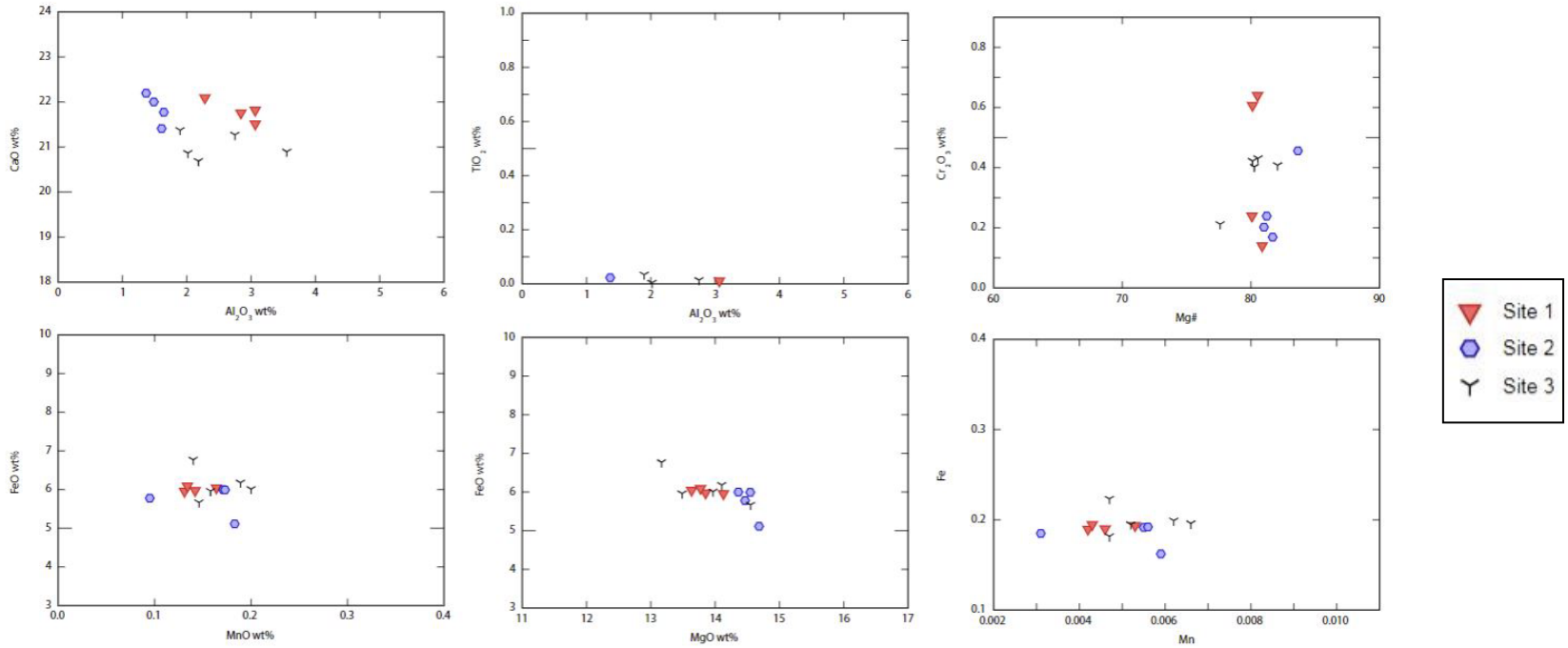

Figure 65. Sample SO-1747A from a pyroclastic bomb (Ohrmundt).

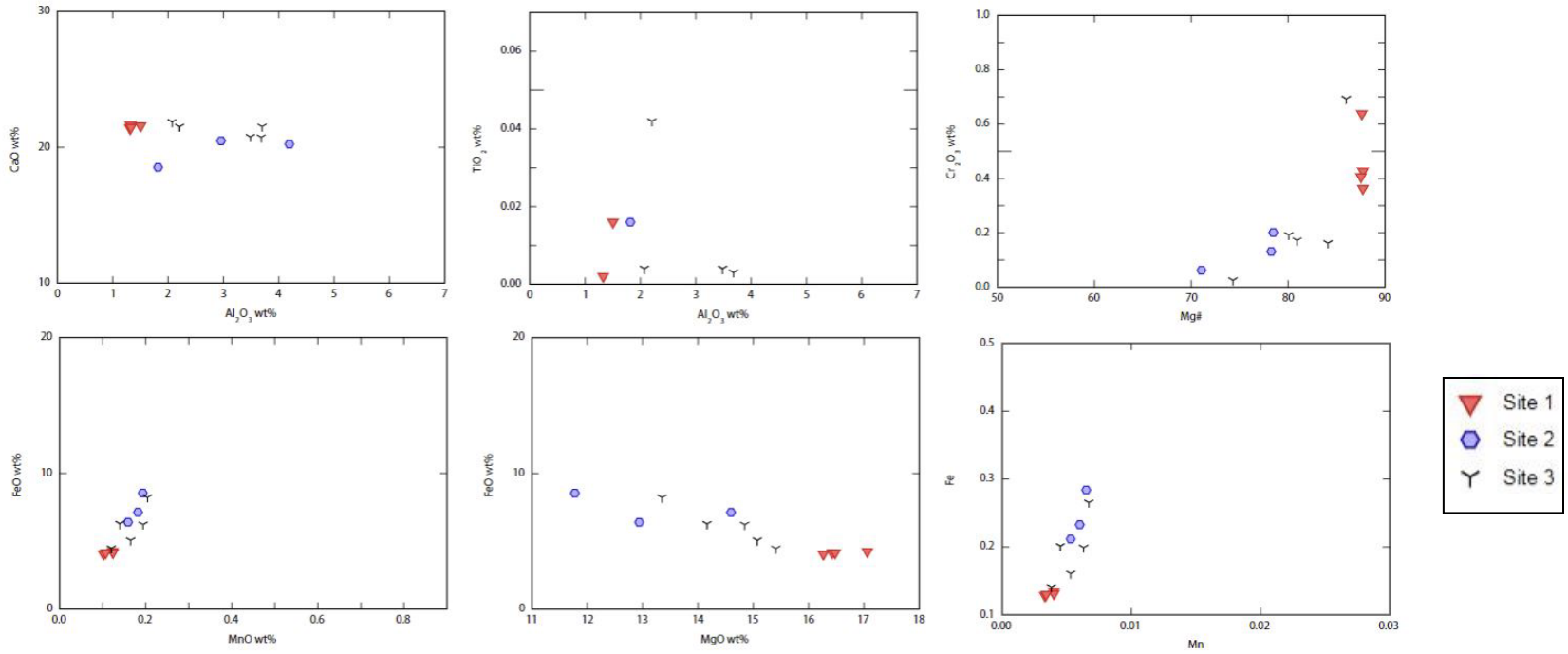

Figure 66. Sample 1601.2A from bedded lapillistone (Andrews).

APPENDIX III: CPX TEMPERATURES AND PRESSURES

Table 32. KB43-16 temperatures and pressures

Cpx crystal	Point on crystal	Temperature Wang et al. (2021)	Temperature Putirka (2008)	Pressure Wang et al. (2021)	Pressure Putirka (2008)
1	2	1228.47	1268.49	13.49	10.49
1	4	1110.04	1187.38	0.13	0.94
1	5	1149.95	1179.62	3.19	7.99
2	1	1237.94	1285.30	13.99	11.98
2	2	1209.48	1228.87	6.02	7.01
3	1	1151.12	1178.43	3.14	5.53
3	2	1147.12	1178.83	3.26	7.69
4	3	1155.94	1183.07	2.89	6.95
4	4	1165.07	1186.56	3.42	7.49
5	1	1130.89	1161.51	1.40	6.87
5	2	1127.58	1162.54	1.47	7.11
5	3	1138.61	1174.84	2.80	7.53
5	4	1143.96	1173.99	2.74	7.53
5	5	1145.72	1178.01	3.14	7.73
5	6	1150.85	1175.44	3.01	7.78
6	4	1156.67	1177.43	3.02	7.73
6	5	1166.73	1185.21	4.10	8.33

Table 33. PO7-16 temperatures and pressures

Cpx crystal	Point on crystal	Temperature Wang et al. (2021)	Temperature Putirka (2008)	Pressure Wang et al. (2021)	Pressure Putirka (2008)
1	1	1086.91	1136.29	1.37	7.79
1	2	1111.12	1152.67	2.29	2.25
1	3	1260.54	1265.10	11.03	3.26
1	4	1273.40	1274.10	12.03	3.13
1	5	1279.64	1273.71	12.13	4.98
1	7	1261.38	1263.65	11.05	3.76
1	8	1264.50	1266.62	11.63	3.51
2	1	1242.21	1252.04	9.32	5.44
2	2	1270.89	1266.94	11.31	4.18
2	3	1270.28	1271.39	12.40	2.84
2	4	1258.36	1261.81	11.42	3.10
2	5	1269.28	1276.73	13.77	1.96
3	1	1101.90	1141.50	0.26	7.69
3	3	1277.18	1276.58	12.21	2.42
3	4	1250.13	1253.05	10.43	4.55
3	5	1242.20	1245.02	9.99	5.40
4	5	1260.49	1265.73	10.99	3.18

Table 34. G56-16 temperatures and pressures

Cpx crystal	Point on crystal	Temperature Wang et al. (2021)	Temperature Putirka (2008)	Pressure Wang et al. (2021)	Pressure Putirka (2008)
1	2	1283.17	1248.55	10.01	10.14207
4	2	1150.55	1183.11	3.39	7.813208
5	1	1189.15	1199.71	4.73	8.103203
6	2	1229.79	1207.94	5.66	8.774168
6	3	1216.70	1199.76	5.33	11.40827

Table 35. M6-4 temperatures and pressures

Cpx crystal	Point on crystal	Temperature Wang et al. (2021)	Temperature Putirka (2008)	Pressure Wang et al. (2021)	Pressure Putirka (2008)
1	1	1211.06	1234.33	4.20	2.90
1	2	1187.43	1216.84	3.48	4.12
1	3	1184.94	1210.70	2.85	4.16
1	4	1214.59	1233.36	4.26	3.25
1	5	1208.50	1240.11	5.27	5.23
2	2	1194.79	1232.64	4.03	4.23
2	3	1192.61	1220.54	3.58	4.19
2	4	1179.67	1213.19	3.08	4.68
3	2	1187.11	1215.29	4.11	6.52
3	3	1189.00	1222.84	3.70	4.90
3	4	1198.59	1230.23	4.42	5.08

Table 36. VA 1603 temperatures and pressures

Cpx crystal	Point on crystal	Temperature Wang et al. (2021)	Temperature Putirka (2008)	Pressure Wang et al. (2021)	Pressure Putirka (2008)
1	1	1224.86	1245.16	5.04	3.24
1	2	1256.44	1258.60	5.33	1.02
1	3	1227.55	1250.48	4.97	1.88
1	4	1245.64	1257.97	5.66	1.74
1	5	1215.56	1239.42	4.92	4.05
1	6	1210.00	1235.33	5.57	5.92
1	7	1209.40	1233.68	5.04	4.93
2	1	1207.69	1232.76	3.07	0.37
2	2	1231.76	1247.90	4.65	0.80
2	3	1217.64	1241.16	4.00	0.81
2	4	1225.32	1249.88	4.38	0.67
2	5	1218.39	1245.40	4.34	0.64
3	1	1216.43	1239.72	3.86	0.83
3	2	1222.45	1244.86	4.49	1.65
3	3	1219.20	1249.24	4.37	1.24
3	4	1207.69	1239.45	3.03	-0.28
3	5	1198.49	1233.15	2.61	-0.30
3	6	1191.36	1219.63	1.85	1.32
3	7	1175.20	1210.03	0.94	0.61

Table 37. SO-18126 A temperatures and pressures

Cpx crystal	Point on crystal	Temperature Wang et al. (2021)	Temperature Putirka (2008)	Pressure Wang et al. (2021)	Pressure Putirka (2008)
1	1	1192.21	1222.41	3.14	3.55
1	2	1181.17	1213.67	3.65	5.96
1	3	1162.10	1193.72	2.55	5.23
1	4	1189.15	1221.60	4.64	6.44
1	5	1194.52	1224.84	3.88	4.65
2	1	1254.99	1280.80	9.17	5.10
2	2	1249.66	1248.73	6.12	4.41
2	3	1254.24	1280.69	8.87	4.56
2	4	1219.10	1255.14	5.90	2.66
3	1	1172.74	1206.84	3.77	6.34
3	2	1166.19	1197.58	2.38	5.51
3	5	1216.94	1249.70	6.32	4.38
4	1	1172.63	1207.25	2.97	6.17
4	2	1163.04	1200.68	3.21	6.76
4	3	1163.88	1198.07	3.05	6.54
4	4	1169.64	1205.99	3.26	6.23
4	5	1190.14	1218.06	4.88	5.97
4	6	1247.61	1235.15	6.36	6.81

Table 38. SO-1767 C temperatures and pressures

Cpx crystal	Point on crystal	Temperature Wang et al. (2021)	Temperature Putirka (2008)	Pressure Wang et al. (2021)	Pressure Putirka (2008)
1	1	1239.19	1262.37	6.85	4.01
1	2	1238.63	1261.95	6.75	4.12
1	3	1239.92	1260.97	6.69	4.06
1	5	1235.34	1258.03	6.49	4.26
1	7	1223.98	1247.03	4.87	2.50
2	3	1187.98	1217.22	2.07	2.25
2	5	1217.89	1251.37	6.02	4.18
3	3	1183.37	1215.44	1.83	1.99
4	1	1200.46	1228.63	2.97	1.36
4	2	1207.55	1234.83	3.53	2.30
4	3	1221.89	1247.48	6.27	4.99

Table 39. M1-1A temperatures and pressures

Cpx crystal	Point on crystal	Temperature Wang et al. (2021)	Temperature Putirka (2008)	Pressure Wang et al. (2021)	Pressure Putirka (2008)
1	1	1162.54	1193.51	1.28	4.38
1	2	1146.07	1175.01	0.14	4.96
1	3	1155.91	1182.72	-0.02	3.54
1	5	1140.88	1169.97	-1.43	2.85
1	7	1136.29	1175.32	0.11	5.14
2	1	1157.32	1188.91	1.89	6.05
2	2	1144.09	1174.29	0.59	6.20
2	3	1149.19	1184.36	0.73	3.97
2	4	1158.85	1191.51	0.94	3.48
2	5	1148.92	1181.71	0.21	4.32
2	6	1156.89	1189.25	1.16	4.61
2	7	1168.87	1193.98	1.72	4.83
3	1	1153.59	1183.54	1.15	5.56
3	2	1141.67	1174.75	2.03	8.64
3	3	1137.06	1165.19	-0.81	4.98
3	5	1160.29	1186.98	1.98	6.27
3	6	1123.09	1153.27	0.38	8.54
4	1	1140.96	1175.20	1.61	7.55
4	2	1153.49	1177.72	0.57	4.80
4	3	1163.23	1184.52	1.37	5.11
4	4	1169.32	1182.84	1.16	5.41
4	5	1143.50	1169.76	0.76	6.11
4	6	1168.59	1188.53	2.10	6.09

Table 40. VA 16105 temperatures and pressures

Cpx crystal	Point on crystal	Temperature Wang et al. (2021)	Temperature Putirka (2008)	Pressure Wang et al. (2021)	Pressure Putirka (2008)
1	1	1136.30	1175.30	2.38	7.01
1	2	1156.08	1191.90	2.84	5.88
1	3	1195.47	1205.26	4.15	6.37
1	4	1170.32	1201.99	3.42	5.33
2	1	1165.88	1192.57	2.52	5.48
2	2	1159.61	1195.78	3.23	6.13
2	3	1160.09	1197.35	2.45	4.62
2	4	1171.89	1204.66	4.31	6.48
2	5	1162.88	1200.21	2.95	6.30
3	1	1164.31	1200.47	4.18	7.04
3	2	1165.52	1199.68	3.68	6.45
3	3	1175.94	1204.13	3.41	4.90
3	4	1162.97	1201.34	3.11	4.81
3	5	1152.03	1190.53	2.71	5.87

Table 41. SO-1716 D temperatures and pressures

Cpx crystal	Point on crystal	Temperature Wang et al. (2021)	Temperature Putirka (2008)	Pressure Wang et al. (2021)	Pressure Putirka (2008)
1	3	1182.30	1210.71	3.51	5.46
1	4	1163.14	1197.68	2.17	5.07
1	5	1158.73	1189.01	1.23	5.21
1	6	1174.35	1204.71	3.50	6.59
2	1	1163.26	1190.84	1.95	6.10
2	2	1170.30	1200.40	2.56	5.97
2	3	1153.52	1183.83	1.27	5.88
2	4	1143.54	1174.22	1.43	7.70
2	6	1167.11	1194.49	-0.08	2.27
2	7	1173.19	1207.99	1.46	3.10
2	8	1161.27	1194.38	1.27	4.82
3	1	1194.01	1205.33	3.18	5.59
3	2	1197.30	1207.55	3.01	5.04
3	3	1163.68	1193.85	1.64	5.09
3	4	1178.03	1206.96	2.92	4.65
3	5	1163.47	1195.35	2.60	5.92
3	6	1185.70	1209.65	2.59	4.19
4	1	1069.79	1146.62	-1.28	3.29
4	2	1193.77	1220.64	1.44	-0.70
4	3	1137.15	1188.46	-0.77	-0.18
4	4	1151.14	1190.23	-1.33	-0.95
4	5	1159.52	1198.50	-1.21	-1.95

Table 42. SO-1763 G temperatures and pressures

Cpx crystal	Point on crystal	Temperature Wang et al. (2021)	Temperature Putirka (2008)	Pressure Wang et al. (2021)	Pressure Putirka (2008)
1	2	1166.99	1197.73	0.16	2.21
1	4	1155.90	1187.48	-1.40	0.81
1	5	1162.67	1198.46	-0.37	0.41
2	1	1159.08	1185.20	0.12	3.22
2	2	1162.13	1190.57	0.77	3.30
2	3	1145.58	1175.22	-0.62	3.71
2	4	1162.68	1192.74	0.36	2.29
2	5	1143.71	1177.27	-1.18	2.73
2	6	1188.76	1200.80	2.07	4.72
2	7	1206.40	1219.23	3.52	4.25
3	2	1242.96	1241.53	4.22	2.01
3	4	1173.77	1204.95	1.52	3.03
3	5	1164.04	1195.47	0.80	3.41
3	6	1226.48	1244.86	3.83	0.14
3	7	1185.83	1217.64	1.97	1.57
4	2	1192.31	1217.04	1.85	1.55
4	3	1179.62	1212.76	1.40	1.08
4	4	1179.53	1209.99	1.14	1.54

Table 43. M3-4 temperatures and pressures

Cpx crystal	Point on crystal	Temperature Wang et al. (2021)	Temperature Putirka (2008)	Pressure Wang et al. (2021)	Pressure Putirka (2008)
1	1	1163.08	1200.36	3.51	6.79
1	3	1194.06	1221.51	3.50	3.42
1	4	1230.33	1232.09	4.21	3.34
1	5	1210.40	1226.68	3.79	3.32
1	6	1202.85	1233.11	4.12	3.54
2	1	1180.04	1209.57	3.10	4.98
2	3	1194.28	1215.72	2.54	2.79
3	1	1170.01	1206.24	3.56	6.70
3	3	1211.44	1229.63	3.32	1.80
3	4	1191.44	1218.91	2.11	1.37
4	1	1185.60	1214.66	2.69	3.05
4	2	1201.81	1221.99	2.89	2.13
4	3	1213.49	1234.57	3.41	0.91
4	4	1187.49	1218.61	1.81	2.06

Table 44. SO-1888A temperatures and pressures

Cpx crystal	Point on crystal	Temperature Wang et al. (2021)	Temperature Putirka (2008)	Pressure Wang et al. (2021)	Pressure Putirka (2008)
1	1	1188.21	1219.12	4.38	5.31
1	2	1200.65	1231.25	6.12	5.96
1	3	1200.77	1235.08	6.51	6.55
1	4	1195.41	1226.05	5.25	5.81
1	5	1190.73	1228.23	5.90	6.38
2	1	1227.68	1241.95	4.88	2.21
2	3	1225.73	1244.44	5.21	2.35
2	4	1243.79	1251.94	6.04	3.01

Table 45. SO-1894 temperatures and pressures

Cpx crystal	Point on crystal	Temperature Wang et al. (2021)	Temperature Putirka (2008)	Pressure Wang et al. (2021)	Pressure Putirka (2008)
1	1	1188.42	1216.13	3.13	3.64
1	2	1152.70	1184.99	0.05	3.35
1	3	1169.31	1200.50	2.06	4.57
1	5	1184.23	1214.97	2.58	3.40
1	6	1193.92	1220.49	3.35	3.82
2	1	1178.23	1206.07	2.11	3.60
2	2	1170.10	1203.00	0.88	2.26
2	3	1172.11	1202.34	1.76	3.32
2	4	1166.90	1199.54	0.85	2.39
2	5	1182.33	1211.16	1.53	1.97
2	6	1179.63	1208.74	1.36	1.92
3	1	1191.23	1223.33	4.53	5.71
3	2	1176.69	1208.39	3.56	6.40
3	4	1172.12	1205.28	1.68	3.50
3	5	1188.50	1221.91	3.24	3.47
3	6	1186.07	1218.36	2.39	2.95
4	1	1194.67	1225.58	4.43	5.15
4	2	1216.52	1232.46	4.40	3.78
4	3	1196.54	1228.18	3.97	3.95
4	4	1199.80	1229.65	4.22	4.12
4	5	1215.43	1233.99	4.49	3.78
4	6	1189.25	1217.79	4.24	6.04

Table 46. SO-18166 temperatures and pressures

Cpx crystal	Point on crystal	Temperature Wang et al. (2021)	Temperature Putirka (2008)	Pressure Wang et al. (2021)	Pressure Putirka (2008)
1	1	1263.18	1269.19	7.02	1.49
1	2	1251.92	1268.44	6.93	1.64
1	3	1230.83	1255.80	5.59	1.14
2	1	1173.69	1206.43	2.95	4.00
2	2	1268.88	1268.92	6.68	1.09
2	4	1245.52	1258.07	5.90	1.37
3	1	1224.18	1244.82	4.84	1.41
3	2	1259.07	1267.08	6.59	1.39
3	3	1231.02	1253.38	6.48	4.02
3	4	1267.28	1268.57	6.85	1.92

Table 47. MS6-7 temperatures and pressures

Cpx crystal	Point on crystal	Temperature Wang et al. (2021)	Temperature Putirka (2008)	Pressure Wang et al. (2021)	Pressure Putirka (2008)
1	3	1177.73	1218.19	5.65	8.08
1	4	1314.23	1243.80	7.03	7.99
1	5	1227.62	1234.47	6.07	7.09
2	1	1292.87	1247.41	6.13	5.32
2	2	1307.37	1245.65	6.10	5.78
2	3	1290.05	1235.38	5.53	6.24
2	4	1282.96	1243.33	5.60	5.06
3	1	1338.44	1267.11	6.50	3.74
3	2	1322.54	1273.04	7.03	3.10
3	3	1332.84	1270.74	6.74	2.56
3	4	1329.71	1269.87	6.80	2.86
3	5	1349.21	1270.04	6.68	3.03
3	6	1340.62	1270.00	6.64	2.76
4	1	1280.18	1248.70	5.49	5.27
4	2	1282.20	1252.38	6.06	5.78
4	3	1260.28	1244.88	5.34	5.29
4	4	1276.40	1247.69	5.81	6.01

Table 48. M1-4B temperatures and pressures

Cpx crystal	Point on crystal	Temperature Wang et al. (2021)	Temperature Putirka (2008)	Pressure Wang et al. (2021)	Pressure Putirka (2008)
1	1	1148.76	1175.21	0.35	5.80
1	2	1142.55	1169.62	-1.41	3.50
1	3	1148.47	1177.06	0.66	6.36
1	4	1147.67	1178.98	0.14	5.25
1	5	1152.55	1181.22	0.32	5.58
1	6	1168.11	1189.50	1.20	4.50
1	7	1150.85	1176.14	-0.14	4.28
2	1	1150.82	1180.91	-0.04	4.70
2	2	1170.68	1195.09	1.33	4.28
2	3	1150.83	1178.88	-0.37	4.41
2	4	1147.38	1167.67	-0.13	6.86
2	5	1147.53	1174.99	-0.33	5.41

Table 49. M2-1A temperatures and pressures

Cpx crystal	Point on crystal	Temperature Wang et al. (2021)	Temperature Putirka (2008)	Pressure Wang et al. (2021)	Pressure Putirka (2008)
1	1	1208.58	1190.51	0.86	5.23
1	2	1222.79	1205.61	1.96	5.38
1	3	1202.94	1205.83	2.03	4.00
1	4	1207.18	1198.73	2.08	5.80
1	5	1185.27	1195.84	0.88	2.60
1	6	1188.23	1193.68	0.98	3.17
2	1	1136.86	1165.77	1.11	8.17
2	2	1162.95	1192.91	0.63	3.24
2	3	1248.32	1176.56	-1.33	1.46
2	4	1147.39	1178.69	-1.13	1.66
3	2	1151.88	1185.16	0.55	4.65
3	3	1142.28	1170.07	0.14	5.80
3	6	1155.67	1186.03	-0.03	3.12
4	1	1146.93	1178.89	-0.43	4.03
4	2	1146.08	1175.38	-2.07	0.99
4	3	1158.37	1195.43	-0.36	1.08
4	4	1145.00	1175.96	-1.09	2.96
4	5	1129.89	1164.37	-2.32	2.55

Table 50. M3-3 temperatures and pressures

Cpx crystal	Point on crystal	Temperature Wang et al. (2021)	Temperature Putirka (2008)	Pressure Wang et al. (2021)	Pressure Putirka (2008)
1	1	1154.96	1228.21	0.06	1.08
1	2	1169.70	1230.73	0.57	1.38
1	3	1161.60	1227.70	0.16	1.12
1	4	1155.10	1225.48	0.06	1.08
1	5	1159.91	1225.38	-0.18	0.76
1	6	1140.48	1210.32	-2.09	-0.20
2	1	1198.31	1231.95	1.20	3.11
2	2	1192.24	1234.89	1.09	2.27
2	3	1196.04	1230.72	0.30	1.67
2	4	1200.72	1247.96	1.65	1.64
2	5	1202.83	1246.45	1.60	1.72
2	7	1202.97	1227.29	1.43	4.31
2	8	1195.48	1228.11	2.31	6.00
3	5	1133.12	1198.41	-0.99	3.24
3	6	1138.08	1207.34	-0.25	3.39
3	7	1132.94	1197.97	-2.09	1.33

Table 51. SO-18173 temperatures and pressures

Cpx crystal	Point on crystal	Temperature Wang et al. (2021)	Temperature Putirka (2008)	Pressure Wang et al. (2021)	Pressure Putirka (2008)
1	1	1167.81	1207.42	4.85	7.88
1	2	1145.77	1197.68	4.43	8.99
1	3	1162.62	1204.59	3.78	7.34
1	4	1184.87	1217.98	4.16	5.46
1	5	1166.31	1210.43	3.47	5.30
1	6	1227.04	1223.96	4.72	6.09
1	7	1189.88	1213.19	4.63	6.83
2	1	1199.97	1214.69	4.11	6.13
2	2	1212.91	1222.32	4.46	5.63
2	5	1189.28	1220.94	5.03	6.99
3	1	1271.78	1226.85	5.08	6.44
3	2	1263.90	1225.23	4.95	6.30
3	3	1288.01	1243.38	5.50	5.33
3	4	1248.78	1241.22	5.33	4.39
3	5	1252.75	1236.88	4.71	3.83
3	6	1260.26	1236.55	4.72	4.31
4	1	1213.51	1227.25	3.52	1.90
4	2	1241.15	1251.50	6.19	4.17
4	3	1279.25	1242.16	5.13	3.88
4	4	1276.07	1229.90	4.74	5.16
4	5	1247.47	1234.34	4.98	5.06
4	6	1262.59	1239.35	4.80	3.91

Table 52. SO-18176 B temperatures and pressures

Cpx crystal	Point on crystal	Temperature Wang et al. (2021)	Temperature Putirka (2008)	Pressure Wang et al. (2021)	Pressure Putirka (2008)
1	1	1182.35	1215.26	1.93	1.77
1	2	1155.78	1191.38	1.17	3.42
1	3	1175.32	1211.76	1.79	1.98
1	4	1148.87	1188.61	0.87	3.91
1	5	1161.54	1197.31	1.08	3.19
1	7	1180.75	1213.54	2.46	2.91
2	1	1218.03	1225.03	4.15	3.94
2	3	1160.53	1197.53	2.76	5.76
2	4	1168.41	1201.13	1.64	3.86
2	5	1154.95	1193.82	1.59	4.42
2	6	1158.11	1191.21	0.94	3.86
2	7	1164.98	1202.45	0.85	2.23
3	2	1166.21	1202.55	1.10	2.08
3	3	1184.87	1216.29	1.87	0.76
3	4	1164.62	1197.19	0.90	2.07
3	5	1181.96	1207.63	1.69	1.95

Table 53. SO-1747A temperatures and pressures

Cpx crystal	Point on crystal	Temperature Wang et al. (2021)	Temperature Putirka (2008)	Pressure Wang et al. (2021)	Pressure Putirka (2008)
1	1	1227.33	1244.29	5.55	4.45
1	3	1240.28	1244.46	5.75	4.60
1	4	1235.07	1232.14	4.21	3.39
1	5	1230.44	1243.19	5.59	4.79
2	1	1229.96	1230.24	4.10	3.04
2	2	1245.21	1240.55	4.46	2.25
2	3	1229.44	1230.43	3.94	2.35
2	4	1226.57	1230.32	4.10	3.07
3	1	1234.68	1236.60	4.56	3.33
3	2	1245.39	1240.73	5.50	4.57
3	3	1236.70	1243.92	5.75	4.44
3	4	1225.35	1238.79	5.14	4.34
3	5	1204.60	1236.24	5.63	5.68

Table 54. 1601.2A temperatures and pressures

Cpx crystal	Point on crystal	Temperature Wang et al. (2021)	Temperature Putirka (2008)	Pressure Wang et al. (2021)	Pressure Putirka (2008)
1	1	1263.70	1262.65	5.76	0.74
1	2	1165.52	1194.36	-1.91	-2.45
1	3	1273.03	1262.64	5.84	1.16
1	4	1252.23	1256.82	5.14	0.99
2	2	1188.15	1196.38	5.02	8.63
2	3	1258.05	1225.40	6.30	6.72
2	4	1279.03	1212.47	5.52	7.16
3	1	1179.57	1197.44	4.64	7.37
3	2	1206.54	1213.42	4.64	5.38
3	3	1259.34	1234.03	5.27	2.79
3	4	1263.24	1232.17	5.78	4.03
3	5	1211.70	1218.60	5.22	5.49

REFERENCES

Andrews, V.P., Hanson, R.E., Baylor, D., Lehman, K.M., and Williams, J.W, 2016, Intermixed hawaiian, strombolian, and phreatomagmatic eruption styles in a Mesoproterozoic volcanic arc sequence (Barby Formation) in southwest Namibia: Geological Society of America Abstracts with Programs, v. 48, no. 7, doi: 10.1130/abs/2016AM-283694.

Andrews, V.P., Hanson, R.E., Lehman, K.M., Baylor, D., and Williams, J.W., 2017, Volcanic and hypabyssal lithofacies in a Mesoproterozoic volcanic arc sequence, Barby Formation, southwest Namibia: Geological Society of America Abstracts with Programs, v. 49, no. 1, doi: 10.1130/abs/2017SC-289494.

Armienti, P., Perinelli, C., and Putirka, K.D., 2013, A new model to estimate deep-level magma ascent rates, with applications to Mt. Etna (Sicily, Italy): Journal of Petrology, v. 54, p. 795-813.

Becker, T., Hansen, T., Weber, K., and Weigand, B., 1996, U-Pb and Rb-Sr data for the Mooirivier Complex, Weener Igneous Suite, and Gaub Valley Formation (Rehoboth Sequence) in the Nauchas area and their significance for Paleoproterozoic crustal evolution in Namibia: Geological Survey of Namibia Communications, v. 11, p. 33-48.

Brady, J. and Perkins, D., 2008, Mineral formulae recalculation spreadsheet, clinopyroxene formula spreadsheet, Science Education Resource Center, Carleton College.

Brown, G.J. and Wilson, A.H., 1986, The petrology and geochemistry of the Barby Formation, Sinclair Sequence: Geological Survey of South West Africa/Namibia Communications, v. 2, p. 85-99.

Cabanis, B., and Lecolle, M., 1989, The La/10-Y/15-Nb/8 diagram: a tool for discriminating volcanic series and evidencing continental crust magmatic mixtures and/or contamination: Comptes Rendus de l'Academie des Sciences, Serie 2, Mecanique, Physique, Chimie: Sciences de l'Univers, Sciences de la Terre, v. 309, p. 2023-2029.

Cornell, D.H., van Schijndel, V., Simonsen, S.L., and Frei, D., 2015, Geochronology of Mesoproterozoic hybrid intrusions in the Konkiep terrane, Namibia, from passive to active continental margin in the Namaqua-Natal Wilson cycle: Precambrian Research, v. 265, p. 166-188.

Cornell, D.H., Harris, M., Mapani, B.S., Malobela, T., Frei, D., Kristoffersen, M., Lehman Francko, K., and Hanson, R., 2020, Dating of the Guperas Formation rhyolites changes the stratigraphy of the Mesoproterozoic Sinclair Supergroup of Namibia: South African Journal of Geology, v. 123, p. 633-648.

Corner, B., 2008, The crustal framework of Namibia derived from an integrated interpretation of geophysical and geological data, *in* Miller, R.M., ed., The Geology of Namibia: Archaean to Mesoproterozoic, vol. 1. Ministry of Mines and Energy, Geological Survey of Namibia, Windhoek, p. 1-19.

Deer, W.A., Howie, R.A., and Zussman, J., 2013, An Introduction to Rock Forming Minerals: London, Mineralogical Society of Great Britain and Ireland, 3rd edition, 498 p.

Feng, W. and Zhu, Y., 2019, Magmatic plumbing system beneath a fossil continental arc volcano in western Tianshan (NW China): constraints from clinopyroxene and thermodynamic modeling: Lithos, v. 350-351, doi: 10.1016/j.lithos.2019.105221.

Hanson, R.E., 2003, Proterozoic geochronology and tectonic evolution of southern Africa, *in* Yoshida, M., Windley, B., and Dasgupta, S., eds., Proterozoic East Gondwana: Supercontinent Assembly and Breakup: Geological Society of London Special Publication 206, p. 428-463.

Hanson, R.E., Wilson, T.J., Brueckner, H.K., Onstott, T.C., Wardlaw, M.S., Johns, C.C., and Hardcastle, K.C., 1988, Reconnaissance geochronology, tectonothermal evolution, and regional significance of the Middle Proterozoic Choma-Kalomo block, southern Zambia: Precambrian Research, v. 42, p. 39-61.

Hanson, R.E., Crowley, J.L., Bowring, S.A., Ramezani, J., Gose, W.A., Dalziel, I.W.D., Pancake, J.A., Seidel, E.K., Blenkinsop, T.G., and Mukwakwami, J., 2004, Coeval large-scale magmatism in the Kalahari and Laurentian cratons during Rodinia assembly: Science, v. 304, p. 1126-1129.

Hanson, R. E., Harmer, R. E., Blenkinsop, T.G., Bullen, D.S., Dalziel, I.W.D., Gose, W.A., Hall, R.P., Kampunzu, A.B., Key, R.M., Mukwakwami, J., Munyanyiwa, H., Pancake, J.A., Seidel, E.K., and Ward, S.E., 2006, Mesoproterozoic intraplate magmatism in the Kalahari craton: A review: Journal of African Earth Sciences, v. 46, p. 141-167.

Hanson, R.E., Andrews, V.P., Ohrmundt, S.C., Lehman, K.M., Baylor, D.J., and Williams, J.W., 2018, Eruptive mechanisms, lithofacies patterns and subvolcanic magma plumbing systems in a 1.2 Ga extensional continental margin arc on the edge of the Kalahari Craton, SW Namibia: Geological Society of America Abstracts with Programs, v. 50, no. 1, doi: 10.1130abs/2018sc-310181.

Harris, M., Cornell, D.H., Mapani, B.S., Malobela, T., Lundell, C., and Jonsson, A.K., 2020, The Kumbis and Nagatis Formations and the Helmeringhausen Gabbro: Oldest undeformed rocks of the Sinclair Supergroup in Namibia: Journal of African Sciences, v. 165, Article 13733.

Harris, M., Mapani, B. S., Cornell, D. H., Malobela, T., Weber, B., Kristoffersen, M., Lehman Francko, K., and Hanson, R., 2021, Chronostratigraphic correlation of the volcanic 1.21 Ga Barby and Haiber Flats Formations in the Sinclair Supergroup of Namibia: Journal of African Earth Sciences, v. 178, Article 104180.

Hoal, B., 1989, The geologic history of the Awasib Mountain terrane and its relationship to the Sinclair Sequence and the Namaqualand Metamorphic Complex: Geological Survey of Namibia Communications, v.5, p. 41-51.

Hoal, B.G., 1990, The geology and geochemistry of the Proterozoic Awasib Mountain Terrain, southern Namibia: Geological Survey of Namibia, Memoir 11, 163 p.

Hoal, B.G., 1993, The Proterozoic Sinclair Sequence in southern Namibia: intracratonic rift or active continental margin setting? Precambrian Research, v. 63, p. 143-162.

Houghton, B.F., and Smith, R.T., 1993, Recycling of magmatic clasts during explosive eruptions: estimating the true juvenile content of phreatomagmatic volcanic deposits: Bulletin of Volcanology, v. 55, p. 414-420.

Kasbohm, J., Evans, D., Panzik, J.E., Hofmann, M., and Linnemann, U., 2016, Paleomagnetic and geochronological data from Late Mesoproterozoic redbed sedimentary rocks on the western margin of Kalahari craton, *in* Li, Z.X., Evans, D.A.D., and Murphy, J.B., eds., Supercontinent Cycles through Earth History: Geological Society London, Special Publication, v. 424. p. 145-159.

Lehman, K.M., 2019, Exploring the geochemical evolution of magmatic sources in relation to tectonic setting in the Mesoproterozoic Konkiep terrane, Namaqua-Natal orogen, SW Namibia [M.S. Thesis]: Texas Christian University, 243 p.

Lehman, K.M., Andrews, V.P., Hanson, R.E., Baylor, D.J., and Williams, J.W., 2016, A paleogeographic control on the formation of thick, downward-growing, sill packages emplaced into wet sediments within a Mesoproterozoic volcanic arc in south-central Namibia: Geological Society of America Abstracts and Programs, v. 48, no. 7, doi: 10.1130/abs/2016AM-281508.

Leterrier, J., Maury, R.C., Thonon, P., Girard, D., and Marchal, M., 1982, Clinopyroxene composition as a method of identification of the magmatic affinities of paleo-volcanic series, Earth and Planetary Science Letters, v. 59, p. 139-154.

Malobela, T., Mapani, B., Harris, M., Cornell, D.H., Karlsson, A., Jonsson, A.K., Lundell, C., and Kristoffersen, M., 2019, Age and geological context of the Barby Formation, a key volcanic unit in the Mesoproterozoic Sinclair Supergroup of southern Namibia: South African Journal of Geology, v. 122, p. 519-540.

Magee, C., Muirhead, J. D., Karvelas, A., Holford, S. P., Jackson, C. A. L., Bastow, I. D., Schofield, N., Stevenson, C. T.E., McLean, C., McCarthy, W., and Shtukert, O., 2016, Lateral magma flow in mafic sill complexes: Geosphere, v. 12, no. 3, p. 817-833, doi: 10.1130/GES01256.1.

Miller, R. McG., 1969, The Auborus Formation of the Bethanie District, South West Africa: Bulletin of the Precambrian Research Unit, University of Cape Town, v. 2, 32 p.

Miller, R. McG., 2008, The Geology of Namibia, Vol. 1, Archaean to Mesoproterozoic: Windhoek, Geological Survey of Namibia, p. 8-1 to 8-104.

Miller, R. McG., 2012, Review of Mesoproterozoic magmatism, sedimentation and terrane amalgamation in southwestern Africa: South African Journal of Geology, v. 115, p. 417-448.

Morimoto, N., 1988, Nomenclature of pyroxenes: American Mineralogist, v. 73, p. 1123-1133.

Ohrmundt, S.C., 2020, Eruptive styles, magma-plumbing systems, and magma/sediment interaction in a 1.2 Ga calc-alkaline to shoshonitic volcanic arc setting, SW Namibia [M.S. Thesis]: Texas Christian University, 75 p.

Ohrmundt, S.C., Hanson, R.E., and Caves, L.R., 2019, Complex shallow-level andesitic magma plumbing systems and magma/sediment interaction in a Mesoproterozoic volcanic arc setting in Namibia: Geological Society of America, Abstracts with Programs, v. 51, no. 2, doi: 10.1130/abs/2019SC-327355.

Panzik, J.E., Evans, D.A.D., Kasbohm, J.J., Hanson, R., Gose, W., and DesOrmeau, J., 2016, Using palaeomagnetism to determine late Mesoproterozoic palaeogeographic history and tectonic relations of the Sinclair Terrane, Namaqua Orogen, Namibia, *in* Li, Z.X., Evans, D.A.D., and Murphy, J.B., eds., Supercontinent Cycles through Earth History: Geological Society of London Special Publication 424, p. 119-143.

Pearce, J.A., and Cann, J.R., 1973, Tectonic setting of basic volcanic rocks determined using trace element analysis: Earth and Planetary Science Letters, v. 19, p. 290-300.

Pearce, J.A., 1982, Trace element characteristics of lavas from destructive plate margins, *in* Thorpe, R.S., ed., Andesites: Orogenic Andesites and Related Rocks, Wiley, p. 525-548.

Pearce, J.A., 1996, A users guide to basalt discrimination diagrams, *in* Bailes, A.H. Christiansen, E.H., Galley, A.G., Jenner, G.A., Keith, Jeffrey D., Kerrich, R., Lentz, David R., Lesher, C.M., Lucas, Stephen B., Ludden, J.N., Pearce, J.A., Peloquin, S.A., Stern, R.A., Stone, W. E., Syme, E.C., Swinden, and H.S., Wyman, D.A., eds., Trace element geochemistry of

volcanic rocks; applications for massive sulphide exploration, Geological Association of Canada, Short Course Notes, v. 12, p. 79-113.

Putirka, K.D., 2008, Thermometers and barometers for volcanic systems: Reviews in Mineralogy and Geochemistry, vol. 69, p. 66-120.

Rossel, P., Oliveros, V., Ducea, M.N., and Hernandez, L., 2015, Across and along arc geochemical variations in altered volcanic rocks: Evidence from mineral chemistry of Jurassic lavas in northern Chile, and tectonic implications: Lithos, v. 239, p. 97-113.

Sheehan, F. and Barclay, J., 2016, Staged storage and magma convection at Ambryn volcano, Vanuatu: Journal of Volcanology and Geothermal Research 322, p. 144-157.

Singletary, S.J., Hanson, R.E., Martin, M.W., Crowley, J.L., Bowring, S.A., Key, R.M., Ramokate, L.V., Direng, B.B., and Krol, M.A., 2003, Geochronology of basement rocks in the Kalahari Desert, Botswana, and implications for regional Proterozoic tectonics: Precambrian Research, v. 121, p. 47-71.

Von Brunn, V., 1969, Igneous rocks of the Nagatis and Sinclair Formations north-east of Lüdertiz, South West Africa: Bulletin of the Precambrian Research Unit, University of Cape Town, v. 7, 54 p.

Wang, X., Hou, T., Wang, M., Zhang, C., Zhang, Z., Pan, R., Marxer, F., and Zhang, H., 2021, A new clinopyroxene thermobarometer for mafic to intermediate magmatic systems: European Journal of Mineralogy, v. 33, p. 621-637.

Watters, B.R., 1974, Stratigraphy, igneous petrology and evolution of the Sinclair Group in southern South West Africa: Bulletin of the Precambrian Research Unit, University of Cape Town, v. 16, 235 p.

VITA

Personal Background

Lauren Taylor Burden
Born in Fort Worth, Texas
Daughter of Scott and Joi Burden

Education

Diploma, Tahquitz High School, Hemet, CA, May 2016
Texas Christian University, Fort Worth, TX
Master of Science in Geology, May 2022
Bachelor of Science in Geology, May 2020

Experience

Graduate Assistant, August 2020- May 2022
Texas Christian University, Fort Worth, TX

ABSTRACT

USING CLINOPYROXENE CHEMISTRY TO CONSTRAIN MAGMA PLUMBING SYSTEMS IN A 1.2 GA ANDESITIC TO SHOSHONITIC VOLCANIC ARC, BARBY FORMATION, NAMIBIA

By Lauren Taylor Burden, M.S., 2022
Department of Geological Sciences
Texas Christian University

Thesis Advisor: Richard Hanson, Professor of Geology

The 1.2 Ga Barby Formation located in SW Namibia is composed of basaltic andesites and shoshonites erupted in a volcanic arc setting. Clinopyroxene (cpx) from samples of pyroclastic rocks and hypabyssal intrusions previously collected by TCU graduate students was analyzed using an electron microprobe at Fayetteville State University, North Carolina. Correlations between cpx and whole-rock chemistry are used to provide additional insights into the complex magma plumbing system feeding the Barby Formation. Cpx compositions and cation ratios were also used in an attempt to constrain pressure and temperature conditions in the source magma chambers using geothermobarometry. Cpx data from hypabyssal intrusions in one part of the study area provide evidence of a different magma reservoir compared to the other samples.